

November 2015

## Virtual Antennas Using Metamaterials

CAGLAR D. EMIROGLU  
*University of Massachusetts - Amherst*

Follow this and additional works at: [https://scholarworks.umass.edu/dissertations\\_2](https://scholarworks.umass.edu/dissertations_2)



Part of the [Electromagnetics and Photonics Commons](#)

---

### Recommended Citation

EMIROGLU, CAGLAR D., "Virtual Antennas Using Metamaterials" (2015). *Doctoral Dissertations*. 490.  
[https://scholarworks.umass.edu/dissertations\\_2/490](https://scholarworks.umass.edu/dissertations_2/490)

This Open Access Dissertation is brought to you for free and open access by the Dissertations and Theses at ScholarWorks@UMass Amherst. It has been accepted for inclusion in Doctoral Dissertations by an authorized administrator of ScholarWorks@UMass Amherst. For more information, please contact [scholarworks@library.umass.edu](mailto:scholarworks@library.umass.edu).

# **VIRTUAL ANTENNAS USING METAMATERIALS**

A Dissertation Presented

by

**CAGLAR D. EMIROGLU**

Submitted to the Graduate School of the  
University of Massachusetts Amherst in partial fulfillment  
of the requirements for the degree of

**DOCTOR OF PHILOSOPHY**

September 2015

Electrical and Computer Engineering

© Copyright by Caglar D. Emiroglu 2015

All Rights Reserved

# **VIRTUAL ANTENNAS USING METAMATERIALS**

A Dissertation Presented

by

**CAGLAR D. EMIROGLU**

Approved as to style and content by:

---

Do-Hoon Kwon, Chair

---

Ramakrishna Janaswamy, Member

---

Marinos N. Vouvakis, Member

---

Mark Tuominen, Member

---

C. V. Hollot, Department Head  
Electrical and Computer Engineering



*To Sadiye, Mustafa, and İmge Miray.*

## ACKNOWLEDGMENTS

I here would like to express my sincere gratitude to those people who had a touch in this work.

I would like to thank my adviser Professor Do-Hoon Kwon for his invaluable support and guidance. I have always admired his dedication to his work, and I am so much grateful that I had the opportunity to work together with him. I would also like to thank Professors Ramakrishna Janaswamy, Marinos N. Vouvakis, and Mark Tuominen for devoting their time to serve in my committee. It was a great opportunity to learn from them throughout my studies. I would like to thank to all of my colleagues in the Antenna Laboratory, particularly to Hsieh-Chi Chang, Yutong Yang, and Amin Nikravan, for their help and effort in the measurements. I would also like to thank to my former labmates and fellows for their strong company in this journey.

The one and only unique source of support is my family, to whom I dedicate my dissertation. It is their natural and perpetual love that made this work possible.

Çağlar Doğu Emiroğlu

Amherst, MA

# **ABSTRACT**

## **VIRTUAL ANTENNAS USING METAMATERIALS**

SEPTEMBER 2015

CAGLAR D. EMIROGLU

B.Sc., MIDDLE EAST TECHNICAL UNIVERSITY

M.Sc., UNIVERSITY OF MASSACHUSETTS AMHERST

Ph.D., UNIVERSITY OF MASSACHUSETTS AMHERST

Directed by: Professor Do-Hoon Kwon

Virtual antenna radiation at microwave frequencies using metamaterials is presented. Based on the transformation electromagnetics technique, the media embedding a physical antenna in a ground recess is designed such that the far-zone radiation pattern of a virtual antenna radiating above a flat conducting ground plane is reproduced. The antenna and a limited surrounding space above a ground plane is folded below the ground level, resulting in a physical antenna in a ground recess that is enclosed in transformation media. The electromagnetic specification of the media surrounding the physical antenna at the bottom of the recess is provided by a properly defined coordinate transformation.

A three-step design approach is followed. First, microstrip transmission-line metamaterials for a ground-recessed probe are designed and implemented for virtual source formation above the ground plane. Transmission-line metamaterial unit cell designs for the embedding media are shown. Virtual probe formation is validated using full-wave

simulations. Measured field distributions over the fabricated metamaterial-surface for an embedded probe current radiating in a ground recess confirm formation of a virtual line source above the ground plane. As a next step, resonant inclusion-based metamaterials are designed for embedding a two-dimensional electric line source in a ground recess. Metamaterials are fabricated and assembled. Measured field distributions for an effective two-dimensional configuration confirm formation of a virtual line current above the ground plane. As a final extension to a three-dimensional configuration, design, fabrication, and measurement of an embedded monopole antenna in a ground recess is presented. Poorer performance was measured compared with the two-dimensional case. The complexity and material losses associated with resonator-based, negative-index metamaterials for multiple polarizations in three-dimensional applications were identified as main technical challenges.

# TABLE OF CONTENTS

	<b>Page</b>
<b>ACKNOWLEDGMENTS</b> .....	<b>v</b>
<b>ABSTRACT</b> .....	<b>vi</b>
<b>LIST OF TABLES</b> .....	<b>x</b>
<b>LIST OF FIGURES</b> .....	<b>xi</b>
 <b>CHAPTER</b>	
<b>1. INTRODUCTION</b> .....	<b>1</b>
1.1 Background .....	1
1.2 Motivation .....	5
1.3 Contributions .....	7
<b>2. DESIGN BASED ON COORDINATE TRANSFORMATION</b> .....	<b>9</b>
2.1 3-D Virtual Antenna Radiation .....	9
2.1.1 Coordinate Transformation .....	9
2.1.2 Numerical Results .....	11
2.2 2-D Virtual Line Source Radiation .....	14
2.2.1 Coordinate Transformation .....	14
2.2.2 Numerical Results .....	16
<b>3. ANISOTROPIC METAMATERIALS AND HOMOGENIZATION</b> .....	<b>19</b>
3.1 A Conventional Homogenization Method .....	20
3.2 Non-Orthogonal Grids in 2-D Metamaterials .....	22
3.2.1 Coordinate Transformation .....	25
3.2.2 Design Procedure .....	27

3.3	<i>S</i> -Parameter-Based Homogenization of an Anisotropic Medium .....	28
<b>4.</b>	<b>MICROSTRIP TL-METAMATERIAL DESIGN .....</b>	<b>32</b>
4.1	Microstrip TL Metamaterial Cell Designs .....	32
4.2	Numerical Results .....	37
4.3	Measurement Results .....	40
<b>5.</b>	<b>2-D METAMATERIAL EMBEDDED LINE SOURCE .....</b>	<b>48</b>
5.1	Unit Cells for the Negative-Index Lens $A_3$ .....	48
5.2	Unit Cell for the Matcher $A_2$ .....	55
5.3	Measurement Results .....	61
<b>6.</b>	<b>3-D METAMATERIAL-EMBEDDED MONOPOLE .....</b>	<b>78</b>
6.1	Unit Cells for the Negative-Index Lens $A_3$ .....	78
6.1.1	Outer volume .....	79
6.1.2	Central volume .....	80
6.2	Unit Cells for the Matcher $A_2$ .....	84
6.2.1	Rotated cubic unit cell .....	84
6.2.2	Parallelogram cross-section unit cell .....	85
6.3	Fabrication, Assembly and Measurement Results .....	95
6.3.1	Fabrication and Assembly of the Metamaterials .....	95
6.3.2	Measurement Results .....	98
<b>7.</b>	<b>SUMMARY AND CONCLUSIONS .....</b>	<b>116</b>
	<b>BIBLIOGRAPHY .....</b>	<b>118</b>

## LIST OF TABLES

Table	Page
4.1 Host TL configurations, and the loading elements used in the fabrication for each region. ....	45
4.2 Manufacturer part numbers of the components used in the fabrication. ....	45
5.1 Geometrical design parameters for the NIM unit cells (in mm). ....	52
5.2 Geometrical design parameters for the unit cell (in mm). ....	59
6.1 Geometrical design parameters for the outer NIM unit cell (in mm). ....	80
6.2 Geometrical design parameters for the central NIM unit cell (in mm). ....	82
6.3 Geometrical design parameters for the rotated cubic matcher unit cell (in mm). ....	89
6.4 Geometrical design parameters for the parallelogram cross section matcher unit cell (in mm). ....	91

## LIST OF FIGURES

Figure		Page
1.1	The coordinate transformation based invisibility cloak design guides the incident waves around a spherical volume [33]. (b) The 2-D metamaterial cloak experimentally verified at microwave frequencies [39]. . . . .	2
1.2	(a) A non-uniform circular array designed to radiate and receive as a uniformly spaced linear array [34]. (b) A 4-element array with an effective physical aperture reduced by a factor of 2 [54]. . . . .	3
1.3	Objective: an antenna and embedding media without protrusion above the ground plane, radiating vertically polarized fields with maximum radiation in the horizon on the ground plane. (a) Electrical configuration. (b) Physical configuration. . . . .	5
2.1	The coordinate transformation between the original (virtual) and embedded (physical) radiation configurations. (a) Original configuration. (b) Embedded configuration. . . . .	10
2.2	Snapshots of the $H_\phi$ distributions. (a) Original configuration. (b) Embedded configuration. . . . .	12
2.3	Simulated directivity patterns for the embedded configuration, compared with the cases without $A_2$ and without $A_3$ . . . . .	12
2.4	Simulated far-field gain patterns for the embedded configuration, compared with the case of a lossy $A_2$ region having effective medium parameters $\epsilon = \mu = 1 - j100$ . . . . .	13
2.5	The 2-D coordinate transformation between the original (virtual) and embedded (physical) radiation configurations. (a) Original configuration. (b) Embedded configuration. . . . .	15
2.6	Snapshots of the $E_z$ distributions. (a) Original configuration. (b) Embedded configuration. . . . .	17



2.7	Simulated 2-D directivity patterns for the embedded configuration, compared with the cases without $A_2^\pm$ and without $A_3$ .....	18
2.8	Refraction through a flat NIM slab with $\epsilon = \mu = -1$ in free space. ....	18
3.1	Homogenization based on the reflection and transmission coefficients. (a) An inhomogeneous metamaterial slab of thickness $d$ . (b) Equivalent homogeneous slab with the retrieved refractive index $n$ and impedance $z$ . ....	20
3.2	A perspective view of the non-orthogonal grid TL metamaterial unit cell. ....	23
3.3	Top view of the non-orthogonal grid (or parallelogram) TL metamaterial unit cell. ....	25
3.4	Homogenization of an anisotropic medium under normally incident plane wave illuminations. (a) An anisotropic medium in free space. (b) $\alpha_1 = 0$ . (c) $\alpha_2$ . (d) $\alpha_3$ . ....	29
3.5	Elliptical dispersion curves for an anisotropic medium in 2-D. ....	30
4.1	An embedded line source (red dot) inside a ground recess. ....	32
4.2	A generic 2-D TL metamaterial unit cell. (a) 2-D periodic unit cell. (b) Definitions for $Z_1$ , $Z_2$ and $Y$ .....	33
4.3	Top view of the 2-D TL metamaterial unit cell in a non-orthogonal grid.....	35
4.4	Snapshot of $E_z$ for the embedded probe configuration.....	38
4.5	Snapshot of $E_z$ for the original configuration of a probe over a flat ground plane. ....	39
4.6	TL NIM unit cell for parameter retrieval and optimization. ....	40
4.7	Homogenized medium parameters of the optimized NIM cell with the real load values. (a) Refractive index $n_{\text{NIM}}$ . (b) Normalized impedance $z_{\text{NIM}}$ . ....	41
4.8	TL matcher unit cell for parameter retrieval and optimization. ....	41

4.9	Homogenized medium parameters of the optimized matcher cell along $q_1$ with the real load values. (a) Refractive index $n$ . (b) Normalized impedance $z$ . . . . .	42
4.10	Homogenized medium parameters of the optimized matcher cell along $q_2$ with the real load values. (a) Refractive index $n$ . (b) Normalized impedance $z$ . . . . .	42
4.11	A detailed view of the TL metamaterial grid over the area of the embedding region. (a) Fabricated sample. (b) Design schematic. . . . .	43
4.12	Measurement setup. Top view of a NIM unit cell in detail. . . . .	43
4.13	Measurement setup. $x - y$ positioner table. . . . .	44
4.14	Measured $S_{21}$ distributions at $f = 1.616$ GHz. (a) Phase. (b) Magnitude. 46	
4.15	Measured $S_{21}$ phase distributions. (a) At $f = 1.592$ GHz. (b) At $f = 1.640$ GHz. . . . .	47
5.1	Unit cell for the NIM superlens metamaterial. (a) 3-D view. (b) SRR wall. (b) ELC wall. The side of the unit cell is equal to $d\sqrt{2}$ . . . . .	49
5.2	The retrieved medium parameters of the optimized NIM unit cell for $A_3$ . Index of refraction $n = n' - jn''$ , and impedance $z = z' - jz''$ . . . . .	50
5.3	The retrieved medium parameters of the optimized NIM unit cell for $A_3$ . The relative permeability $\mu = \mu' - j\mu''$ , and permittivity $\epsilon = \epsilon' - j\epsilon''$ . . . . .	51
5.4	Retrieved transmittance, reflectance, and absorbance of the optimized NIM unit cell for $A_3$ . . . . .	52
5.5	The NIM lens under line source illumination. . . . .	53
5.6	Unit cells for the NIM lens under TE-polarized plane wave illuminations. (a) Rotated NIM cell. (b) Conventional NIM cell. . . . .	54
5.7	The effective medium parameters of the NIM lenses as a function of the incidence angle $\theta_i$ . (a) Index of refraction $n = n' - jn''$ . (b) Impedance $z = z' - jz''$ . . . . .	55
5.8	Unit cell for the anisotropic impedance-matching block $A_2$ . (a) 3-D view. (b) The SRR face. (c) The ELC face. . . . .	56

5.9	Retrieved $\mu_{11}$ and $\epsilon_{zz}$ of the optimized metamaterial unit cell for $A_2$ .	57
5.10	Transmittance, reflectance, and absorbance of the optimized metamaterial unit cell for $A_2$ along $v_2$ .	58
5.11	Retrieved $\mu_{22}$ and $\epsilon_{zz}$ of the optimized metamaterial unit cell for $A_2$ .	60
5.12	Transmittance, reflectance, and absorbance of the optimized metamaterial unit cell for $A_2$ along $v_1$ .	61
5.13	Assembly steps for the NIM lens and the matcher metamaterial.	62
5.14	Assembled metamaterial inside the ground recess. (a) A bent aluminum strip was used as the ground recess. (b) The ground recess was treated with copper tape. The measurement volume was terminated in absorbers.	63
5.15	Metamaterial set up for field-scanning measurement. (a) Original configuration. (b) Embedded configuration.	64
5.16	Parallel-plate waveguide simulator setup on the $x - y$ positioner table. Insets show close-up photos of the cut coaxial cable used as an $E$ -field sensor in the top plate, and the $0.4\lambda_0$ -long excitation probe.	65
5.17	Measured electric field phase distributions around the design frequency $f_0 = 5$ GHz. (a) At $f = 4.92$ GHz. (b) At $f = 4.85$ GHz. (c) At $f = 5$ GHz. (d) At $f = 5.03$ GHz. (e) At $f = 5.06$ GHz.	69
5.18	Measured electric field magnitude distributions at $f = 4.92$ GHz. (a) Desired configuration. (b) Embedded configuration.	70
5.19	Measured electric field snapshots at $f = 4.92$ GHz. (a) Desired configuration. (b) Embedded configuration.	71
5.20	Measured electric field for an empty recess at $f = 4.92$ GHz. (a) Phase distribution. (b) Magnitude distribution.	72
5.21	Measured $S_{21}$ along $x = 0$ at $f = 4.92$ GHz.	73
5.22	Measured near-field patterns for the embedded configuration.	73
5.23	Measured near-field patterns at $f = 4.92$ GHz.	74
5.24	Simulated near-field patterns at $f = 4.92$ GHz.	74

5.25	Effects of the matcher region $A_2$ on the near-field pattern at $f = 4.92$ GHz. ....	75
5.26	Approximate far-field gain patterns measured at $f = 4.92$ GHz. ....	75
5.27	Simulated approximate far-field gain patterns at $f = 4.92$ GHz. ....	76
5.28	Effects of the matcher region $A_2$ on the approximate far-field gain pattern at $f = 4.92$ GHz. ....	76
5.29	Numerically calculated far-field gain patterns for measurements at $f = 4.92$ GHz. ....	77
5.30	Simulated far-field gain patterns at $f = 4.92$ GHz. ....	77
6.1	Unit cell of the outer NIM. (a) 3-D view. (b) The SRR face. (c) The ELC face. The side of the unit cell is equal to $d\sqrt{2}$ . ....	79
6.2	The retrieved medium parameters of the optimized outer NIM unit cell. (a) Index of refraction $n = n' - jn''$ . (b) Impedance $z = z' - jz''$ . ....	81
6.3	Unit cell of the central NIM. (a) 3-D view. (b) The SRR face. (c) The ELC face. The side of the unit cell is equal to $d\sqrt{2}$ . ....	82
6.4	The retrieved medium parameters of the optimized central NIM unit cell. (a) Index of refraction $n = n' - jn''$ . (b) Impedance $z = z' - jz''$ . ....	83
6.5	The cubic unit cell for $A_2$ . (a) A 3-D view. (b) The ELC faces. ....	85
6.6	The retrieved medium parameters of the optimized cubic unit cell for $A_2$ . (a) $\epsilon_{11}$ . (b) $\mu_{\phi\phi}$ . ....	86
6.7	The retrieved medium parameters of the optimized cubic unit cell for $A_2$ . (a) $\epsilon_{22}$ . (b) $\mu_{\phi\phi}$ . ....	87
6.8	Metamaterial for $A_2$ . (a) Rotated cubic unit cell. (b) Volumetric fill for a matcher constructed with the rotated cubic unit cell. ....	88
6.9	The parallelogram cross-section unit cell for $A_2$ . (a) A 3-D view. (b) The ELC faces. ....	88
6.10	Metamaterial for $A_2$ . (a) Parallelogram cross-section unit cell. (b) Volumetric fill for a matcher constructed with the parallelogram cross-section unit cell. ....	91

6.11	The retrieved medium parameters of the optimized parallelogram cross-section matcher unit cell for $A_2$ . (a)-(b), (c)-(d), (e)-(f) show the effective relative $\epsilon - \mu$ in $\theta = 0, 90, -45^\circ$ plane wave incidence directions, respectively. ....	92
6.12	The retrieved medium parameters of the optimized parallelogram cross-section matcher unit cell for $A_2$ . (a) $\epsilon_{\rho\rho}$ . (b) $\epsilon_{\rho z}$ . ....	93
6.13	The retrieved medium parameters of the optimized parallelogram cross-section matcher unit cell for $A_2$ . (a) $\epsilon_{zz}$ . (b) $\mu_{\phi\phi}$ . ....	94
6.14	Assembly of the metamaterial for the central NIM volume. (a) Creating slots in the cell walls. (b) A close-up view of the slots. (c) Cut-out cell wall strips. (d) Assembling the walls. (e) One layer of the central NIM. ....	96
6.15	Assembled metamaterial for the central NIM volume. (a) Assembled parts of the central NIM. (b) Side view. (c) Assembled central NIM metamaterial. (d) Assembled central NIM the recess. ....	97
6.16	Fabricated ground recess. $\lambda_0 = 6$ cm at the design frequency. ....	97
6.17	Top view of the unit cell assembly schematics for NIM lenses. (a) Outer NIM. (b) Central NIM fill using the outer NIM unit cell. ....	98
6.18	Assembled metamaterials for each volume. (a) Close-up view of the NIM for the outer volume. (b) Top view of the outer NIM. (c) Close-up view of the matcher metamaterial with the parallelogram cross-section unit cells. (d) Assembled matcher and the central NIM. ....	99
6.19	Metamaterial-embedded monopole antenna inside the ground recess. (a) Recess filled with the assembled metamaterials. (b) Final assembly is paper-covered for measurements. ....	99
6.20	Near-field range for spherical surface scan. ....	100
6.21	Gain patterns for the original configuration. ....	101
6.22	Gain patterns for a monopole radiating in an empty recess. ....	101
6.23	Measured gain patterns for the material-embedded monopole around $f_0 = 5$ GHz. ....	102
6.24	Ground pit for the central NIM lens experiment. ....	103

6.25	Gain patterns for a monopole radiating inside the central-NIM-filled pit. ....	103
6.26	Gain patterns for a monopole radiating in an empty pit. ....	104
6.27	NIM lens assembled using the outer NIM unit cells for the ground pit measurement. ....	105
6.28	Measured gain pattern for the pit filled with outer NIM unit cells. ....	105
6.29	Measured gain pattern for the pit filled with outer NIM unit cells in a mirror symmetric arrangement. ....	106
6.30	Gain patterns for the pit filled with outer NIM unit cells in a mirror symmetric arrangement. ....	106
6.31	Top view of the unit cell assembly schematics for the NIM lens. (a) NIM volume fill using outer NIM unit cells. (b) NIM volume fill using the unrotated outer NIM unit cells. ....	108
6.32	NIM lens using the outer NIM unit cells positioned inside the ground recess. ....	108
6.33	Measured gain pattern for the NIM-filled recess using the outer NIM unit cells. ....	109
6.34	Measured gain pattern for the NIM-filled recess using the outer volume NIM unit cells in a mirror symmetric arrangement. ....	109
6.35	Gain patterns for the NIM-filled recess using the outer volume NIM unit cells. ....	110
6.36	(a) Reflection inside the recess. (b) A top view of the outer NIM unit cell. ....	111
6.37	Simulated gain pattern with the NIM lens replaced with an isotropic medium having the effective medium parameters given by (6.11). ....	112
6.38	NIM lens positioned inside the ground recess using the outer NIM unit cells unrotated. ....	113
6.39	Measured gain for the NIM-filled recess using the outer NIM unit cells unrotated. ....	114

6.40	Gain patterns for the NIM-filled recess using the outer NIM unit cells unrotated. ....	114
------	---	-----

# CHAPTER 1

## INTRODUCTION

This dissertation work presents a metamaterial-embedded antenna radiating inside a ground recess. The media embedding a recessed antenna is designed such that the embedded antenna yields the same far-field radiation characteristics as an antenna over a flat conducting ground plane. In this chapter, the background for the subject and the motivation for studying the problem are presented.

### 1.1 Background

Metamaterials are artificial structures that can be designed to have unconventional electromagnetic properties which may not be commonly found in nature. They are designed to interact with and control electromagnetic waves. Unusual properties of metamaterials have allowed novel applications, concepts and devices [8].

Transformation electromagnetics/optics (TE/TO) is a novel design technique [22,33,53] that allows designing electromagnetic and optical devices featuring novel wave-material interaction properties based on coordinate transformations. The theory is based on the form-invariant nature of Maxwell's equations under spatial coordinate transformations [52].

Starting with the invisibility cloaks [33, 39] as shown in Figure 1.1, the TE/TO has been credited with a variety of novel device designs that manipulate propagation, reflection, and refraction properties. Embedded transformations were introduced in [36], generalizing the technique to coordinate transformations possessing discontinuities along device boundaries. For two-dimensional (2-D) geometries, quasi-conformal transformation optics (QCTO) have been utilized to design broadband carpet cloaks [25] and Luneburg



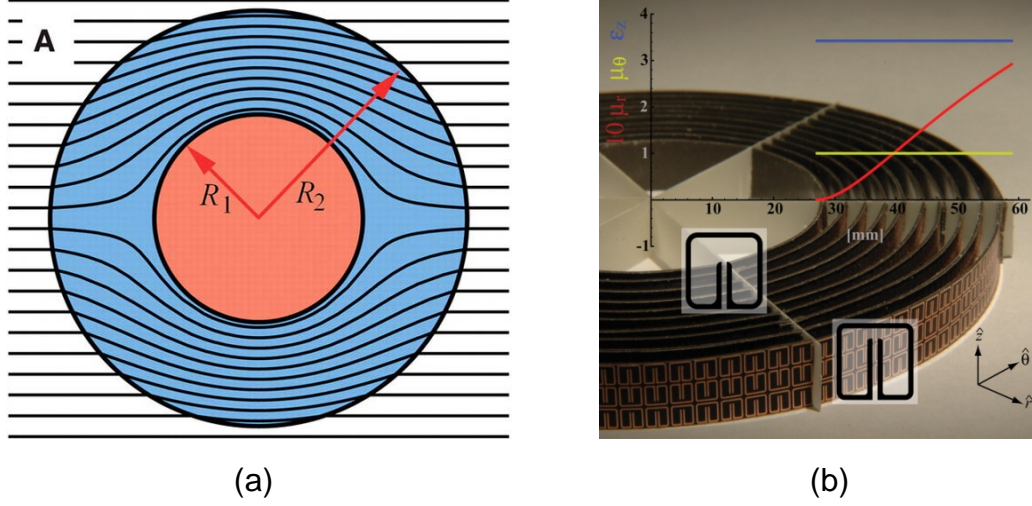


**Figure 1.1.** The coordinate transformation based invisibility cloak design guides the incident waves around a spherical volume [33]. (b) The 2-D metamaterial cloak experimentally verified at microwave frequencies [39].

lenses [14], allowing devices that can be realized accurately using isotropic electric materials with a graded index of refraction. A negative-index material (NIM) superlens or the “perfect lens” [29, 43] was interpreted in [23] as a device that utilizes a coordinate transformation involving a negative slope between coordinates. Such transformations, which lead to negative-index constituent materials in resulting devices, have led to new interesting designs such as external cloaks utilizing complementary media [20], illusion optics devices [21], and invisible electromagnetic gateways [24].

An overview of the coordinate transformation based device designs are available in [3, 15, 53]. The vast majority of TE and QCTO applications has been to wave scattering configurations, i.e., to cases where radiation sources are away from the TE device volumes or surfaces. Notable exceptions are applications to array antennas for changing the array geometry while maintaining the same radiation characteristics [17, 34, 54]. Specifically, an anisotropic embedding medium was designed to make a non-uniform circular array to radiate as a uniform linear array [34] as shown in Figure 1.2(a). A change in the source distribution results with a transformation on a volume containing sources. The behavior of

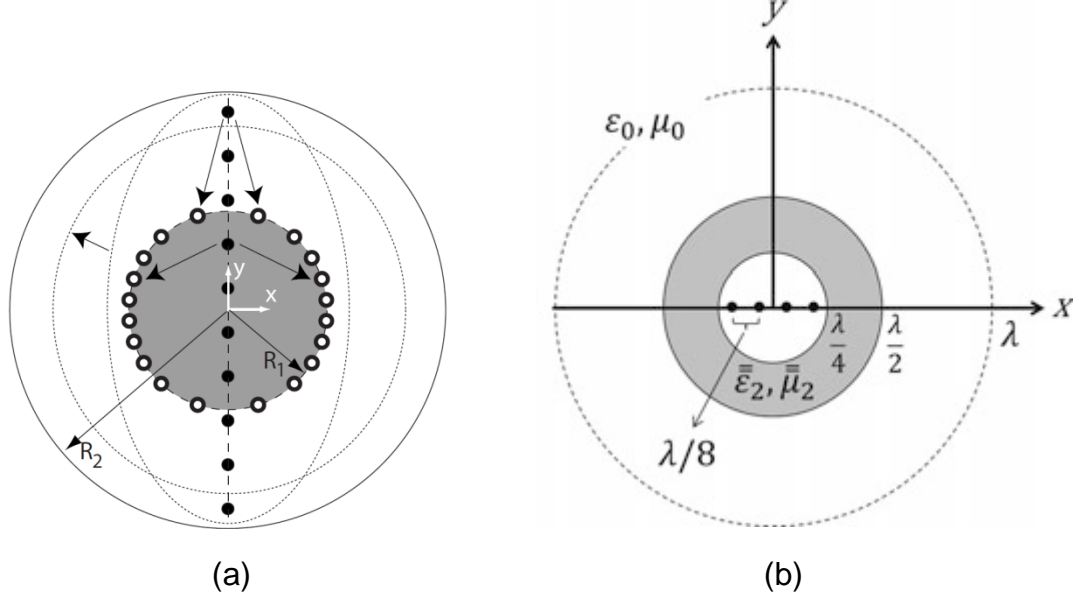


**Figure 1.2.** (a) A non-uniform circular array designed to radiate and receive as a uniformly spaced linear array [34]. (b) A 4-element array with an effective physical aperture reduced by a factor of 2 [54].

line sources and surface currents under coordinate transformations was investigated in [6]. In [17], two coordinate transformations were applied in sequence to a vertical phased array such that a resulting horizontal array has a scanning capability in the endfire angular regime. In [54], a radially inhomogeneous and anisotropic spherical shell was designed so that an enclosed array as illustrated in Figure 1.2(b) behaves like a physically larger array, both in free space and over a perfect electric conductor (PEC) ground plane. In [16], a coordinate transformation design of a material-embedded monopole antenna inside a ground recess was presented such that the embedded antenna creates the same far-zone radiation pattern as the same monopole placed over a flat conducting ground plane. The embedded configuration is flush with the surrounding ground plane and there is no physical structure above the ground plane. This configuration is capable of radiating vertically polarized fields with a pattern maximum in the horizon on the ground plane.

2-D transmission-line (TL) metamaterial design approach has been useful in realizing coordinate transformation based designs. The theory is a widely used analysis and design

tool for conventional right/left-handed metamaterials which can be realized using loaded coaxial or microstrip lines [2, 7]. The sub-diffraction limit imaging capability of a NIM superlens was experimentally verified using TL metamaterials in [11]. In [26], TL approach was used to design and simulate a cylindrical invisibility cloak. A loaded circuit network constructed with lumped elements was utilized in the simulation. The electromagnetic gateway device was constructed using a circuit network and experimentally verified [24]. In [9], TL metamaterial unit cells capable of synthesizing arbitrary full-tensor material parameters were proposed. A TL unit cell topology that can represent full-tensor material parameters was presented and demonstrated. It was shown that a rectangular TL unit cell with one or more loads along the cell diagonal can realize full-tensor anisotropic parameters. A 2-D cloak was numerically constructed and tested utilizing the unit cell. A different TL metamaterial unit cell was presented in [57], and the characteristics of a cloak constructed with the proposed cell were investigated. Instead of the approaches derived from conventional rectangular TL unit cells, in [18, 42], a unit cell based on a non-orthogonal TL grid was proposed for realizing arbitrary full-tensor parameters. Based on the coordinate transformation technique, the topology uses non-orthogonal TL segments, contrary to adding additional branches intersecting at a node. This topology enables a direct extension to a three-dimensional (3-D) adaptation of the implementation.

Metamaterials have been typically realized as periodic structures with a unit cell size that is electrically much smaller than the effective wavelength in the host medium. A periodic array of inclusion-based materials can be designed to behave as an effective electromagnetic medium. In [45], a medium with simultaneously negative permittivity and permeability was demonstrated. Split-ring resonators (SRRs) [31] and continuous thin wires [30, 32] were used in a periodic array to form a left-handed medium. An SRR based 2-D cloak was realized in [39] as shown in Figure 1.1(b). In [51], a 3-D double-negative (DNG) metamaterial unit cell composed of SRRs and wire medium was designed

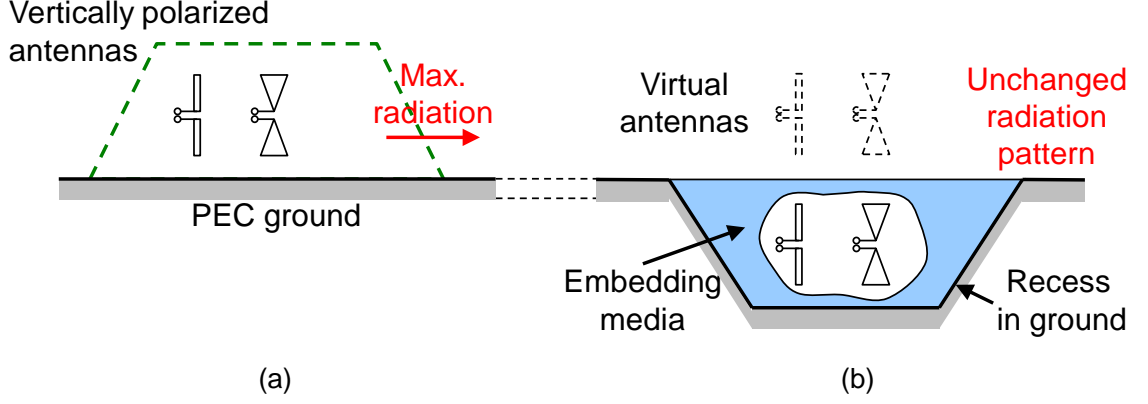


**Figure 1.3.** Objective: an antenna and embedding media without protrusion above the ground plane, radiating vertically polarized fields with maximum radiation in the horizon on the ground plane. (a) Electrical configuration. (b) Physical configuration.

and tested. As an alternative to the wire media, an inductor-capacitor electric resonator (ELC) was proposed for designing the effective permittivity of the metamaterial in [40].

## 1.2 Motivation

Out of numerous novel possibilities of modifying the antenna or array geometry without changing the intended radiation characteristics, the motivation for the research is formation of a virtual antenna—making an embedded physical source in a ground recess appear as if it transmits and receives above a ground plane without physical presence. Of particular interest is to design and fabricate a material-embedded monopole antenna that radiates vertically polarized fields with a pattern maximum in the horizon on the ground plane, as illustrated in Figure 1.3(b). The structure is flush with the surrounding ground plane, making the design suitable for conformal applications. Figure 1.3(a) shows the equivalent original configuration.

The first step towards the objective is a design of a 2-D TL metamaterial radiation configuration to validate the approach. A coordinate transformation maps a 2-D line source above a flat ground plane into a source embedded in transformation-derived media inside a ground recess such that the embedded-recessed line source has the same 2-D far-field

radiation characteristics as the original configuration. This is followed by the extension of the presented TL metamaterial design to a resonator-based metamaterial counterpart for TE polarization in two dimensions. Then, implementation of the embedded 3-D monopole setup is the final step.

Potential applications of the virtual antenna include removal of blade antennas on aircraft bodies without affecting their radiation characteristics. Protrusions by blade antennas are undesirable because they cause drag, especially problematic for high-speed vehicles. In addition, they are prone to mechanical failure at the attachment point to the aircraft body. Replacing blade antennas with completely flush structures having physical antennas positioned hidden inside the mounting platform will remove such shortcomings.

Here we note that the use of coordinate transformation and negative-index materials is a passive material approach and it is not the unique method to realize virtual antennas. An active material approach (i.e., an electronically controlled phased array antenna, which can be thought as an active metasurface) can be also devised to form virtual antennas. For the flush physical configuration in Figure 1.3(b) that is devoid of physical structures above the ground plane, impressed current sources can be placed over the recess aperture to reproduce the same radiation pattern. In this approach, the exact amplitude and phase distribution of the impressed sources are dependent on the specific antenna—they need to be adjusted based on the radiation properties of the physical antenna. In contrast, the TE/TO based media can effectively virtualize any embedded antenna configuration in principle. In practice, this requires synthesis of the transformation media that responds to the primary source fields of arbitrary polarization and this poses a significant challenge. Therefore, any simplification of the TE/TO design requirement can be taken advantage of if plausible in application scenarios. Implementing such transformation media using passive metamaterials typically involves careful consideration of the embedded antenna properties, e.g., polarization, as will be discussed in this study.

### 1.3 Contributions

The novel contributions of this dissertation work are:

- *Design of a 3-D virtual antenna configuration based on the TE/TO-based metamaterials:* The media embedding a physical antenna in a ground recess is designed such that the far-zone radiation pattern of a virtual antenna radiating above a flat conducting ground plane is reproduced. Effectively, the lateral dimension of a NIM lens is shortened by treating the truncation effect.
- *Experimental validation of a 2-D virtual antenna configuration by a combination of a finite-sized NIM lens and a TE/TO-based impedance-matcher:* The horizontal dimension of the NIM lens is finite and the associated truncation effect is compensated by anisotropic media. Furthermore, the physical source in this study is backed by conducting recess walls unlike in studies of experimental NIM lenses in the literature. Using a metamaterial-embedded probe, formation of a virtual source is experimentally confirmed in transmission-line metamaterials. As an extension using resonant inclusion-based metamaterials, it is confirmed that the embedding media translates radiation from the physical line source located inside a recess to a virtual location above the ground plane.
- *Design and fabrication of transmission-line and inclusion-based metamaterials based on unit cells having non-orthogonal boundaries for realizing anisotropic medium parameters:* A non-orthogonal TL grid unit cell and a right parallelogram prism unit cell with resonant inclusions are introduced in this work and used to synthesize anisotropic tensor parameters.
- *Development of a homogenization algorithm for anisotropic media:* For synthesizing a fully anisotropic medium in a plane, a homogenization method based on  $S$ -parameters of a finite-thickness slab is developed. The homogenized medium pa-

rameters are found from plane-wave scattering analysis of a metamaterial slab under three different illumination directions.

- *An assembly method for 3-D metamaterials based on unit cells:* The NIM and the matcher metamaterials are held together in position using layers of perforated standard copier papers. Arrays of square holes were created in the papers using the laser cutter to form a holder and spacer for the metamaterial.

## **CHAPTER 2**

### **DESIGN BASED ON COORDINATE TRANSFORMATION**

In this chapter, coordinate transformation design of a material-embedded physical source for virtual antenna formation will be presented. Material parameters of the embedding media will be derived.

#### **2.1 3-D Virtual Antenna Radiation**

##### **2.1.1 Coordinate Transformation**

Consider a monopole antenna mounted on an infinite PEC ground plane as shown in Figure 2.1(a). This configuration radiates a vertically polarized field with the pattern maximum located in the horizon. It is desired that the monopole and embedding media are arranged inside a ground recess, such that this new arrangement has the same far-zone radiation pattern as the original setup. The target physical configuration is completely flush with the surrounding ground plane and there is no physical structure above the surrounding ground plane.

Following the TE/TO design technique, a coordinate transformation from the original (virtual) to the transformed (physical) systems leads to specifications of the material parameter values for realizing the intended physical configuration. We choose to transform only the coordinate normal to the ground plane; the region bounded by the dashed contour and the ground plane in Figure 2.1(a) is folded below the ground plane in Figure 2.1(b). The transformation from  $z$  to  $z'$  is kept continuous along  $z' = 0$  to ensure that the interface



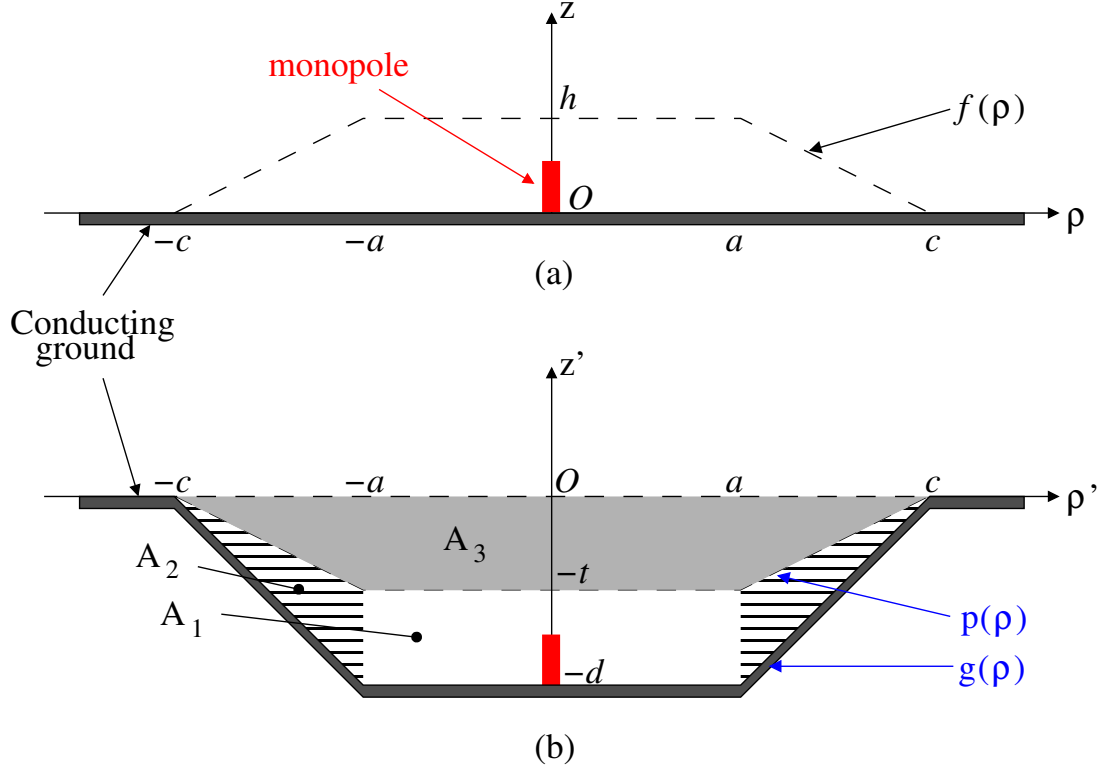


**Figure 2.1.** The coordinate transformation between the original (virtual) and embedded (physical) radiation configurations. (a) Original configuration. (b) Embedded configuration.

with free space is reflectionless. The following transformation can be introduced between the original  $(\rho, \phi, z)$  and the transformed  $(\rho', \phi', z')$  cylindrical coordinate systems:

$$\rho = \rho', \quad \phi = \phi', \quad z = \begin{cases} z', & z' \geq 0 \\ \frac{f(\rho)}{p(\rho')} z', & p(\rho') \leq z' < 0 \\ \frac{f(\rho)}{p(\rho') - g(\rho')} [z' - g(\rho')], & g(\rho') \leq z' < p(\rho') \end{cases} \quad (2.1)$$

One first finds the Jacobian matrix of the transformation  $\mathbf{A}$  and then computes the relative permittivity and permeability tensors from  $\mathbf{A}$  for regions  $A_1$ ,  $A_2$  and  $A_3$  [41]. The non-zero elements of  $3 \times 3$  tensors are found to be

$$\epsilon'_{\rho'\rho'} = \mu'_{\phi'\phi'} = \frac{h}{d-t}, \quad \epsilon'_{z'z'} = \frac{d-t}{h} \quad \text{in } A_1, \quad (2.2)$$

$$\epsilon'_{\rho'\rho'} = \mu'_{\phi'\phi'} = \frac{h}{d-t}, \quad \epsilon'_{\rho'z'} = \epsilon'_{z'\rho'} = \frac{hd}{(c-a)(d-t)},$$

$$\epsilon'_{z'z'} = \frac{d-t}{h} + \frac{hd^2}{(c-a)^2(d-t)} \quad \text{in } A_2, \quad (2.3)$$

$$\epsilon'_{\rho'\rho'} = \mu'_{\phi'\phi'} = -\frac{h}{t}, \quad \epsilon'_{z'z'} = -\frac{t}{h} \quad \text{in } A_3. \quad (2.4)$$

We now remove primes in (2.2)–(2.4) to interpret them as medium parameters in the original space [41].

Of particular interest is the choice  $h = t = d/2$ , with which  $A_1$  and  $A_3$  become isotropic media,  $A_1$  is free space and  $A_3$  is a negative-index material (NIM) with  $\epsilon = \mu = -1$ . For the lateral dimension, choosing  $a = c/2 = d$ , yields following anisotropic tensor parameters:

$$\boldsymbol{\epsilon} = \boldsymbol{\mu} = \begin{bmatrix} 1 & 1 & 0 \\ 1 & 2 & 0 \\ 0 & 0 & 1 \end{bmatrix} \quad (2.5)$$

for the remaining region  $A_2$ . It is noted that all constituent blocks  $A_1$ ,  $A_2$ , and  $A_3$  are homogeneous. The free space region in  $z > 0$  is denoted as  $A_0$ .

### 2.1.2 Numerical Results

The radiation characteristics of an embedded monopole are numerically investigated using COMSOL Multiphysics, which is a commercial full-wave analysis tool based on the finite-element technique. At the design frequency  $f = f_0$ , a  $0.25\lambda_0$ -long thin-wire monopole antenna radiates in two different configurations. Dimensional parameters of the ground recess were chosen to be  $a = d = c/2 = 2h = 2t = \lambda_0$ . Snapshots of the distributions of the  $\phi$ -directed magnetic field  $\mathbf{H}$  are compared in Figures 2.2(a)–2.2(b).

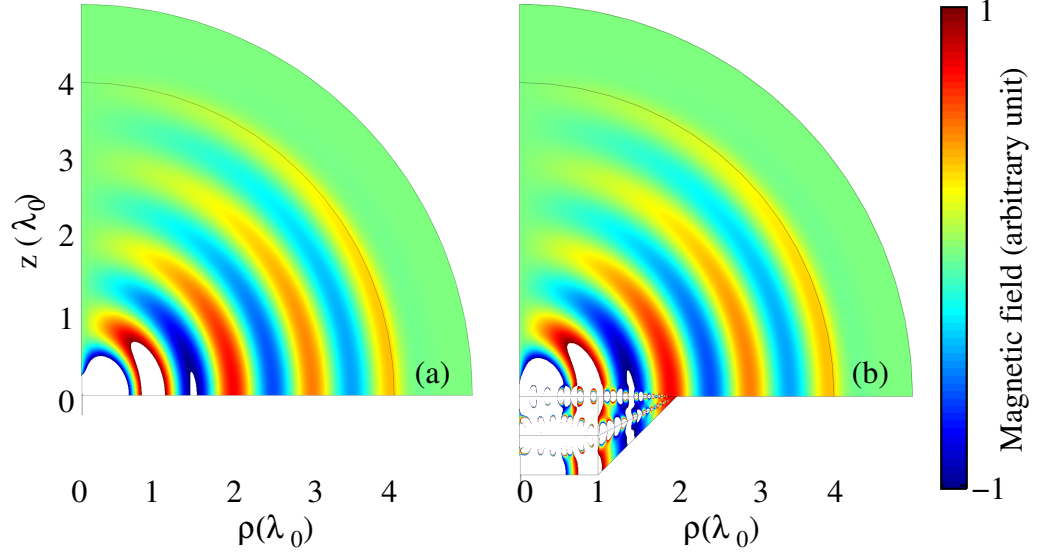


**Figure 2.2.** Snapshots of the  $H_\phi$  distributions. (a) Original configuration. (b) Embedded configuration.

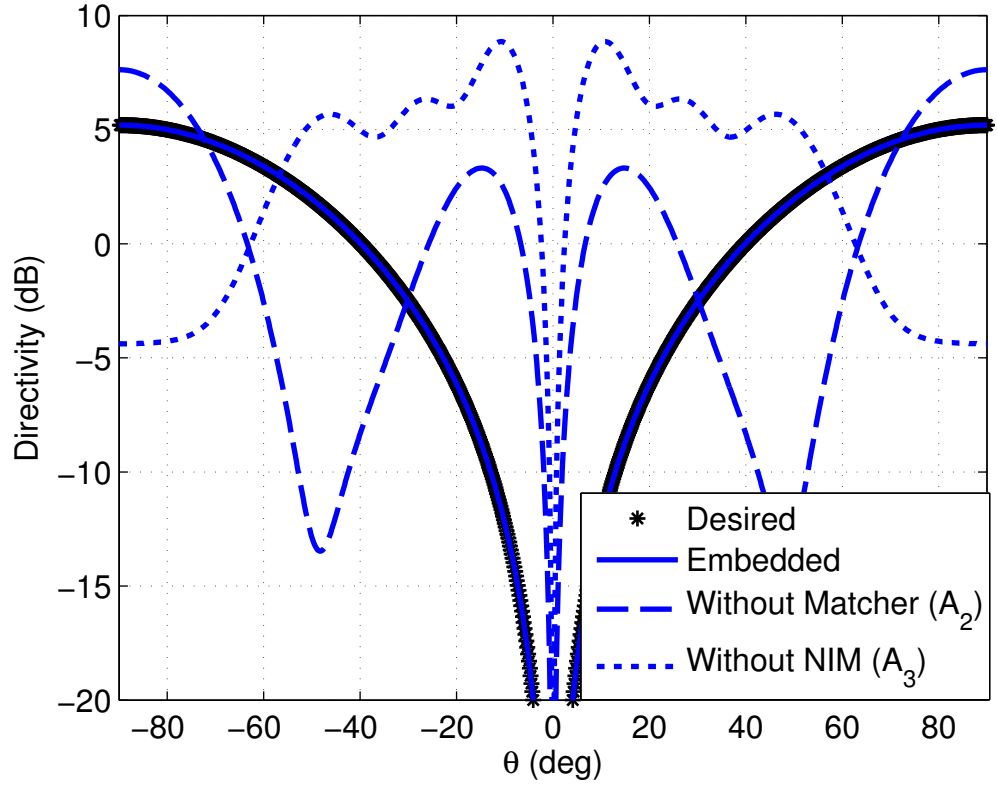


**Figure 2.3.** Simulated directivity patterns for the embedded configuration, compared with the cases without  $A_2$  and without  $A_3$ .

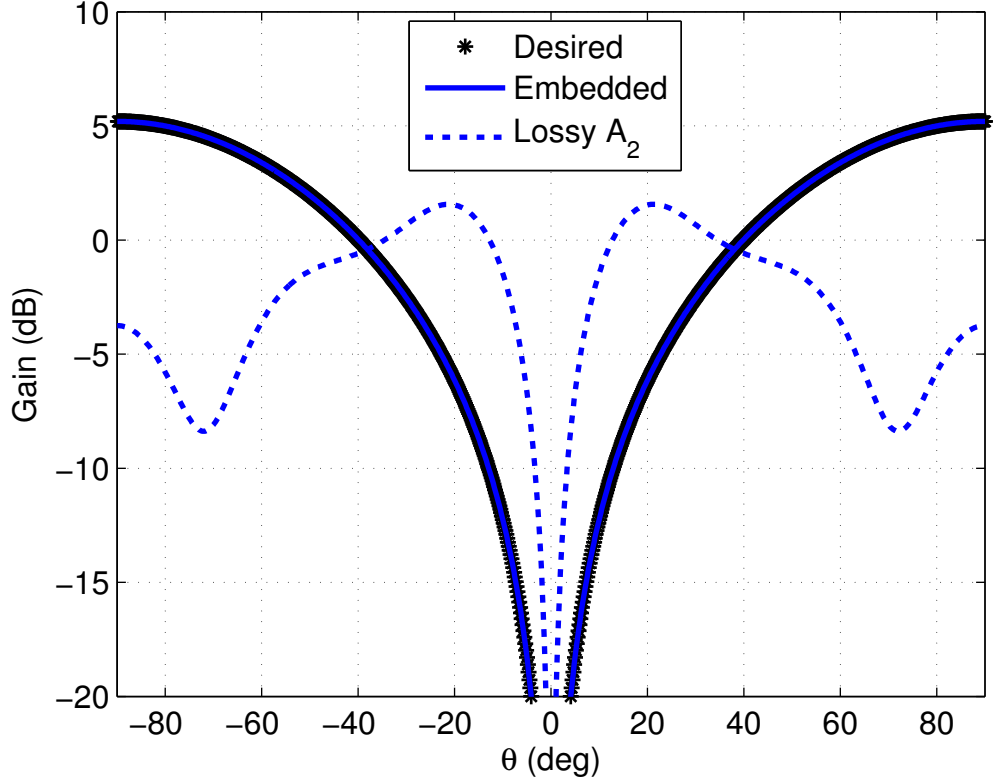


**Figure 2.4.** Simulated far-field gain patterns for the embedded configuration, compared with the case of a lossy  $A_2$  region having effective medium parameters  $\epsilon = \mu = 1 - j100$ .

Figure 2.2(a) shows the distribution of  $H_\phi$  for the original configuration. For the antenna radiating embedded inside the recess, the same field distribution is reproduced away from the immediate neighborhood of the boundary at  $z = 0$  as shown in Figure 2.2(b). The high field values observed along the boundary of the NIM with neighboring volumes are associated with the surface-mode plasmon resonances [38]. In order to assess the effect of the individual media, simulated far-field directivity patterns are plotted in Figure 2.3. It is observed that both  $A_2$  and  $A_3$  are essential for achieving the desired device function. The effect of  $A_2$  is further investigated by replacing  $A_2$  with an effective medium having  $\epsilon = \mu = 1 - j100$ . In Figure 2.4, simulated far-field gain patterns are plotted. We observe that gain drops by 8.95 dB at  $\theta = 90^\circ$  (in the horizon).

## 2.2 2-D Virtual Line Source Radiation

### 2.2.1 Coordinate Transformation

One can also define a 2-D variant of the design. We consider an electric line source in the  $+\hat{z}$  direction radiating at  $(x, y) = (0, s)$  in free space above a PEC ground in the  $x - z$  plane in the Cartesian  $(x, y, z)$  coordinate system as shown in Figure 2.5(a). The configuration is infinite and uniform in  $z$ . It is desired that a line source and embedding media be arranged inside a ground recess such that the new arrangement has the same 2-D far-zone radiation pattern as the original configuration at the operating frequency. The resulting radiation configuration is completely flush with the surrounding ground plane and there is no physical structure above the  $x - z$  plane. Figure 2.5(b) depicts the physical configuration. Similar to the 3-D monopole configuration, the following transformation can be defined:

$$x = x', \quad z = z', \quad y = \begin{cases} y', & y' \geq 0 \\ \frac{f(x')}{p(x')}y', & p(x') \leq y' < 0 \\ \frac{f(x')}{p(x')-g(x')}[y' - g(x')], & g(x') \leq y' < p(x') \end{cases} \quad (2.6)$$

From the Jacobian matrix of the transformation  $\mathbf{A} = \partial(x', y', z')/\partial(x, y, z)$  we compute the relative permittivity and permeability tensors from  $\mathbf{A}$  for regions  $A_1$ ,  $A_2^-$ ,  $A_2^+$ , and  $A_3$  [41]. In the Cartesian bases, non-zero elements of the  $3 \times 3$  permittivity and permeability tensors are found to be

$$\mu'_{x'x'} = \epsilon'_{z'z'} = \frac{h}{d-t}, \quad \mu'_{y'y'} = \frac{d-t}{h} \quad \text{in } A_1, \quad (2.7)$$

$$\mu'_{x'x'} = \epsilon'_{z'z'} = \frac{h}{d-t}, \quad \mu'_{x'y'} = \mu'_{y'x'} = \frac{hd}{(a-c)(d-t)},$$

$$\mu'_{y'y'} = \frac{d-t}{h} + \frac{hd^2}{(c-a)^2(d-t)} \quad \text{in } A_2^-, \quad (2.8)$$

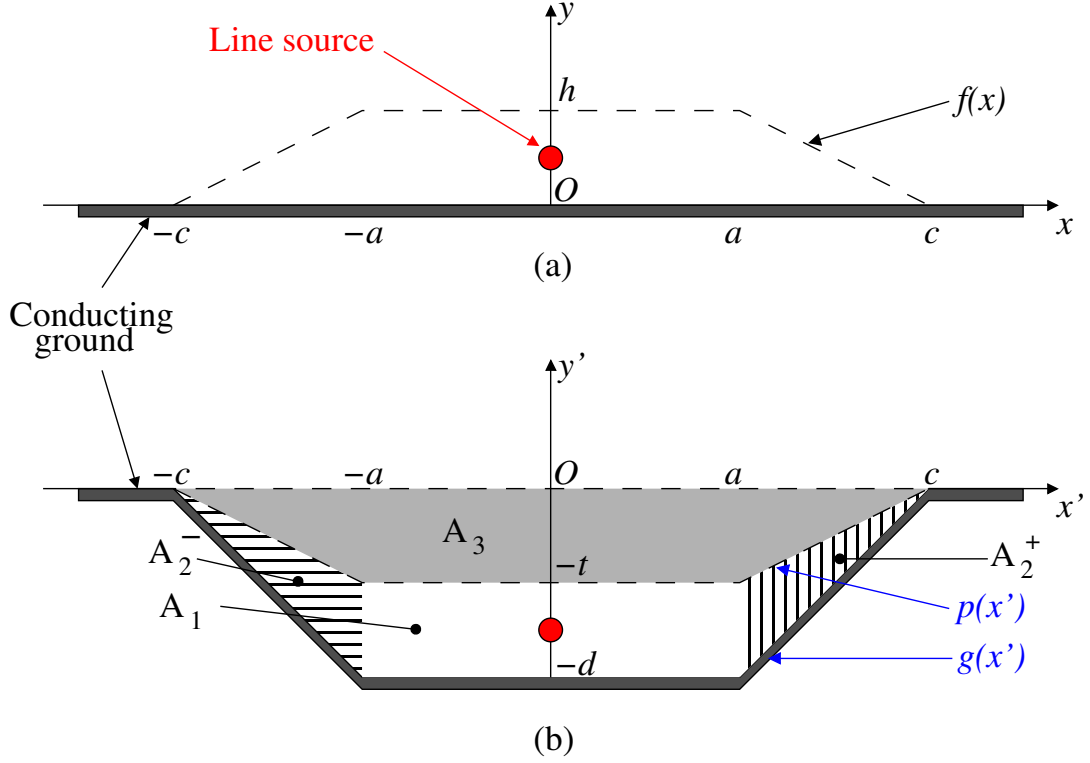


**Figure 2.5.** The 2-D coordinate transformation between the original (virtual) and embedded (physical) radiation configurations. (a) Original configuration. (b) Embedded configuration.

$$\mu'_{x'x'} = \epsilon'_{z'z'} = \frac{h}{d-t}, \quad \mu'_{x'y'} = \mu'_{y'x'} = \frac{hd}{(c-a)(d-t)},$$

$$\mu'_{y'y'} = \frac{d-t}{h} + \frac{hd^2}{(c-a)^2(d-t)} \quad \text{in } A_2^+, \quad (2.9)$$

$$\mu'_{x'x'} = \epsilon'_{z'z'} = -\frac{h}{t}, \quad \mu'_{y'y'} = -\frac{t}{h} \quad \text{in } A_3. \quad (2.10)$$

Similar to the 3-D design, choosing  $h = t = d/2$ , and  $a = c/2 = d$  results with  $A_1$  free space and  $A_3$  negative-index material (NIM) with  $\epsilon = \mu = -1$ . For the remaining regions  $A_2^-$  and  $A_2^+$  the anisotropic tensor parameters are:

$$\epsilon = \mu = \begin{bmatrix} 1 & \mp 1 & 0 \\ \mp 1 & 2 & 0 \\ 0 & 0 & 1 \end{bmatrix}. \quad (2.11)$$

### 2.2.2 Numerical Results

The radiation characteristics of an embedded line source are numerically investigated using COMSOL Multiphysics. At the design frequency  $f = f_0$ , a line source along the  $+\hat{z}$  direction is placed  $\lambda_0/4$  above the ground plane at  $(x, y) = (0, 0.25\lambda_0)$  for the original, and at  $(0, -0.75\lambda_0)$  for the embedded configurations, respectively. Dimensional parameters of the ground recess were chosen to be  $a = d = c/2 = 2h = 2t = \lambda_0$ . Snapshots of the  $z$ -directed electric field distributions are compared in Figure 2.6(a)–2.6(b) for the two configurations. It can be observed that the same field distribution is reproduced away from the immediate neighborhood of the boundary at  $y = 0$ . In Figure 2.7, simulated far-field directivity patterns with and without the anisotropic media are compared. It is observed that removing  $A_3$  distorts the pattern significantly. In contrast to the 3-D case of Figure 2.7, we note that the relatively small impact of  $A_2^\pm$  is due to the broadside radiation for the line source radiation configuration.

A flat NIM slab in a right-handed medium [2] can act like a planar lens as shown in Figure 2.8. Images of the source are formed inside and outside of the lens. In principle, the design relies on the same physics as a NIM superlens [29], with two major distinctions. First, the horizontal dimension of the NIM lens is finite and the associated truncation effect is compensated by the impedance-matching region  $A_2$ . Second, no extreme accuracy is required for the effective medium parameters in practical antenna applications [16], unlike in the sub-diffraction-limit near-field lensing applications [48].

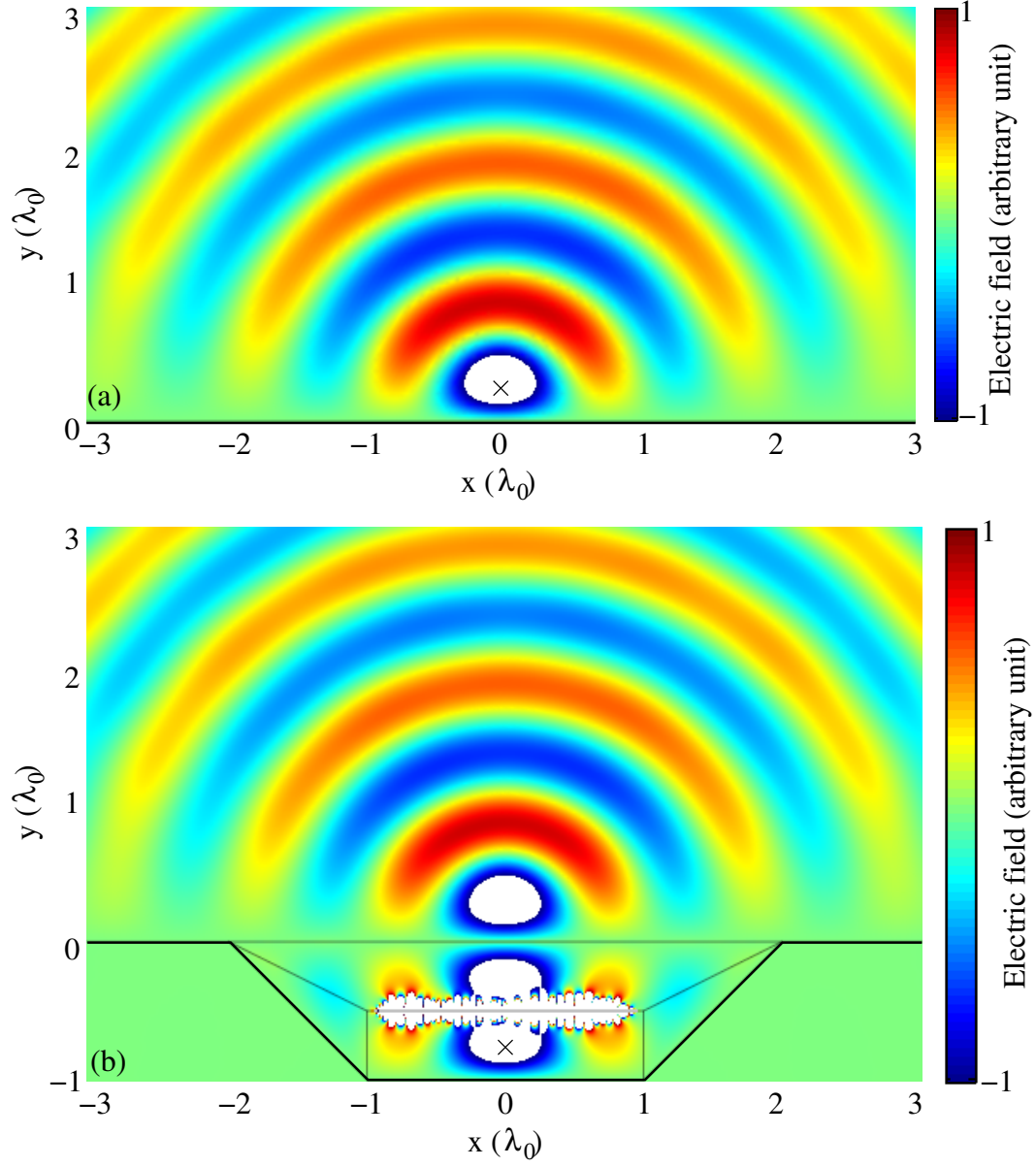


**Figure 2.6.** Snapshots of the  $E_z$  distributions. (a) Original configuration. (b) Embedded configuration.



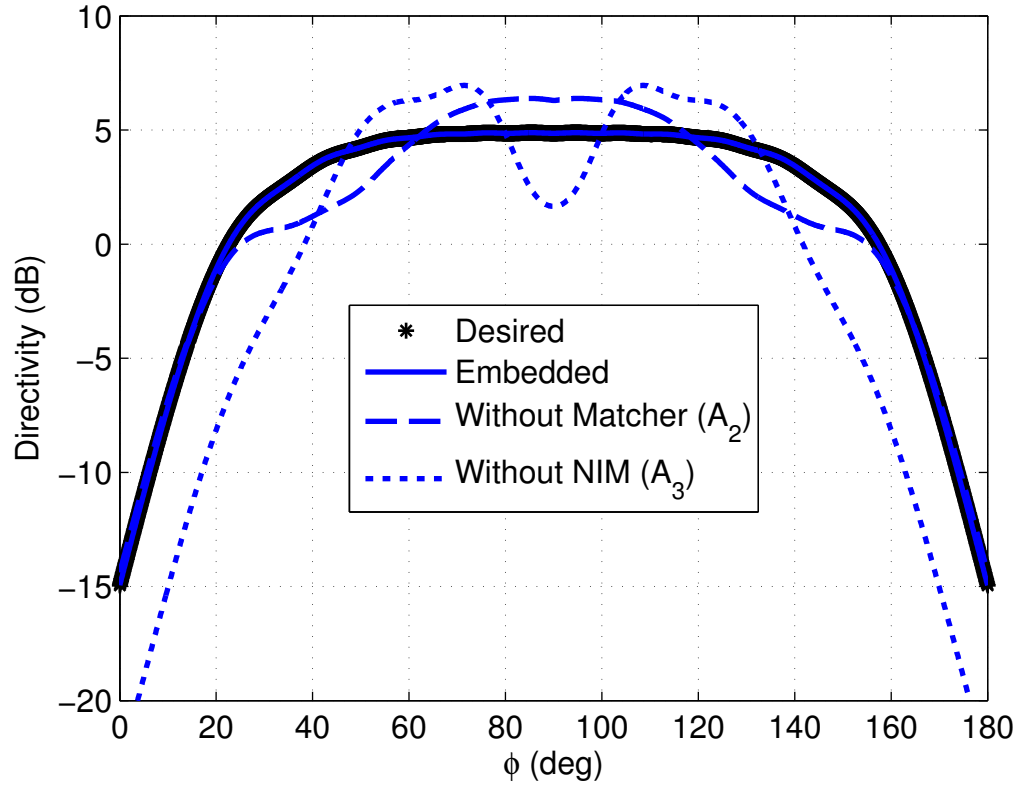


**Figure 2.7.** Simulated 2-D directivity patterns for the embedded configuration, compared with the cases without  $A_2^\pm$  and without  $A_3$ .

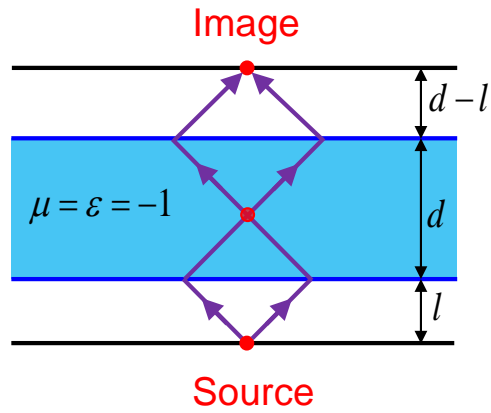


**Figure 2.8.** Refraction through a flat NIM slab with  $\epsilon = \mu = -1$  in free space.

## CHAPTER 3

### ANISOTROPIC METAMATERIALS AND HOMOGENIZATION

Metamaterials are artificially tailored materials providing desired configuration of electromagnetic fields. Often they are designed to be composed of unit cells in a periodic arrangement. Provided that the electrical dimensions of the unit cell remain much smaller than the wavelength, these materials can be characterized with homogeneous material parameters. As such, the homogenized refractive index  $n$  and the impedance  $z$  are useful parameters for describing the effective medium properties of a material.

Homogenization methods attempt to establish an equivalence between an inhomogeneous structure and a homogeneous structure via the comparison of measured and calculated quantities. A standard homogenization method [4, 47, 49] utilizes the scattering parameters ( $S$ -parameters), i.e., reflection and transmission coefficients for a plane wave illuminating the synthesized medium, of a metamaterial unit cell. Field averaging [46] is another approach in the extraction of the medium parameters, involving calculation of the macroscopic fields by local field averaging on unit cell boundaries. Parameter retrieval methods have been applied to a variety of common metamaterial structures [31, 32, 45]. Equivalent metamaterial parameters for the fabricated designs have been experimentally verified [50].

In this chapter, a standard parameter retrieval technique based on the scattering parameters of a unit cell under periodic boundary conditions is reviewed. Next, a design method for a TL metamaterial unit cell capable of representing full-tensor material parameters is summarized. Finally, a technique to calculate the anisotropic tensor parameters of a 2-D resonant inclusion-based metamaterial is introduced.

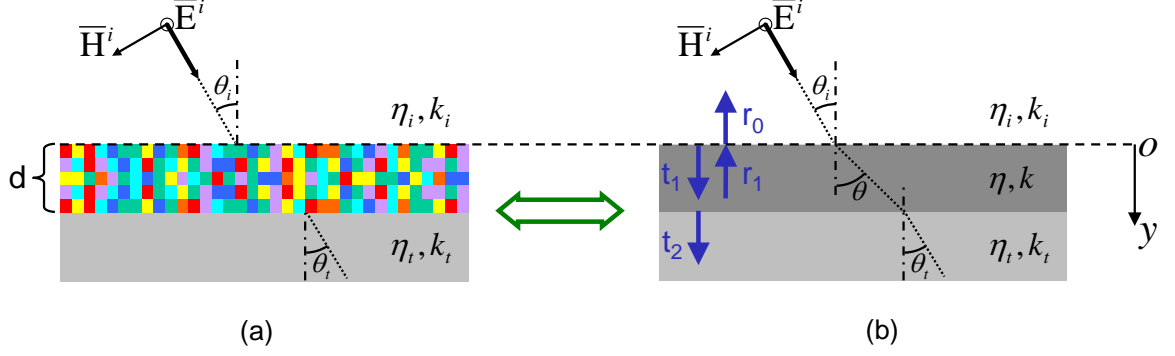


**Figure 3.1.** Homogenization based on the reflection and transmission coefficients. (a) An inhomogeneous metamaterial slab of thickness  $d$ . (b) Equivalent homogeneous slab with the retrieved refractive index  $n$  and impedance  $z$ .

### 3.1 A Conventional Homogenization Method

We consider the reflection and transmission of a plane wave of the TE polarization (electric field polarized normal to the page) incident on a planar slab of an inhomogeneous material of thickness  $d$  as shown in Figure 3.1. The dual configuration of a TM-polarized plane wave illumination can be treated similarly.

Plane wave is illuminating the slab from a medium with an intrinsic impedance  $\eta_i$  and a wavenumber  $k_i$ . The equivalent homogeneous medium parameters of the metamaterial slab are denoted by  $\eta$  and  $k$ . The medium behind the metamaterial slab has the corresponding parameters as  $\eta_t, k_t$ . From the phase matching condition at  $y = 0$  and  $y = d$ , one finds

$$k_i \sin \theta_i = k \sin \theta = k_t \sin \theta_t. \quad (3.1)$$

We define the wave impedances  $Z_i, Z$  and  $Z_t$  as

$$Z_i = \frac{\eta_i}{\cos \theta_i}, \quad Z = \frac{\eta}{\cos \theta}, \quad Z_t = \frac{\eta_t}{\cos \theta_t}. \quad (3.2)$$

Enforcing the boundary conditions, i.e. the continuity of total tangential electric and magnetic fields along the slab boundary, in terms of the reflection and transmission coefficients

as illustrated in Figure 3.1, one finds

$$\begin{aligned} 1 + r_0 &= t_1 + r_1 \\ \frac{1 - r_0}{Z_i} &= \frac{t_1 - r_1}{Z}, \end{aligned} \quad (3.3)$$

at  $y = 0$ , and

$$\begin{aligned} t_1 e^{-jk_y d} + r_1 e^{jk_y d} &= t_2 \\ \frac{t_1 e^{-jk_y d} - r_1 e^{jk_y d}}{Z} &= \frac{t_2}{Z_t}, \end{aligned} \quad (3.4)$$

at  $y = d$ , respectively, where  $k_y = k \cos \theta$ . From (3.3)–(3.4), one obtains

$$e^{jk_y d} = \frac{(1 - r_0)/Z_i + (1 + r_0)/Z}{t_2/Z_t + t_2/Z} \quad (3.5)$$

$$e^{-jk_y d} = \frac{(1 - r_0)/Z_i - (1 + r_0)/Z}{t_2/Z_t - t_2/Z}. \quad (3.6)$$

Then, the inversion follows from multiplying (3.5) and (3.6), which yields

$$Z = \pm \sqrt{\frac{t_2^2 - (1 + r_0)^2}{t_2^2/Z_t^2 - [(1 - r_0)/Z_i]^2}}. \quad (3.7)$$

Inserting  $Z$  into the sum of (3.5) and (3.6) gives

$$k_y d = \cos^{-1} \left( \frac{(1 - r_0^2)/Z_i + t_2^2/Z_t}{t_2[(1 + r_0)/Z_t + (1 - r_0)/Z_i]} \right) + 2\pi m \quad (3.8)$$

where  $m$  is an integer. From (3.1), one finds

$$k = \pm \sqrt{(k \cos \theta)^2 + (k \sin \theta)^2} = \pm \sqrt{(k_y)^2 + (k_i \sin \theta_i)^2}. \quad (3.9)$$

Finally,

$$\eta = Z \frac{k_y}{k}. \quad (3.10)$$

Index of refraction and the intrinsic impedance of the medium relative to the free space are given by  $n = n' - jn'' = k/k_0$  and  $z = z' - jz'' = \eta/\eta_0$ , respectively, where  $k_0$  and  $\eta_0$  denote the free space parameters. The relative permeability  $\mu$  and permittivity  $\epsilon$  are related to  $n$  and  $z$  via

$$\mu = nz, \quad (3.11)$$

$$\epsilon = \frac{n}{z}. \quad (3.12)$$

For passive materials, the branch of the square root in (3.7) and the sign of the inverse cosine function in (3.8) is chosen appropriately such that  $z' \geq 0$  and  $n'' \geq 0$ . The imaginary part of the refractive index is uniquely determined by this condition. On the other hand, the real part  $n'$  is due further interpretation by the correct choice of branch associated with the inverse cosine function. The correct branch can be chosen by requiring that the metamaterial does not exhibit magnetic behavior in the low-frequency limit, i.e.,  $\mu \rightarrow 1$  as  $f \rightarrow 0$  ( $f$  = frequency), as long as no magnetic constituent material is used in the design. For this purpose, the  $S$ -parameter analysis for the unit cell of a metamaterial in a periodic structure can be performed where  $d$  is much smaller than the wavelength at the operation frequency. Once the correct branch index  $m$  is determined, the frequency is continuously increased to the frequency of interest. The procedure applies to both homogeneous and inhomogeneous materials identically.

## 3.2 Non-Orthogonal Grids in 2-D Metamaterials

In this Section, a TL metamaterial unit cell based on a non-orthogonal transmission-line grid for creating an arbitrary full-tensor medium parameter is presented. Effective medium parameters in standard Cartesian coordinates are subsequently found.

A non-orthogonal grid TL metamaterial unit cell is illustrated in Figure 3.2. The shunt node configuration for 2-D TL networks is used to model 2-D electromagnetic fields in the

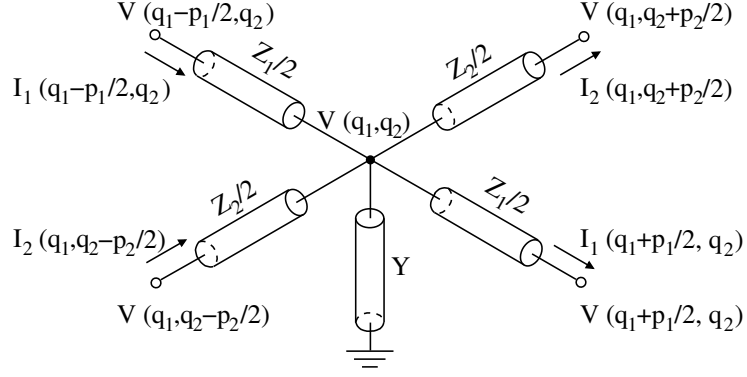


**Figure 3.2.** A perspective view of the non-orthogonal grid TL metamaterial unit cell.

TE polarization [5]. Total series impedances along the two branches are  $Z_1$  and  $Z_2$ , and a shunt admittance  $Y$  is connected between the junction of the series branches and the ground as shown in Figure 3.2. Voltages and currents at the four nodes are also indicated. The advantage of this unit cell over the conventional unit cell approaches [2] is that both branches are allowed to run in fixed, but arbitrary directions. In the non-orthogonal  $(q_1, q_2, q_3)$  coordinate system shown in Figure 3.3,  $q_1$  and  $q_2$  axes are aligned with the series branches. The unit vector sets  $\hat{q}_1, \hat{q}_2, \hat{q}_3$ , which are built along the coordinate axes, and  $\hat{q}^1, \hat{q}^2, \hat{q}^3$ , which are built normal to constant-coordinate surfaces are also defined, where  $\hat{q}_3 = \hat{q}^3 = \hat{z}$ . The lengths of the series branches are  $p_1$  and  $p_2$ , and the height of the shunt branch is  $p_3$ . The geometrical arrangement of immittances constitutes a non-orthogonal grid unit cell or a parallelogram unit cell as indicated with a dashed-line contour in Figure 3.3.

The effective medium parameters represented by the non-orthogonal unit cell can be found by establishing an isomorphism between Kirchoff's circuital laws and 2-D Maxwell's equations in the TE polarization. In the limit  $p_1, p_2 \rightarrow 0$ , application of Kirchoff's voltage law along the two branches gives

$$\frac{\partial V}{\partial q_1} = -(\hat{q}_3 \cdot \hat{q}_1 \times \hat{q}_2) Z'_1 \left( \frac{I_1}{p_2} \right), \quad (3.13)$$

$$\frac{\partial V}{\partial q_2} = -(\hat{q}_3 \cdot \hat{q}_1 \times \hat{q}_2) Z'_2 \left( \frac{I_2}{p_1} \right). \quad (3.14)$$

Kirchoff's current law applied at the junction results in

$$\frac{\partial}{\partial q_1} \left( \frac{I_1}{p_2} \right) + \frac{\partial}{\partial q_2} \left( \frac{I_2}{p_1} \right) = -(\hat{q}_3 \cdot \hat{q}_1 \times \hat{q}_2) Y' V. \quad (3.15)$$

Primed immittances in (3.13)–(3.15) are per-unit-length quantities of the unprimed counterparts for the medium being modeled. For TE-polarized 2-D electromagnetic fields  $\mathbf{E}$  ( $E_3 = \hat{q}_3 \cdot \mathbf{E}$ ) and  $\mathbf{H}$  ( $H_1 = \hat{q}_1 \cdot \mathbf{H}$ ,  $H_2 = \hat{q}_2 \cdot \mathbf{H}$ ), the source-free time-harmonic Maxwell's equations written in the  $(q_1, q_2, q_3)$  system take the same form as in the Cartesian system, i.e.,

$$\nabla \times \mathbf{E} = -j\omega\mu_0 \boldsymbol{\mu} \mathbf{H}, \quad (3.16)$$

$$\nabla \times \mathbf{H} = j\omega\epsilon_0 \boldsymbol{\epsilon} \mathbf{E}, \quad (3.17)$$

due to the form-invariant nature of Maxwell's equations [52]. In (3.16)–(3.17),  $\boldsymbol{\mu}$  and  $\boldsymbol{\epsilon}$  are permeability and permittivity tensors relative to the free space. The network equations (3.13)–(3.15) and Maxwell's equations (3.16)–(3.17) are isomorphic with the following substitutions

$$E_3 \rightarrow -\frac{V}{p_3}, \quad H_1 \rightarrow -\frac{I_2}{p_1}, \quad H_2 \rightarrow \frac{I_1}{p_2} \quad (3.18)$$

for field quantities and

$$\boldsymbol{\epsilon} \rightarrow \hat{q}_3 \hat{q}_3 \frac{\hat{q}_3 \cdot \hat{q}_1 \times \hat{q}_2}{j\omega\epsilon_0} Y', \quad (3.19)$$

$$\boldsymbol{\mu} \rightarrow \frac{\hat{q}_3 \cdot \hat{q}_1 \times \hat{q}_2}{j\omega\mu_0} (\hat{q}_1 \hat{q}_1 Z'_2 + \hat{q}_2 \hat{q}_2 Z'_1) \quad (3.20)$$

for medium parameters. Therefore, expressed in the  $(q_1, q_2, q_3)$  system, the effective medium parameters represented by the non-orthogonal grid are

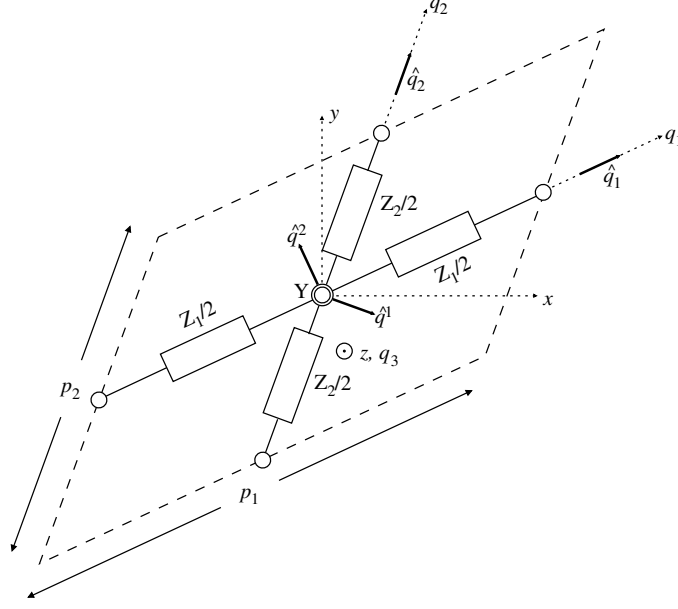


**Figure 3.3.** Top view of the non-orthogonal grid (or parallelogram) TL metamaterial unit cell.

$$\begin{bmatrix} \mu_{11} & 0 \\ 0 & \mu_{22} \end{bmatrix} = \frac{\hat{q}_3 \cdot \hat{q}_1 \times \hat{q}_2}{j\omega\mu_0} \begin{bmatrix} Z'_2 & 0 \\ 0 & Z'_1 \end{bmatrix}, \quad \epsilon_{33} = \frac{\hat{q}_3 \cdot \hat{q}_1 \times \hat{q}_2}{j\omega\epsilon_0} Y', \quad (3.21)$$

where primed immittances in (3.21) are per-unit-length quantities of the unprimed counterparts for the medium being modeled.

### 3.2.1 Coordinate Transformation

In order to utilize the non-orthogonal grid to synthesize anisotropic medium with a full tensor in Cartesian system, it is of interest to find the relative effective medium parameters (3.21) in the  $(x, y, z)$  system, which are denoted by

$$\begin{bmatrix} \mu_{xx} & \mu_{xy} \\ \mu_{yx} & \mu_{yy} \end{bmatrix}, \quad \epsilon_{zz}. \quad (3.22)$$

Restricting our attention to reciprocal media, we impose the condition  $\mu_{yx} = \mu_{xy}$  in (3.22). Consider a coordinate transformation from  $(q_1, q_2, q_3)$  to  $(x, y, z)$ . The Jacobian matrix



$\mathbf{A} = \partial(x, y, z)/\partial(q_1, q_2, q_3)$  of the transformation is equal to

$$\mathbf{A} = \begin{bmatrix} \hat{x} \cdot \hat{q}_1 & \hat{x} \cdot \hat{q}_2 & \hat{x} \cdot \hat{q}_3 \\ \hat{y} \cdot \hat{q}_1 & \hat{y} \cdot \hat{q}_2 & \hat{y} \cdot \hat{q}_3 \\ \hat{z} \cdot \hat{q}_1 & \hat{z} \cdot \hat{q}_2 & \hat{z} \cdot \hat{q}_3 \end{bmatrix} = \begin{bmatrix} \hat{q}_1 & \hat{q}_2 & \hat{q}_3 \end{bmatrix}, \quad (3.23)$$

where  $\hat{q}_1, \hat{q}_2, \hat{q}_3$  are written as column vectors in Cartesian components. The medium tensor parameters in the  $(x, y, z)$  system are then expressed by  $\mathbf{A}\epsilon\mathbf{A}^T/|\mathbf{A}|$  and  $\mathbf{A}\mu\mathbf{A}^T/|\mathbf{A}|$  [41]. Let  $\hat{q}_1$  and  $\hat{q}_2$  in Figure 3.3 make angles  $\phi_1$  and  $\phi_2$  from the  $+x$  direction in the  $x-y$  plane so that

$$\begin{aligned} \hat{q}_1 &= \hat{x} \cos \phi_1 + \hat{y} \sin \phi_1, \\ \hat{q}_2 &= \hat{x} \cos \phi_2 + \hat{y} \sin \phi_2. \end{aligned} \quad (3.24)$$

One finds the medium parameters in the  $(x, y, z)$  system to be [18]

$$\mu_{xx} = \frac{\mu_{11} \cos^2 \phi_1 + \mu_{22} \cos^2 \phi_2}{\sin(\phi_2 - \phi_1)}, \quad (3.25)$$

$$\mu_{yx} = \mu_{xy} = \frac{\mu_{11} \sin \phi_1 \cos \phi_1 + \mu_{22} \sin \phi_2 \cos \phi_2}{\sin(\phi_2 - \phi_1)}, \quad (3.26)$$

$$\mu_{yy} = \frac{\mu_{11} \sin^2 \phi_1 + \mu_{22} \sin^2 \phi_2}{\sin(\phi_2 - \phi_1)}, \quad (3.27)$$

$$\epsilon_{zz} = \frac{\epsilon_{33}}{\sin(\phi_2 - \phi_1)}. \quad (3.28)$$

The following useful inverse relations can be obtained from (3.25)–(3.28):

$$\mu_{11} = \frac{\mu_{xx} \sin^2 \phi_2 - \mu_{yy} \cos^2 \phi_2}{\sin(\phi_1 + \phi_2)}, \quad (3.29)$$

$$\mu_{22} = -\frac{\mu_{xx} \sin^2 \phi_1 - \mu_{yy} \cos^2 \phi_1}{\sin(\phi_1 + \phi_2)}, \quad (3.30)$$

$$\epsilon_{33} = \epsilon_{zz} \sin(\phi_2 - \phi_1), \quad (3.31)$$

$$\tan \phi_1 = -\frac{\mu_{yy} \cos \phi_2 - \mu_{xy} \sin \phi_2}{\mu_{xx} \sin \phi_2 - \mu_{xy} \cos \phi_2}. \quad (3.32)$$

### 3.2.2 Design Procedure

In the  $x - y$  plane, three independent medium parameters  $\mu_{xx}$ ,  $\mu_{xy}$ , and  $\mu_{yy}$  in (3.22) need to be synthesized using a non-orthogonal grid TL unit cell in a typical design problem. This requires three independent design parameters for a unit cell. In comparison, the non-orthogonal unit cell in Figure 3.3 has four design parameters in the  $x - y$  plane, namely  $Z_1$ ,  $Z_2$ ,  $\phi_1$ , and  $\phi_2$ . Design flexibility is achieved with this one extra degree of freedom. For example, one grid direction can be chosen in an arbitrary direction. If there is an interface between two media, one grid can run always along the interface. Then, the remaining three parameter values are uniquely determined to synthesize the given arbitrary full-tensor parameters.

In a design problem for full-tensor material parameters (3.22), the following design procedure can be taken. First, determine one grid angle, e.g.  $\phi_1$ , in a preferred direction. Second, determine the angle  $\phi_2$  according to (3.32). Finally, two diagonal elements of  $\boldsymbol{\mu}$  in the  $(q_1, q_2, q_3)$  system are found from (3.29)–(3.30). The value of  $\epsilon_{33}$  is found from (3.31). These medium parameters of the  $(q_1, q_2, q_3)$  system determine the immittance values  $Y'$  and  $Z'_1$ ,  $Z'_2$  in the non-orthogonal grid unit cell via (3.21).

The values of  $Y$  and  $Z_1$ ,  $Z_2$  are equal to [5]

$$Y = Y' \frac{p_1(\hat{q}^2 \cdot \hat{q}_2 p_2)}{p_3} = j\omega\epsilon_0\epsilon_{33} \frac{p_1 p_2}{p_3}, \quad (3.33)$$

$$Z_1 = Z'_1 \frac{(\hat{q}^1 \cdot \hat{q}_1 p_1) p_3}{p_2} = j\omega\mu_0\mu_{22} \frac{p_1 p_3}{p_2}, \quad (3.34)$$

$$Z_2 = Z'_2 \frac{(\hat{q}^2 \cdot \hat{q}_2 p_2) p_3}{p_1} = j\omega\mu_0\mu_{11} \frac{p_2 p_3}{p_1}. \quad (3.35)$$

They can be expressed relative to their free space counterparts:

$$Y_0 = j\omega\epsilon_0 \frac{p_1 p_2}{p_3}, \quad Z_{10} = j\omega\mu_0 \frac{p_1 p_3}{p_2}, \quad Z_{20} = j\omega\mu_0 \frac{p_2 p_3}{p_1}. \quad (3.36)$$

The parameters  $Y_0$  and  $Z_{10}$ ,  $Z_{20}$  in (3.36) are the cell immittance values associated with an orthogonal grid corresponding to free space with periods  $p_1$  and  $p_2$  in the  $\hat{x}$  and  $\hat{y}$  directions,

respectively. Via (3.36), (3.33)–(3.35) can be rewritten as

$$Y = \epsilon_{33}Y_0, \quad Z_1 = \mu_{22}Z_{10}, \quad Z_2 = \mu_{11}Z_{20}. \quad (3.37)$$

We can split the total immittances of (3.37) into host and load contributions by defining

$$Y = Y_0 + Y_l, \quad Z_1 = Z_{10} + Z_{1l}, \quad Z_2 = Z_{20} + Z_{2l}. \quad (3.38)$$

In practice, the immittance values  $Y_0$ ,  $Z_{10}$ ,  $Z_{20}$  may be realized by an unloaded host TL grid and  $Y_l$ ,  $Z_{1l}$ ,  $Z_{2l}$  may be implemented with lumped load elements. Full-tensor anisotropic medium synthesis with non-orthogonal unit cell structures is simple, because no additional load elements are needed compared with the conventional orthogonal grid unit cells.

### 3.3 *S*-Parameter-Based Homogenization of an Anisotropic Medium

Consider a plane wave of the TM polarization with a  $y$ -directed magnetic field incident on a material slab with homogeneous and anisotropic medium parameters given by

$$\boldsymbol{\epsilon} = \begin{bmatrix} \epsilon_{xx} & \epsilon_{xz} \\ \epsilon_{zx} & \epsilon_{zz} \end{bmatrix}, \quad \mu_{yy}, \quad (3.39)$$

which are relative to the free space values in Cartesian  $(x, y, z)$  coordinate system as illustrated in Figure 3.4(a). The TE-polarized plane wave incidence case can be treated similarly. We note that  $\epsilon_{xz} = \epsilon_{zx}$  for reciprocal media. For TM-polarized 2-D electromagnetic fields, the source-free time-harmonic Maxwell's curl equations are

$$\nabla \times \mathbf{E} = -j\omega\mu_0\mu_{yy}\mathbf{H}, \quad (3.40)$$

$$\nabla \times \mathbf{H} = j\omega\epsilon_0\boldsymbol{\epsilon}\mathbf{E}. \quad (3.41)$$

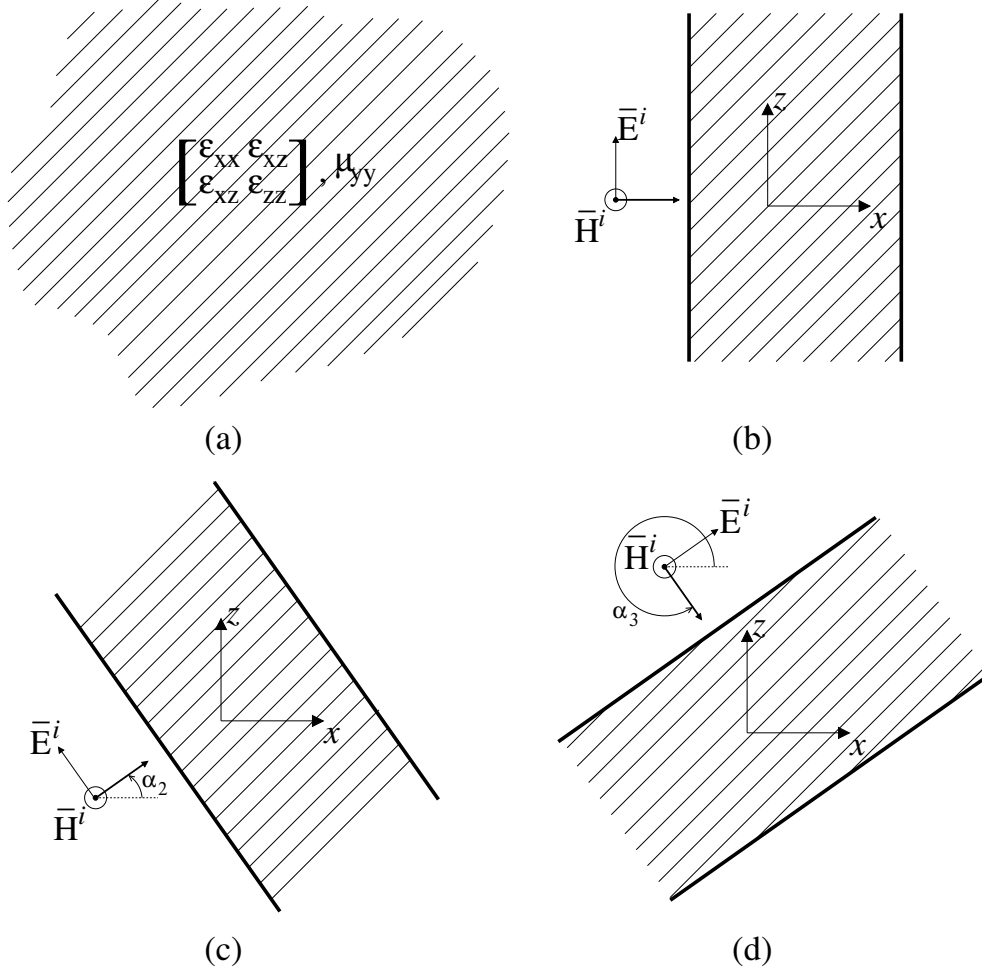


**Figure 3.4.** Homogenization of an anisotropic medium under normally incident plane wave illuminations. (a) An anisotropic medium in free space. (b)  $\alpha_1 = 0$ . (c)  $\alpha_2$ . (d)  $\alpha_3$ .

From (3.40) and (3.41), one finds the dispersion relationship as

$$\frac{\epsilon_{xx}}{|\epsilon|} k_x^2 + \frac{\epsilon_{xz}}{|\epsilon|} 2k_x k_z + \frac{\epsilon_{zz}}{|\epsilon|} k_z^2 = \mu_{yy} \quad (3.42)$$

where

$$|\epsilon| = \epsilon_{xx}\epsilon_{zz} - \epsilon_{xz}^2 \quad (3.43)$$

is the determinant of the  $2 \times 2$  permittivity tensor in the  $xz$ -plane.  $k_x$  and  $k_z$  are the

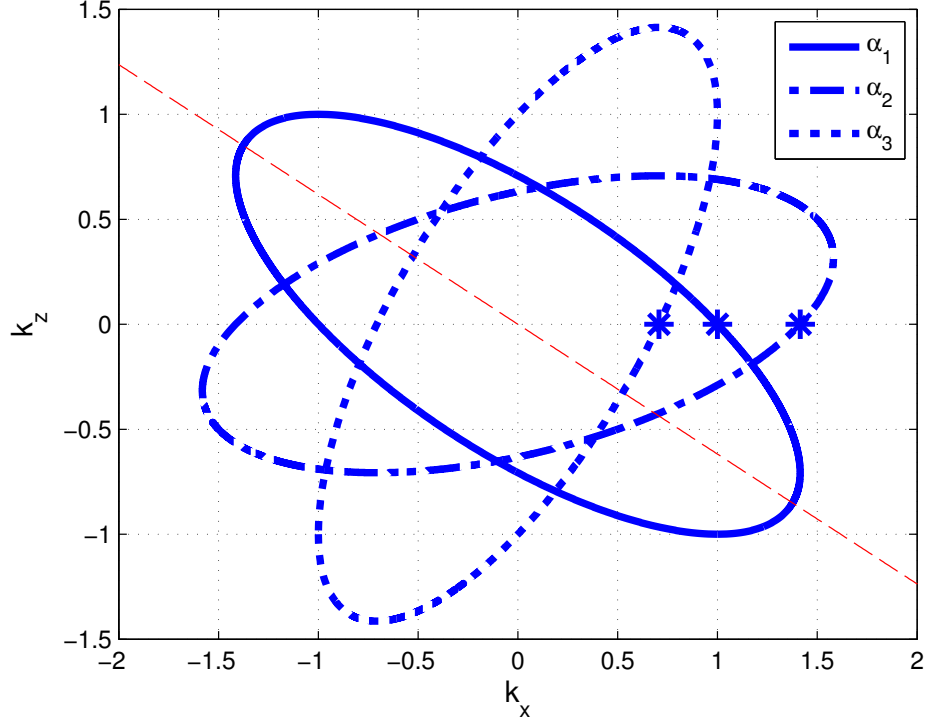


**Figure 3.5.** Elliptical dispersion curves for an anisotropic medium in 2-D.

wavenumbers relative to their free space values in the  $x$  and  $z$  directions, respectively. The dispersion equation (3.42) defines a unique ellipse centered at the origin. Characterized by three parameters, it can be expressed as

$$Ak_x^2 + Bk_xk_z + Ck_z^2 = 1 \quad (3.44)$$

for some constants  $A$ ,  $B$ , and  $C$ .

Now we consider the homogenization of the medium by analyzing reflection and transmission of normally incident plane wave from a slab of this material in free space, where the direction of propagation makes an angle  $\alpha_i$  with the  $+x$  axis measured toward the  $+z$  axis as shown in Figure 3.4(b)–3.4(d). Using a standard parameter retrieval technique as described in Section 3.1, the homogenized relative refractive indices  $n_1, n_2, n_3$  and the normalized impedances  $z_1, z_2, z_3$  can be extracted at the design frequency  $f = f_0$ , for the

incident wave vectors  $\mathbf{k}_1, \mathbf{k}_2, \mathbf{k}_3$  associated with the angles  $\alpha_1, \alpha_2, \alpha_3$ , respectively. As illustrated in Figure 3.5, plane-wave scattering analysis of each case provides a data point on the dispersion diagram of the medium given by

$$\begin{bmatrix} k_{xi} & k_{zi} \end{bmatrix} = \begin{bmatrix} n_i & 0 \end{bmatrix} \begin{bmatrix} \cos \alpha_i & \sin \alpha_i \\ -\sin \alpha_i & \cos \alpha_i \end{bmatrix} \quad (3.45)$$

for  $i = 1, 2, 3$ . Using (3.45), (3.44) is solved for A, B, and C as

$$\begin{bmatrix} A \\ B \\ C \end{bmatrix} = \begin{bmatrix} k_{x1}^2 & k_{x1}k_{z1} & k_{z1}^2 \\ k_{x2}^2 & k_{x2}k_{z2} & k_{z2}^2 \\ k_{x3}^2 & k_{x3}k_{z3} & k_{z3}^2 \end{bmatrix}^{-1} \begin{bmatrix} 1 \\ 1 \\ 1 \end{bmatrix}, \quad (3.46)$$

We note that the relative permeability  $\mu_{yy}$  of the medium can be obtained from any of the three scattering analyses. Ideally,

$$\mu_{yy} = n_1 z_1 = n_2 z_2 = n_3 z_3. \quad (3.47)$$

as the unit cell dimensions reduce to zero. In practice, the retrieved values of  $\mu_{yy}$  obtained from different illumination directions are not expected to be the same. Finally,  $\epsilon_{xx}$ ,  $\epsilon_{xz}$ , and  $\epsilon_{zz}$  are expressed in terms of A, B, C, and  $\mu_{yy}$  via (3.42) and (3.44) as

$$\epsilon_{xx} = \mu_{yy}^{-1} \frac{4A}{4AC - B^2}, \quad (3.48)$$

$$\epsilon_{xz} = \mu_{yy}^{-1} \frac{2B}{4AC - B^2}, \quad (3.49)$$

$$\epsilon_{zz} = \mu_{yy}^{-1} \frac{4C}{4AC - B^2}. \quad (3.50)$$

## CHAPTER 4

### MICROSTRIP TL-METAMATERIAL DESIGN

The embedded current source design introduced in Chapter 2 can be implemented with TL metamaterials. Figure 4.1 shows the cross-sectional view of a line current embedded in transformation media in a ground recess. The medium parameters based on the coordinate transformation method were derived in Section 2.2. In this chapter, the 2-D effective medium is designed and fabricated using a microstrip TL network with practical conductor, dielectric, and load parameters suitable for fabrication and measurement. Furthermore, the unit cells incorporating a via hole for the shunt load are numerically optimized in terms of the homogenized medium parameters.

#### 4.1 Microstrip TL Metamaterial Cell Designs

A TL metamaterial unit cell model is shown in Figure 4.2(a). The shunt branch  $Y$  and the series branches  $Z_1$ ,  $Z_2$  are modeled in Figure 4.2(b). The host TL grid unit cell has branches of length  $p_1$  and  $p_2$  in their respective directions  $\hat{q}_1$  and  $\hat{q}_2$  with the characteristic

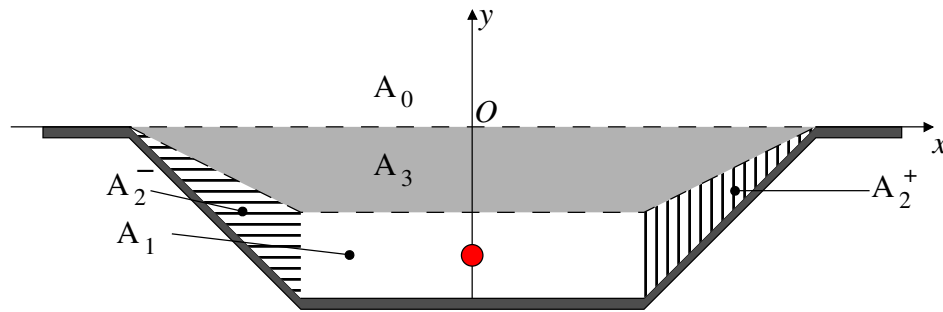


**Figure 4.1.** An embedded line source (red dot) inside a ground recess.

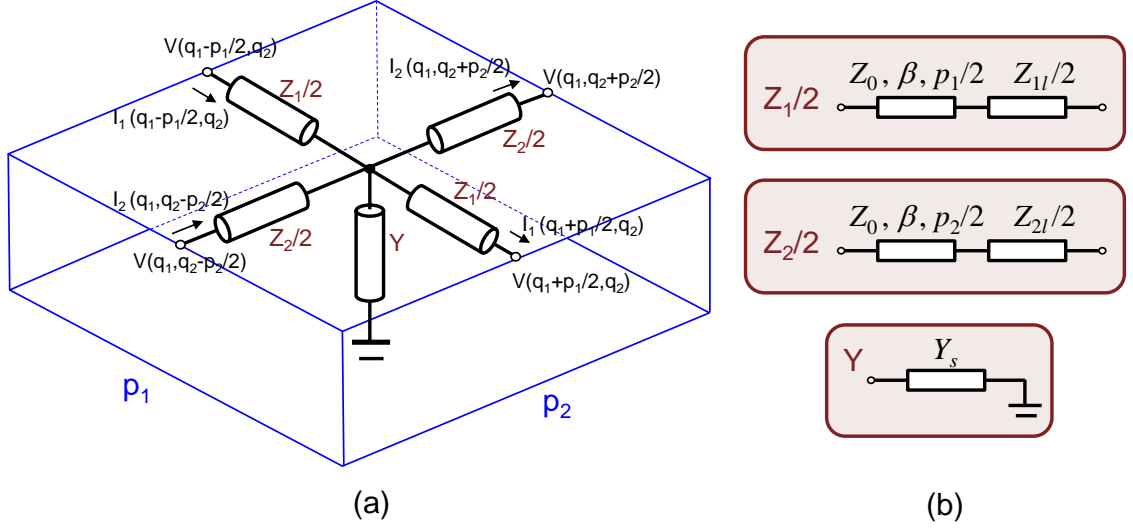


**Figure 4.2.** A generic 2-D TL metamaterial unit cell. (a) 2-D periodic unit cell. (b) Definitions for  $Z_1$ ,  $Z_2$  and  $Y$ .

impedance  $Z_0$ . Load impedances are denoted by  $Z_{il}$  in the series branches, for  $i = 1, 2$ . The admittance  $Y_s$  denotes the shunt branch load admittance. Voltage and current at each node are also indicated.

A Bloch analysis can be performed for this 2-D periodic structure. The dispersion relation can be found by solving for propagating modes with a vector wavenumber

$$\mathbf{k} = \hat{x}k_x + \hat{y}k_y. \quad (4.1)$$

Defining primitive lattice vectors in the spatial domain as

$$\mathbf{p}_1 = \hat{q}_1 p_1, \quad \mathbf{p}_2 = \hat{q}_2 p_2, \quad (4.2)$$

the periodic boundary conditions are



$$\begin{bmatrix} V(q_1 + \frac{p_1}{2}, q_2) \\ I_1(q_1 + \frac{p_1}{2}, q_2) \end{bmatrix} = e^{-j\mathbf{k} \cdot \mathbf{p}_1} \begin{bmatrix} V(q_1 - \frac{p_1}{2}, q_2) \\ I_1(q_1 - \frac{p_1}{2}, q_2) \end{bmatrix}, \quad (4.3)$$

$$\begin{bmatrix} V(q_1, q_2 + \frac{p_2}{2}) \\ I_2(q_1, q_2 + \frac{p_2}{2}) \end{bmatrix} = e^{-j\mathbf{k} \cdot \mathbf{p}_2} \begin{bmatrix} V(q_1, q_2 - \frac{p_2}{2}) \\ I_2(q_1, q_2 - \frac{p_2}{2}) \end{bmatrix}. \quad (4.4)$$

Using (4.3)–(4.4) in Kirchhoff's voltage law for the two series branches and current law at the junction gives four linear equations for four quantities  $V(q_1 - p_1/2, q_2)$ ,  $I_1(q_1 - p_1/2, q_2)$ ,  $V(q_1, q_2 - p_2/2)$ , and  $I_2(q_1, q_2 - p_2/2)$ . The periodic structure allows a non-trivial solution when the determinant of the coefficient matrix is equal to zero. The resulting dispersion relation is given by [10]

$$\begin{aligned} & B_1 D_1 [\cos(k_2 p_2) - B_2 C_2 - A_2 D_2] \\ & + B_2 D_2 \left[ \cos(k_1 p_1) - B_1 C_1 - A_1 D_1 - \frac{B_1 D_2 D_s}{B_s} \right] = 0 \end{aligned} \quad (4.5)$$

where  $A_i, B_i, C_i, D_i$  are the  $ABCD$  parameters [35] of the transmission matrices in the series branches and the shunt branch.  $k_1, k_2$  are the Bloch wavenumbers in the associated directions. In their general form, the  $ABCD$  matrices are equal to

$$\begin{bmatrix} A_i & B_i \\ C_i & D_i \end{bmatrix} = \begin{bmatrix} c_i + j s_i Y_0 Z_{il}/2 & j s_i Z_0 + c_i Z_{il}/2 \\ j s_i Y_0 & c_i \end{bmatrix} \quad (4.6)$$

for the two series branches, and

$$\begin{bmatrix} A_s & B_s \\ C_s & D_s \end{bmatrix} = \begin{bmatrix} 1 & Y_s \\ 1 & 1 \end{bmatrix} \quad (4.7)$$

for the shunt branch  $Y$ , where

$$\begin{aligned} s_1 &= \sin\left(\beta \frac{p_1}{2}\right), & s_2 &= \sin\left(\beta \frac{p_2}{2}\right), \\ c_1 &= \cos\left(\beta \frac{p_1}{2}\right), & c_2 &= \cos\left(\beta \frac{p_2}{2}\right). \end{aligned} \quad (4.8)$$

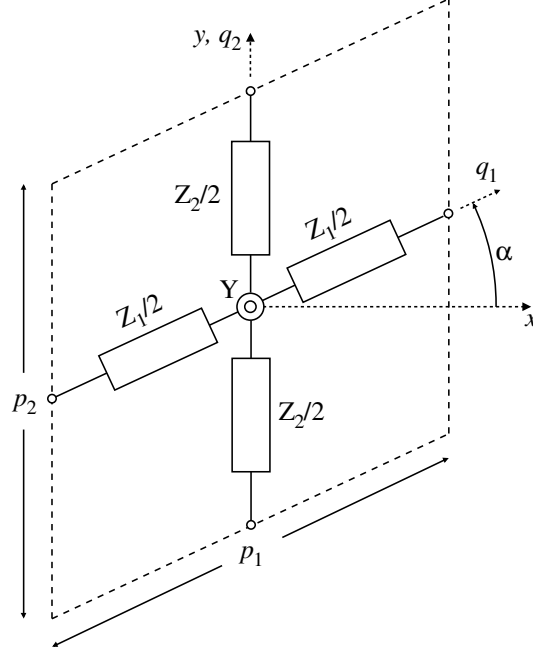


**Figure 4.3.** Top view of the 2-D TL metamaterial unit cell in a non-orthogonal grid.

Load values in the series branches are calculated using the Bloch impedance relation for power flow in each branch direction. For the two series branches,  $Z_{B1}$  and  $Z_{B2}$  are given by [10]

$$Z_{B1} = \frac{Z_0 \tan\left(\frac{\beta p_1}{2}\right) - jZ_{1l}/2}{\tan\left(\frac{k_1 p_1}{2}\right)}, \quad (4.9)$$

$$Z_{B2} = \frac{Z_0 \tan\left(\frac{\beta p_2}{2}\right) - jZ_{2l}/2}{\tan\left(\frac{k_2 p_2}{2}\right)}.$$

where  $k_1 p_1$  and  $k_2 p_2$  are per-unit-cell phase delays,  $\beta = \omega/v_p$  is the propagation constant, and  $v_p$  is the phase velocity of the interconnected TL. The frequency of operation is  $f_0 = \omega/2\pi$ . The shunt branch load values are calculated using the dispersion relation (4.5).

A generic non-orthogonal TL unit cell is shown in Figure 4.3, where branches are aligned in the  $\hat{q}_1$  and  $\hat{q}_2$  directions, respectively. The  $\hat{q}_1$  axis makes an angle  $\alpha$  from the  $+\hat{x}$  direction in the  $x - y$  plane. An unloaded orthogonal unit cell with  $p_1 = p_2 = p_0$  and  $\alpha = 0$  represents the free space regions  $A_0$  and  $A_1$ . For an unloaded host TL grid, (4.9)

reduces to

$$Z_x = Z_y = Z_B = \frac{Z_0 \tan \frac{\beta p_0}{2}}{\tan \frac{k_0 p_0}{2}}. \quad (4.10)$$

From (4.5), the dispersion equation for an unloaded host TL grid is

$$s_1 c_1 \left[ s_2^2 - \sin^2 \left( k_2 \frac{p_2}{2} \right) \right] + s_2 c_2 \left[ s_1^2 - \sin^2 \left( k_1 \frac{p_1}{2} \right) \right] = 0. \quad (4.11)$$

For  $p_1 = p_2 = p_0$ , (4.11) simplifies to

$$\sin^2 \left( \frac{k_1 p_0}{2} \right) + \sin^2 \left( \frac{k_2 p_0}{2} \right) = 2 \sin^2 \left( \frac{\beta p_0}{2} \right). \quad (4.12)$$

The region  $A_3$  is a NIM superlens, so it can be realized by an orthogonal unit cell having capacitively-loaded series branches of equal length with  $p_1 = p_2 = p_0$ , and an inductively-loaded shunt branch [2]. Regions  $A_2^-$  and  $A_2^+$  are anisotropic impedance-matching blocks with non-zero off-diagonal tensor elements. A non-orthogonal unit cell with reactively loaded branches is used to synthesize the anisotropic parameters. Following the design procedure described in Subsection 3.2.2 to realize the particular set of medium parameters for  $A_2^\pm$  in (2.11), we obtain  $\mu_{11} = \sqrt{2}$ ,  $\mu_{22} = 1/\sqrt{2}$ ,  $\epsilon_{33} = 1/\sqrt{2}$  and  $\alpha = \pm 45^\circ$ . With the choice of  $\hat{q}_2 = \hat{y}$ , we select  $p_1 = p_0 / \cos \alpha = p_0 \sqrt{2}$  and  $p_2 = p_0$  such that vertical grids from the two adjoining regions  $A_2^\pm$  and  $A_3$  coincide for a smooth transition across the common boundary.

Series load impedances  $Z_{1l} = j\omega L_{Z1} + (j\omega C_{Z1})^{-1}$  and  $Z_{2l} = j\omega L_{Z2} + (j\omega C_{Z2})^{-1}$  are calculated using (4.9). For branch  $i$  ( $i = 1, 2$ ),  $C_{Zi}$  or  $L_{Zi}$  are given by

$$\begin{aligned} C_{Zi} &= \frac{1}{2\omega} \left( Z_0 \tan \frac{\beta p_i}{2} - Z_B \tan \frac{k_i p_i}{2} \right)^{-1}, \\ L_{Zi} &= \frac{2}{\omega} \left( Z_B \tan \frac{k_i p_i}{2} - Z_0 \tan \frac{\beta p_i}{2} \right). \end{aligned} \quad (4.13)$$

Finally the shunt branch load values,  $C_Y$  or  $L_Y$ , are calculated via inserting (4.6)–(4.7), and (4.13) into (4.5).

The coordinate transformation leading to the physical configuration in Figure 4.1 has been deliberately chosen to give homogeneous medium parameters in each region. As a result, medium parameters are discontinuous across every interface between two neighboring regions. Hence, a unit cell positioned along a medium boundary needs to be carefully designed. The boundary element for each such interface is constructed by superposing the properties of the two media on both sides of the interface [1].

## 4.2 Numerical Results

Full-wave analysis of the design was performed using Ansys HFSS to validate the TL metamaterial design for the embedded probe current radiation. Microstrip line on a low-loss dielectric substrate is selected as the TL structure. The substrate is chosen to be Rogers RT/duroid 5880 of thickness 1.524 mm. The trace width is 0.762 mm with  $p_0 = \lambda_0/10 = 8.83$  mm. The design frequency is selected to be  $f_0 = 1.607$  GHz with  $Z_B = 76.2 \Omega$ . For  $A_2^-$  and  $A_2^+$ , load values are calculated to be  $C_{Z1} = 4.6$  pF,  $L_{Z2} = 2.02$  nH and  $L_Y = 80.81$  nH. The  $A_3$  loads are found to be  $C_{Z1} = C_{Z2} = 1.0$  pF and  $L_Y = 6.1$  nH.

For the original and embedded radiation configurations, current probes injecting 1 A are placed at  $(x, y) = (0, 0.25\lambda_0)$  and  $(0, -0.75\lambda_0)$ , respectively. Figures 4.4 and 4.5 show snapshots of the  $\hat{z}$  component of the electric field in a constant- $z$  plane 1.524 mm above the microstrip surface. Only the  $x > 0$  region is simulated using a magnetic mirror boundary at  $x = 0$ . The two distributions show an excellent agreement that cannot be visually distinguished in  $y > 0$ .

Finally, we design a shunt load as a lumped component on the microstrip surface connected to the ground through a plated via hole in order to model its physical realization accurately. Figure 4.6 shows the unit cell of  $A_3$ . The exact effect of a via hole is taken into account using full-wave analysis of the NIM unit cell at the design frequency of

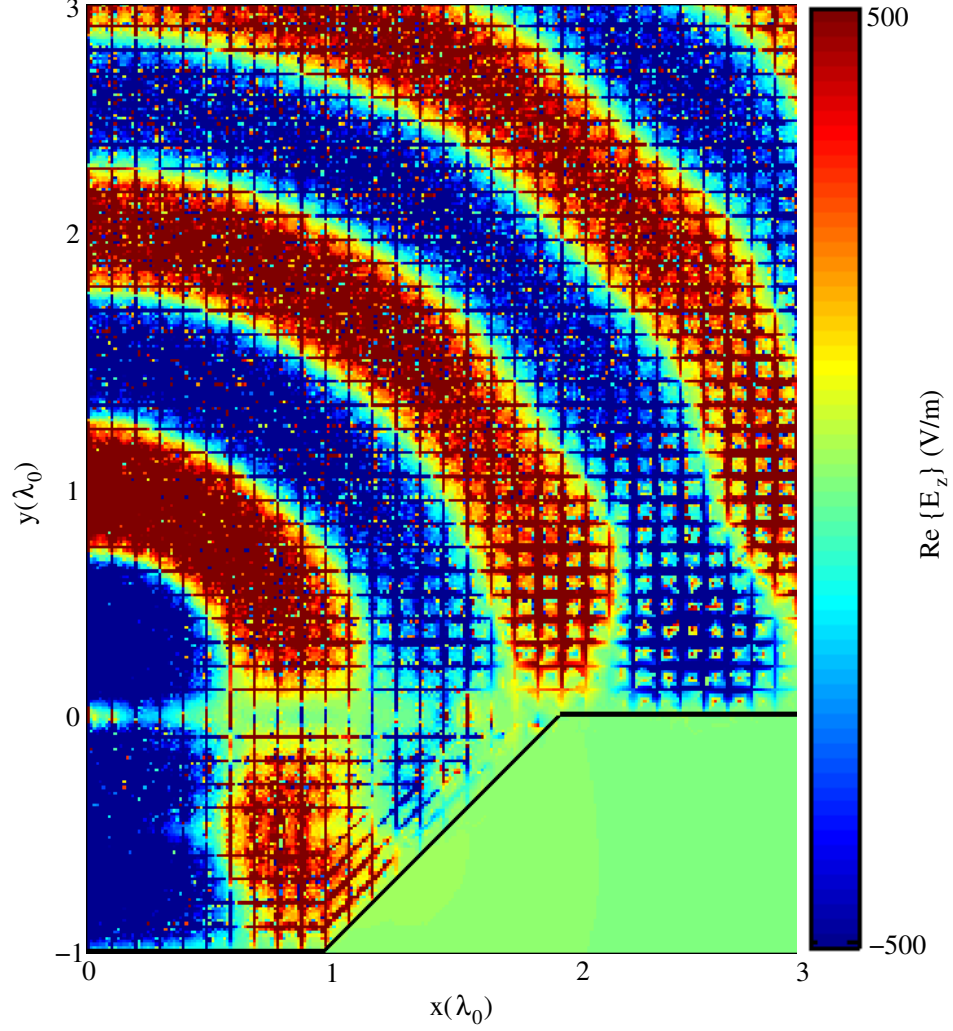


**Figure 4.4.** Snapshot of  $E_z$  for the embedded probe configuration.

$f_0 = 1.607$  GHz. The standard parameter retrieval technique described in Section 3.1 is used in the extraction of the medium parameters at  $f = f_0$ . The only distinction is that the ports in the TL cell design are microstrip ports rather than plane-wave ports. The nominal load values of the NIM unit cell are optimized such that the homogenized medium parameters match those of a NIM superlens. For a via diameter of 0.381 mm, Figures 4.7(a)–4.7(b) show the homogenized refractive index  $n_{\text{NIM}}$  and the relative impedance  $z_{\text{NIM}}$  of a NIM cell for  $A_3$ . The optimized load component values are found to be  $C_{Z1} = C_{Z2} = 0.92$  pF and  $L_Y = 6.17$  nH.

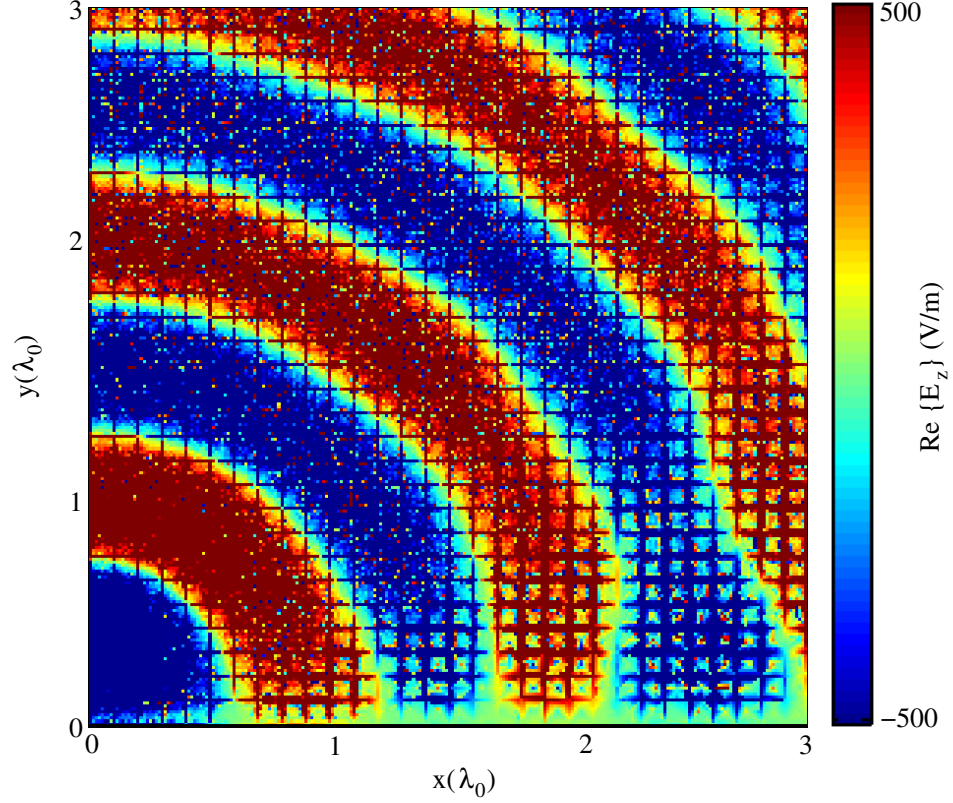


**Figure 4.5.** Snapshot of  $E_z$  for the original configuration of a probe over a flat ground plane.

Following a similar modeling procedure, the unit cell for the anisotropic impedance-matching region is designed to realize the set of medium parameters given in Section 4.1. We obtain two sets of optimized load values with respect to the direction of power flow. Figure 4.8 shows the unit cell of  $A_2^-$  and  $A_2^+$ . For a via diameter of 0.381 mm, Figures 4.9(a)–4.9(b) and 4.10(a)–4.10(b) show the homogenized refractive index  $n$  and the relative impedance  $z$  of the matcher unit cell along  $\hat{q}_1$  and  $\hat{q}_2$  directions, respectively. The optimized set of load values in this case are found to be  $C_{Z1} = 4.60$  pF,  $L_{Z2} = 2.02$  nH,  $L_Y = 80.81$  nH and  $C_{Z1} = 4.60$  pF,  $L_{Z2} = 2.02$  nH,  $L_Y = 24.61$  nH, along  $\hat{q}_1$  and  $\hat{q}_2$  directions, respectively.

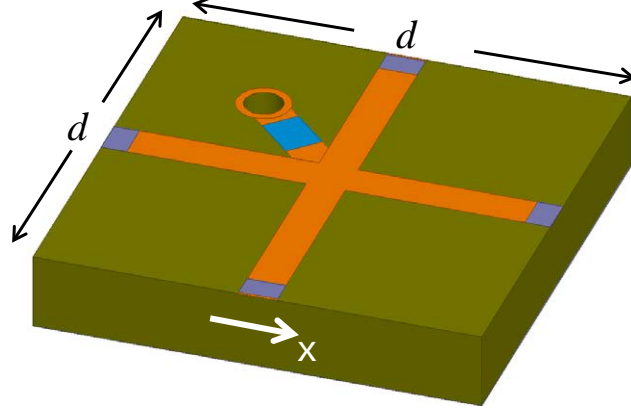


**Figure 4.6.** TL NIM unit cell for parameter retrieval and optimization.

### 4.3 Measurement Results

The designed TL configuration was fabricated over an area of  $500 \text{ mm} \times 360 \text{ mm}$  ( $5.6\lambda_0 \times 4\lambda_0$ ), corresponding to a  $56 \times 40$  microstrip TL grid. The required lumped element values for loads for the fabrication were calculated in Section 4.2. Appropriate surface-mount (SMT) components are chosen among commercially available chip capacitors and chip inductors. Table 4.1 shows the actual load values used for each region in the fabricated design sample. Chip resistors of  $75 \Omega$  terminate the outer boundary of the unloaded microstrip TL grid of region  $A_0$  that represents free space. A total of 702 SMT elements were used. Manufacturer part numbers of the components are listed in Table 4.2. A photo of the fabricated prototype and the associated design schematic of the embedding metamaterial regions are shown in Figures 4.11(a) and 4.11(b), respectively.

The measurement setup is shown in Figure 4.12. The TL grid is excited at  $(x, y) = (0, -0.75\lambda_0)$  with a probe fed by a coaxial cable from below the grounded substrate. The feeding coaxial cable is connected to Port 1 of a vector network analyzer (Agilent model E8363B). The  $\hat{z}$  component of the electric field in a plane above the TL grid surface is detected using a coaxial sensor probe. The sensor probe is connected to Port 2 of the network analyzer. Figure 4.13 shows the  $x - y$  positioner. The positioner was controlled to move the board in  $8.83 \text{ mm}$  ( $\lambda_0/10$ ) steps. The transmission coefficient  $S_{21}$  between the

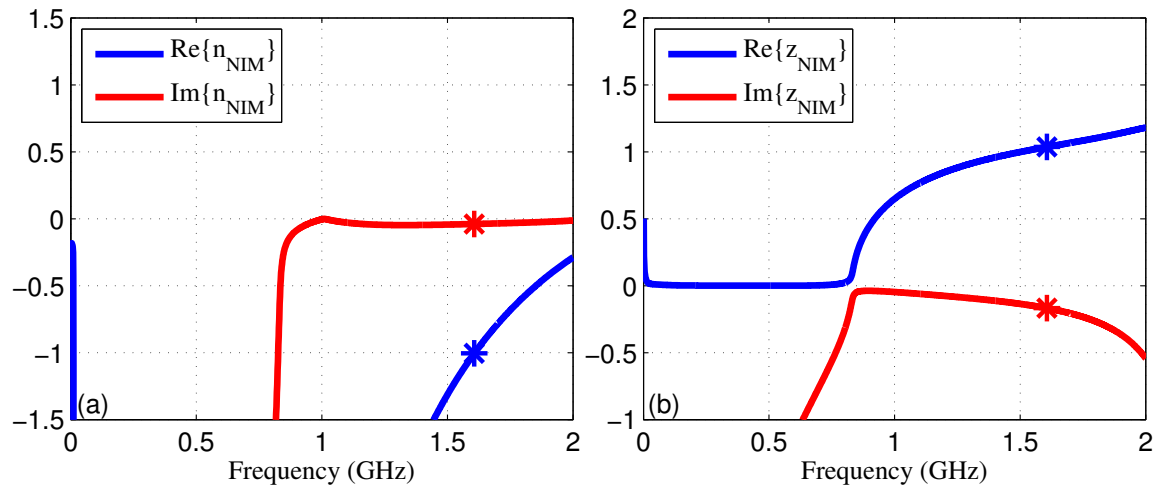


**Figure 4.7.** Homogenized medium parameters of the optimized NIM cell with the real load values. (a) Refractive index  $n_{\text{NIM}}$ . (b) Normalized impedance  $z_{\text{NIM}}$ .

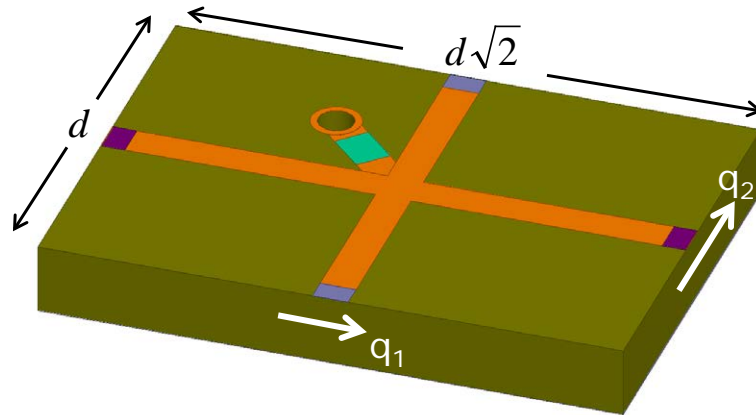


**Figure 4.8.** TL matcher unit cell for parameter retrieval and optimization.



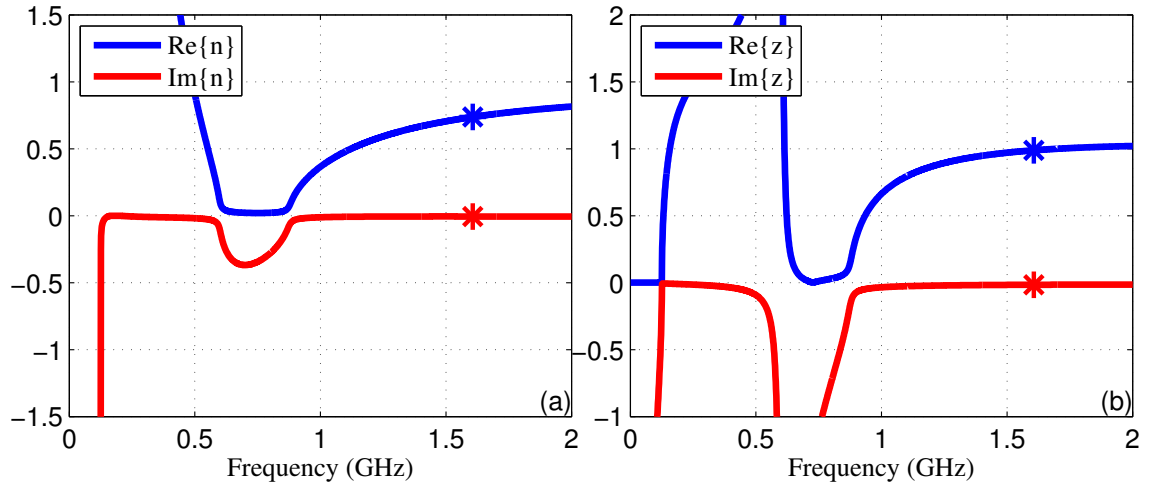


**Figure 4.9.** Homogenized medium parameters of the optimized matcher cell along  $q_1$  with the real load values. (a) Refractive index  $n$ . (b) Normalized impedance  $z$ .

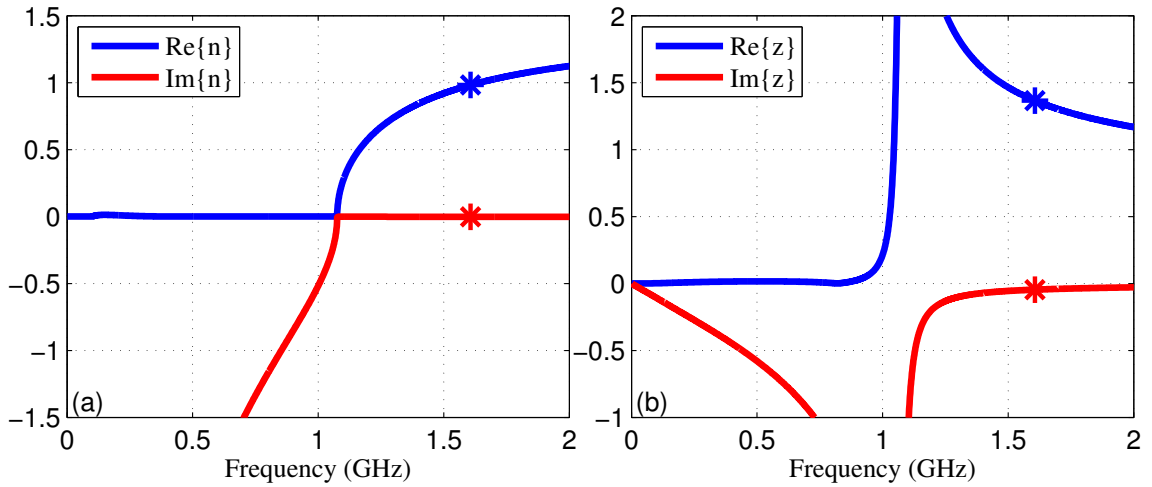


**Figure 4.10.** Homogenized medium parameters of the optimized matcher cell along  $q_2$  with the real load values. (a) Refractive index  $n$ . (b) Normalized impedance  $z$ .



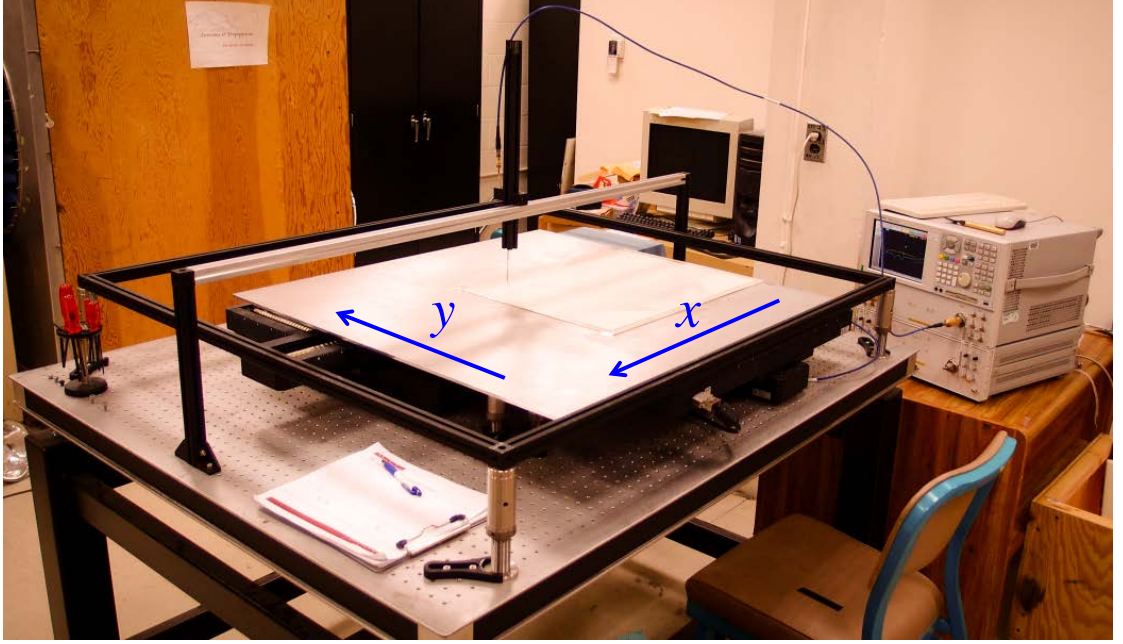


**Figure 4.13.** Measurement setup.  $x - y$  positioner table.

excitation and sensor probes was recorded at each step. LabVIEW by National Instruments is used to command the network analyzer and the positioner.

Electric field maps were generated over a narrow bandwidth around the design frequency  $f_0 = 1.607$  GHz. The best result was observed at  $f = 1.616$  GHz, where the measured phase distribution of the  $S_{21}$  is plotted in Figure 4.14(a). The phase distribution clearly shows that the waves generated by the embedded probe configuration appear as if they originate from above the ground plane as intended. The relatively small deviation of the optimal operating frequency from the design frequency  $f_0$  is primarily attributed to the variation of component values of the SMT capacitors and inductors from their nominal values, in addition to fabrication tolerances. The magnitude distribution of  $S_{21}$  at  $f = 1.616$  GHz is shown in 4.14(b) where the locations of the excitation probe and its image above the ground plane are indicated. As expected, a strong field at the image location inside the NIM lens is observed. In addition, strong fields associated with surface-mode

**Table 4.1.** Host TL configurations, and the loading elements used in the fabrication for each region.

	Host			Loading					
	$p_1$	$p_2$	$\alpha$	$L_{Z1}$	$C_{Z1}$	$L_{Z2}$	$C_{Z2}$	$L_Y$	$C_Y$
$A_0$ $A_1$	$p_0$	$p_0$	0	N/A					
$A_2^-$ $A_2^+$	$p_0\sqrt{2}$	$p_0$	$45^\circ$	—	4.7 pF	2 nH	—	24 nH	—
$A_3$	$p_0$	$p_0$	0	—	0.9 pF	—	0.9 pF	6.2 nH	—

**Table 4.2.** Manufacturer part numbers of the components used in the fabrication.

Description	Manufacturer	Part Number
CAP 4.7 pF 0402	Johanson Technology	500R07S4R7BV4T
IND 2 nH 0402	Abracon Corporation	AISC-0402-2N0J-T
IND 24 nH 0402	Würth Electronics	744765124A
CAP 0.9 pF 0402	Murata Electronics	GRM1555C1HR90WA01D
IND 6.2 nH 0402	Abracon Corporation	AISC-0402-6N2G-T
RES 75 $\Omega$ 0402	Panasonic Electronic	ERJ-2RKF75R0X

plasmon resonances [38] are measured along the free space-NIM lens ( $A_0 - A_3$ ) interface at  $y = 0$ .

Finally, we consider the pattern bandwidth characteristics of the design, in addition to the performance at the design frequency. Figures 4.15(a) and 4.15(b) show the phase distributions at  $f = 1.592$  GHz and  $f = 1.640$  GHz, respectively. A deviation of less than  $p_0 = 0.1\lambda_0$  in the image source location was considered as the performance criterion. The design performance were observed to start deteriorating at approximately  $-1.5\%$  and  $+1.5\%$  away from  $f = 1.616$  GHz.

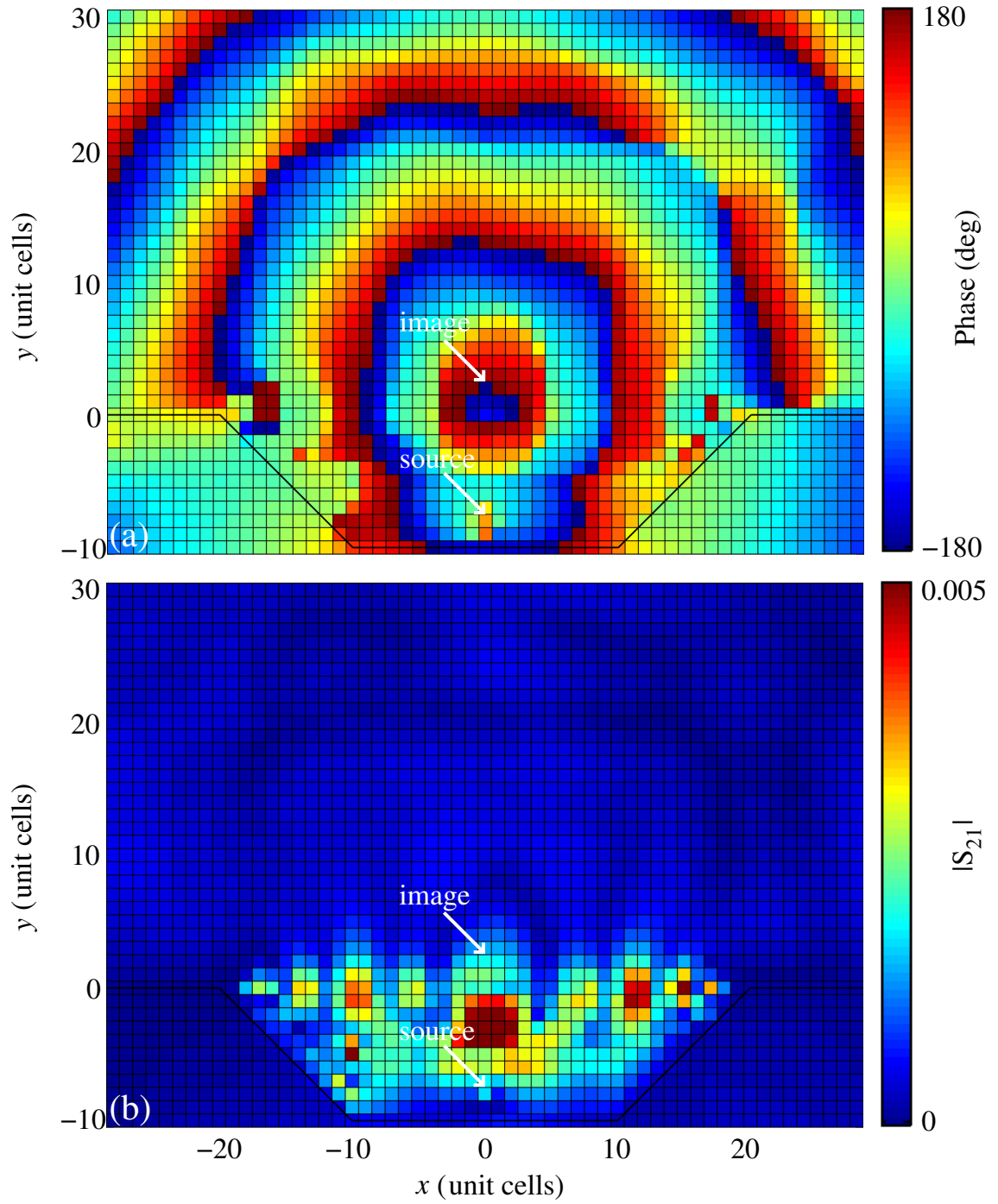


**Figure 4.14.** Measured  $S_{21}$  distributions at  $f = 1.616$  GHz. (a) Phase. (b) Magnitude.

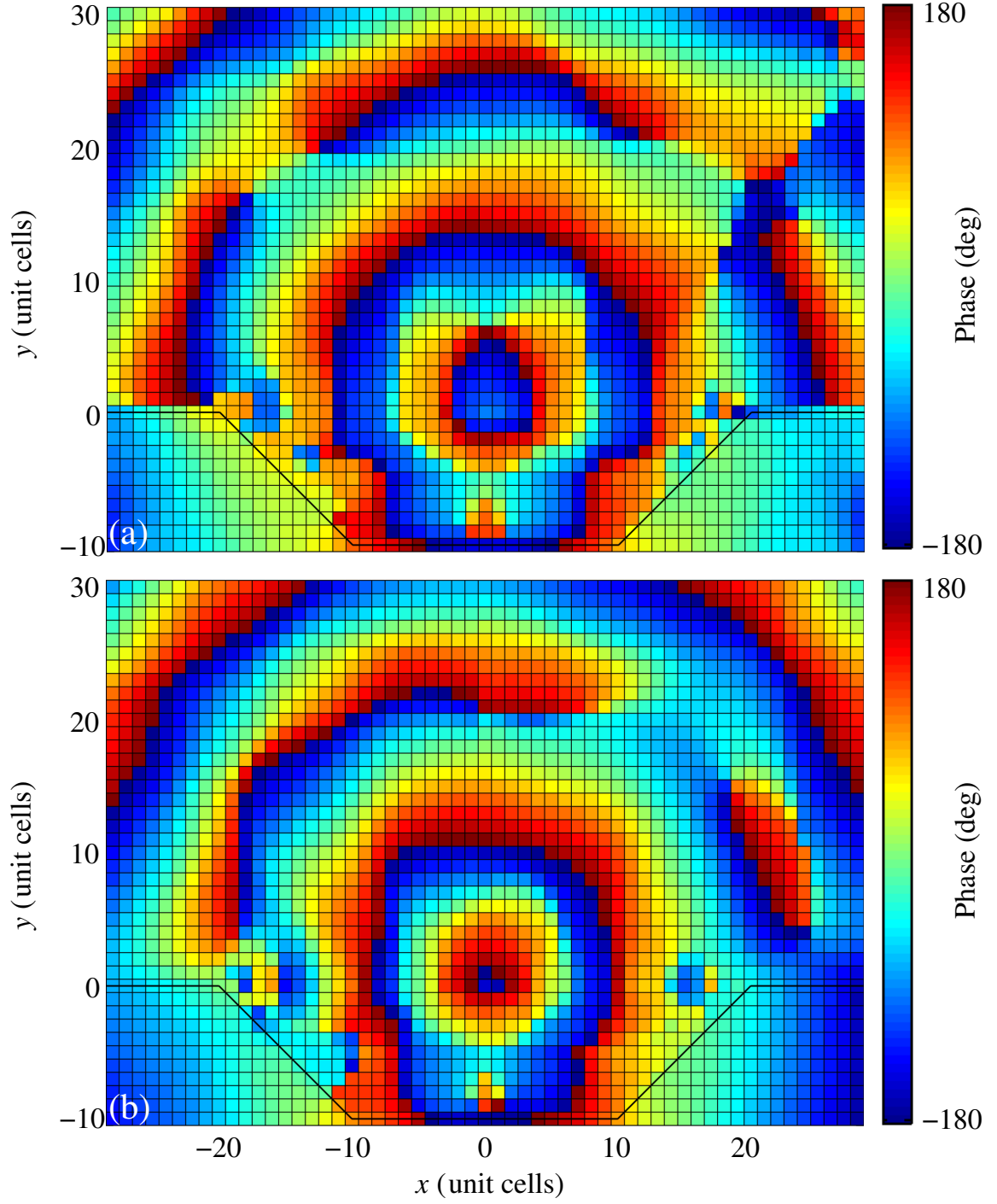


**Figure 4.15.** Measured  $S_{21}$  phase distributions. (a) At  $f = 1.592$  GHz. (b) At  $f = 1.640$  GHz.

## CHAPTER 5

### 2-D METAMATERIAL EMBEDDED LINE SOURCE

A resonator-based metamaterial implementation of the 2-D effective medium designed in Chapter 2 is presented in this chapter. The standard effective medium parameter retrieval technique described in Section 3.1 is used in the extraction of the material parameters at the chosen design frequency  $f_0 = 5$  GHz.

Resonant inclusion-based metamaterials are designed for fabrication using the printed circuit board (PCB) technology. For low-loss properties at high frequencies, Rogers Corporation's RT/Duroid 5880 laminates of a 20 mil thickness with a 0.5-oz. copper cladding (a thickness of 0.017 mm) are chosen for the substrate. Thicker copper traces lead to smaller conductor losses, but a 0.5-oz. thickness was selected due to narrow trace widths and narrow gaps between traces on the order of 0.1 mm or less that are employed in the final designs.

#### 5.1 Unit Cells for the Negative-Index Lens $A_3$

The region  $A_3$  in Figure 2.5(b) represents a NIM superlens that forms the image of the physical source above the ground plane. It has homogeneous and isotropic relative permeability  $\mu$  and permittivity  $\epsilon$  values, both being simultaneously equal to -1 [29].

The NIM unit cell design is illustrated in 5.1. It consists of four substrate segments, each containing SRRs and ELCs on opposite faces. The polarization of the 2-D configuration is TE—the electric field is  $z$ -directed. The SRRs positioned in the two orthogonal planes control the effective permeability in the  $x - y$  plane, and the ELCs having the resonator axis along the  $z$  direction adjust the effective permittivity of the homogenized medium. It

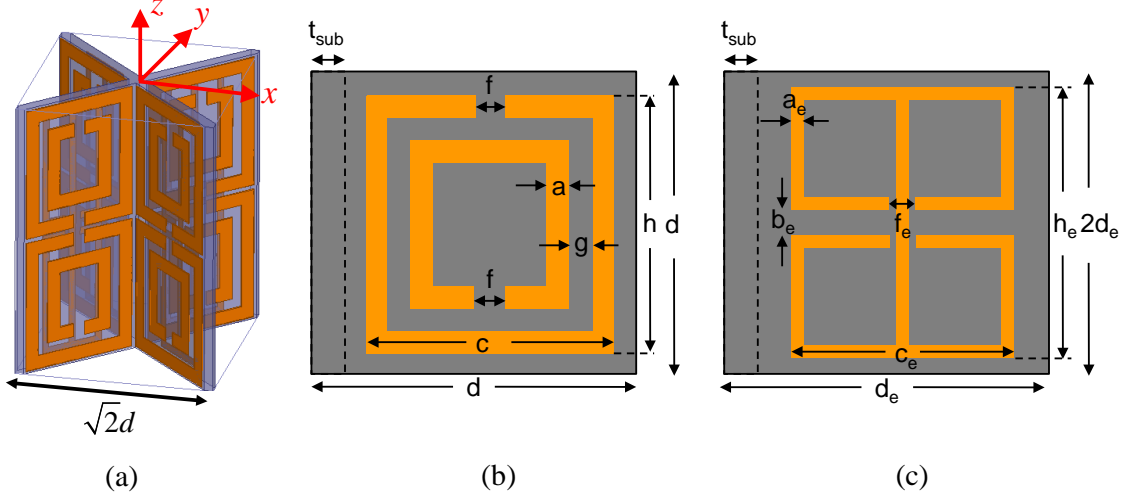


**Figure 5.1.** Unit cell for the NIM superlens metamaterial. (a) 3-D view. (b) SRR wall. (c) ELC wall. The side of the unit cell is equal to  $d\sqrt{2}$ .

is known that the positions of the gaps in the SRR shown in Figure 5.1(a) minimize the bianisotropy coming from magneto-electric coupling within the magnetic resonator [44].

The unit cell size were chosen such that  $d = \lambda_0/10 = 6$  mm at the design frequency  $f_0$ . Efficient numerical analysis can be performed on the unit cell with periodic boundary conditions on the four vertical walls. Using Ansys HFSS, the geometrical parameters of the unit cell were numerically optimized to obtain  $\mu = \epsilon = -1$ . We note that the index of refraction  $n$  and the impedance  $z$  relative to the free space are given by  $n = \sqrt{\mu\epsilon} = -1$  and  $z = \sqrt{\mu/\epsilon} = 1$ . The objective of the numerical optimization was set to minimize the cost function defined by

$$\text{cost} = |n + 1|^2 + |z - 1|^2. \quad (5.1)$$

An optimization setup based on the standard genetic algorithm (GA) was used with  $a$ ,  $c$ ,  $g$ ,  $h$ ,  $a_e$ ,  $b_e$ ,  $c_e$ , and  $h_e$  as the optimization parameters. The best set of parameters with the lowest cost was chosen and used as the initial point for a final optimization based on the quasi-Newton (QN) method. The parameters  $f$ ,  $f_e$ ,  $h$  and  $h_e$  were used for this optimization.



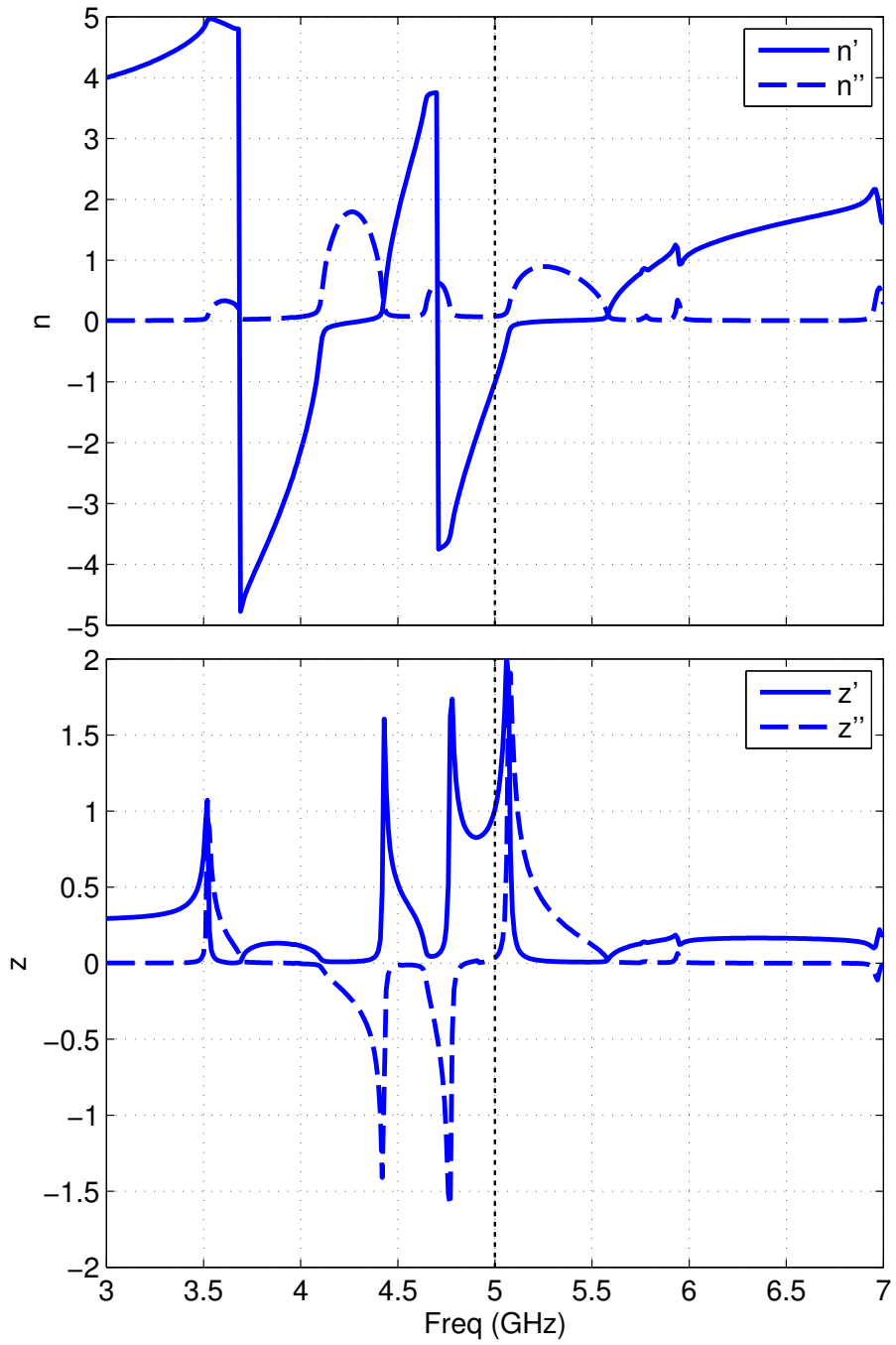


**Figure 5.2.** The retrieved medium parameters of the optimized NIM unit cell for  $A_3$ . Index of refraction  $n = n' - jn''$ , and impedance  $z = z' - jz''$ .

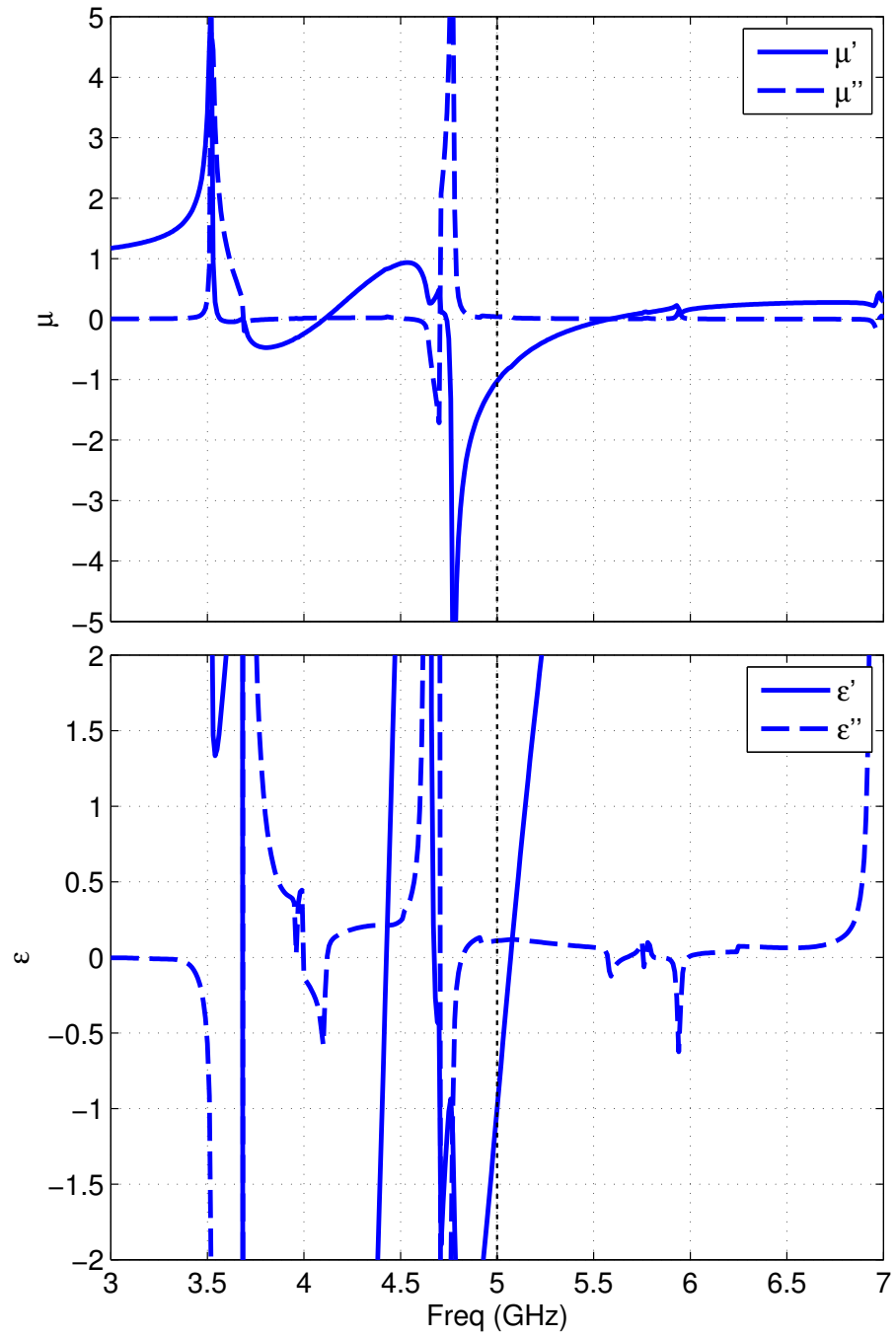


**Figure 5.3.** The retrieved medium parameters of the optimized NIM unit cell for  $A_3$ . The relative permeability  $\mu = \mu' - j\mu''$ , and permittivity  $\epsilon = \epsilon' - j\epsilon''$ .

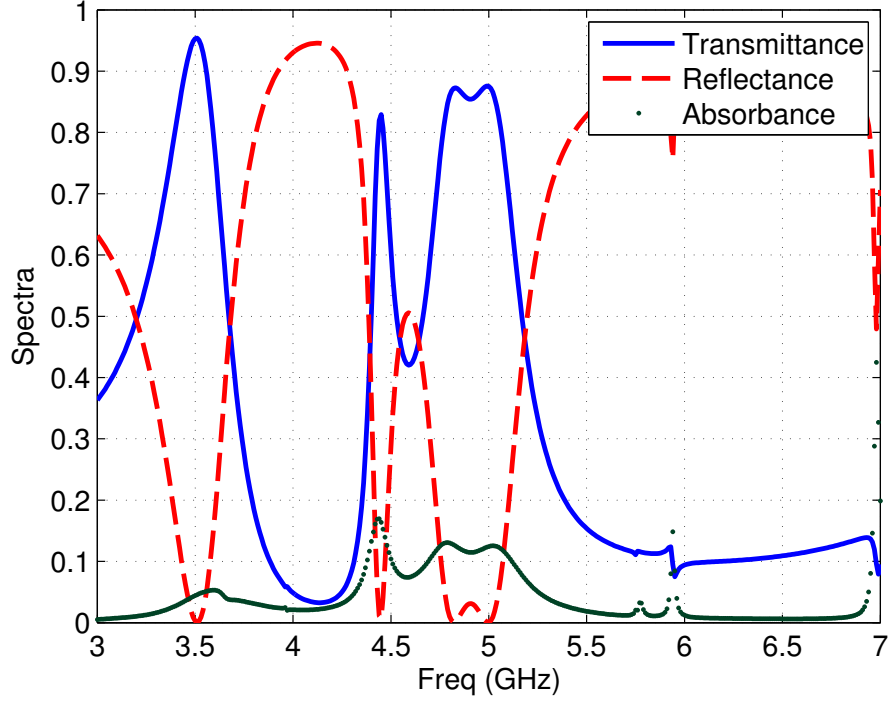


**Figure 5.4.** Retrieved transmittance, reflectance, and absorbance of the optimized NIM unit cell for  $A_3$ .

**Table 5.1.** Geometrical design parameters for the NIM unit cells (in mm).

NIM ( $A_3$ )				Conventional NIM			
ELC		SRR		ELC		SRR	
$a_e$	0.31	$a$	0.59	$a_e$	0.37	$a$	0.61
$b_e$	0.42	$c$	5.2	$b_e$	0.63	$c$	5.2
$c_e$	2.78	$d$	6.0	$c_e$	2.83	$d$	6.0
$f_e$	0.76	$g$	0.39	$f_e$	0.76	$g$	0.44
$d_e$	6.0	$h$	5.8	$d_e$	6.0	$h$	5.8
$h_e$	11.42	$f$	0.55	$h_e$	11.63	$f$	0.56
$t_{sub}$	0.508	$t_{sub}$	0.508	$t_{sub}$	0.254	$t_{sub}$	0.254

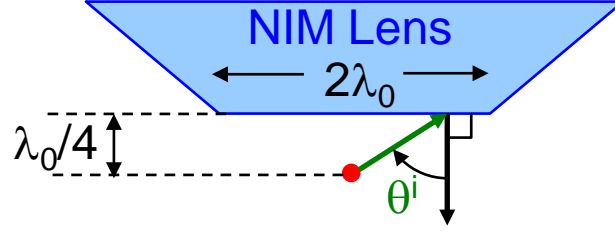


**Figure 5.5.** The NIM lens under line source illumination.

At the design frequency of 5 GHz, the optimized values were found to be  $n = -1.012 - j0.076$  and  $z = 1.011 - j0.035$ . The final design parameters for the optimized cell are given in Table 5.1. For the optimized cell, the retrieved medium parameters are plotted in Figures 5.2 and 5.3 as a function of frequency.

The metamaterial exhibits negative index of refraction in 4.71–5.29 GHz. Slope of  $n'$  in this range suggests a more dispersive response in comparison with a similar NIM design utilizing a wire medium for negative permittivity [19]. The relative permeability and permittivity at the design frequency were obtained to be  $\mu = -1.026 - j0.041$  and  $\epsilon = -0.997 - j0.110$ , respectively.

In Figure 5.4, the transmittance, reflectance, and absorbance spectra of the NIM slab of one-cell thickness are shown with respect to frequency. The slab exhibits 87.51% transmission, 12.42% absorption, and 0.07% reflection at the design frequency. The absorption is observed to be associated with the electric resonance at 4.77 GHz.

It is noted that the medium parameters in Figures 5.2–5.4 are specific to the angle of incidence, which is normal to the unit cell boundary. Typically, retrieved medium parameters vary as a function of the incidence angle. Figure 5.5 shows the NIM lens region of the virtual line source application design under consideration. The lens experiences a wide range of incidence angle  $\theta_i$  over  $0 - 76^\circ$ . Therefore, it is desired that both  $n$  and  $z$  stay unchanged from their ideal values for different angle of incidence.

Conventional resonant inclusion-based NIM designs in the microwave frequency range that employs SRRs and wire medium have the NIM-free space boundary coincide with a

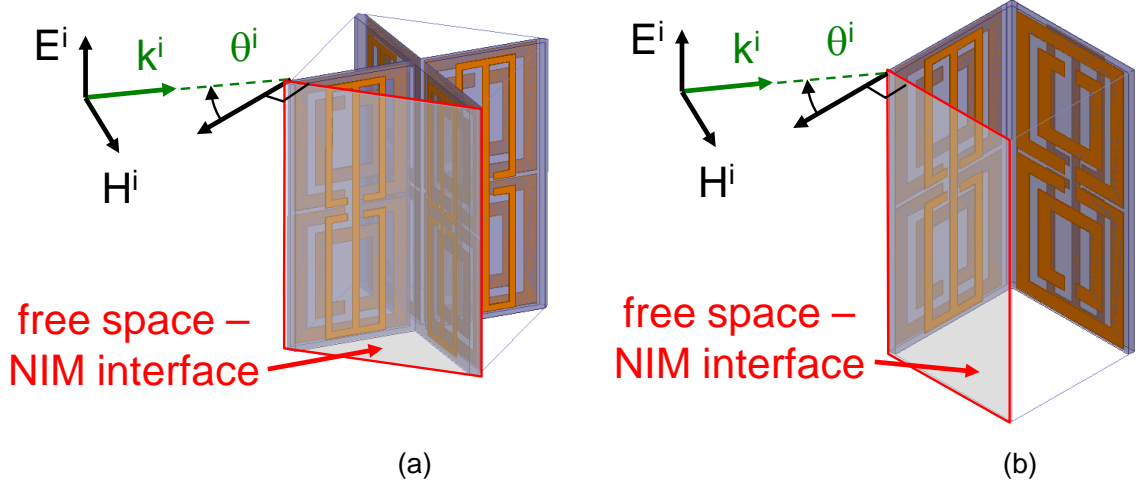


**Figure 5.6.** Unit cells for the NIM lens under TE-polarized plane wave illuminations. (a) Rotated NIM cell. (b) Conventional NIM cell.

wall containing SRRs and/or the wire [51]. Such a NIM unit cell can also be designed based on SRRs and ELCs. In contrast, a  $45^\circ$ -rotated cell was chosen to be designed in this study. We now consider the effect of incidence angle variation on the medium parameters by comparing the rotated and conventional NIM unit cells. The design parameters for the conventional NIM cell are given in Table 5.1. Figure 5.6(a) and 5.6(b) show the rotated and conventional NIM cells, respectively.

The effective medium parameters were computed as a function of the incidence angle and plotted in Figure 5.7(a)–5.7(b). For the NIM design with rotated unit cell, it is found that  $n$  is only a slowly varying function of the incidence angle around 1. The impedance  $z$  turns out to depend even less on the angle than  $n$ . Comparing the angular dependence of the retrieved medium parameters of a conventional NIM design and those of the new design in Figure 5.1(a), it is found that  $n$  and  $z$  of the proposed design are significantly more stable functions. This property is desirable not only in the antenna application under consideration, but also in other applications including sub-diffraction limited lensing applications.

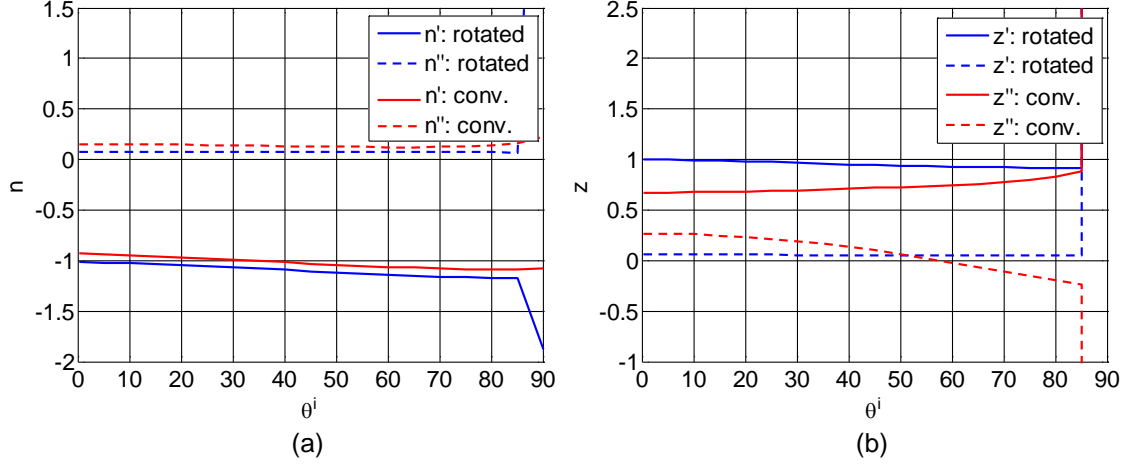


**Figure 5.7.** The effective medium parameters of the NIM lenses as a function of the incidence angle  $\theta_i$ . (a) Index of refraction  $n = n' - jn''$ . (b) Impedance  $z = z' - jz''$ .

## 5.2 Unit Cell for the Matcher $A_2$

Regions  $A_2^-$  and  $A_2^+$  in Figure 2.5(b) have a permeability tensor  $\boldsymbol{\mu}$  in the  $x - y$  plane with non-zero off-diagonal terms as indicated in Equation (2.11). The permittivity  $\epsilon_{zz}$  is equal to 1. The permeability tensor can be diagonalized as

$$\boldsymbol{\mu} = \begin{bmatrix} 1 & 1 \\ 1 & 2 \end{bmatrix} = \mathbf{V} \begin{bmatrix} \mu_{11} & 0 \\ 0 & \mu_{22} \end{bmatrix} \mathbf{V}^T \quad (5.2)$$

where

$$\mathbf{V} = \begin{bmatrix} v_1 & v_2 \end{bmatrix} = \begin{bmatrix} 0.5257 & -0.8507 \\ 0.8507 & 0.5257 \end{bmatrix}. \quad (5.3)$$

The column vectors  $v_1$  and  $v_2$  are the eigenvectors of the matrix. The associated eigenvalues  $\mu_{11}$  and  $\mu_{22}$  are equal to 2.618 and 0.382, respectively. The two eigenvectors are orthogonal. This implies that the permeability tensor is a diagonal matrix when it is expressed in the  $(v_1, v_2, v_3)$  coordinate system, which is equal to the  $(x, y, z)$  coordinate system rotated around the  $z$  axis by  $58.3^\circ$  with  $v_3 = z$ . This approach to synthesizing anisotropic medium

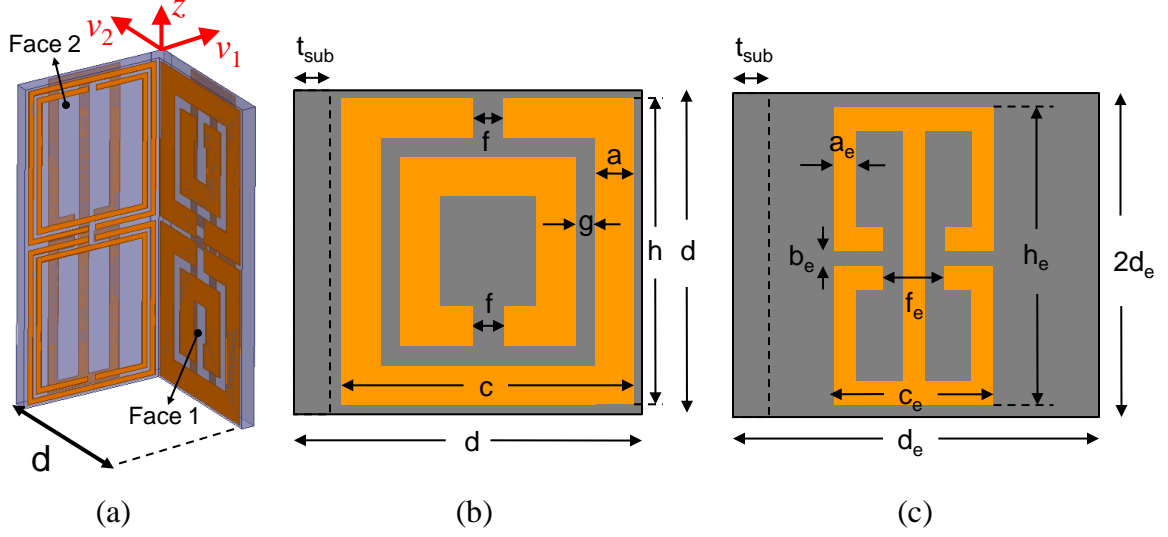


**Figure 5.8.** Unit cell for the anisotropic impedance-matching block  $A_2$ . (a) 3-D view. (b) The SRR face. (c) The ELC face.

parameters has been proposed in [37]. The eigenvectors  $v_1$  and  $v_2$  are associated with their eigendirections.

Therefore, a metamaterial unit cell for the anisotropic parameters (2.11) can be designed following a similar approach to the method used for designing isotropic medium parameters or an anisotropic medium with zero off-diagonal terms for the medium parameter tensor. The unit cell design is shown in Figure 5.8. The two orthogonal walls of a unit cell should incorporate different pairs of electric and magnetic resonators. The resonators are then optimized to synthesize the permeabilities of  $\mu_{11}$  and  $\mu_{22}$ , respectively. Once the resonator designs are complete, the unit cell axis will be rotated such that the face normals are directed along the eigenvectors,  $v_1$  and  $v_2$ . The rotation of the unit cell in the  $x - y$  plane does not affect the value of the permittivity in the  $z$  direction,  $\epsilon_{zz}$ .

As illustrated in Figure 5.8, a pair of SRR and ELC resonators are formed on face 1. A separate pair of resonators of different dimensions are incorporated into face 2. The resonators on face 1 contribute primarily to determining  $\mu_{11}$  and  $\epsilon_{zz}$ . Similarly, the resonators on face 2 are the main contributors to  $\mu_{22}$  and  $\epsilon_{zz}$ . However, it is recognized that the four resonators should be concurrently optimized due to mutual coupling. Since the required

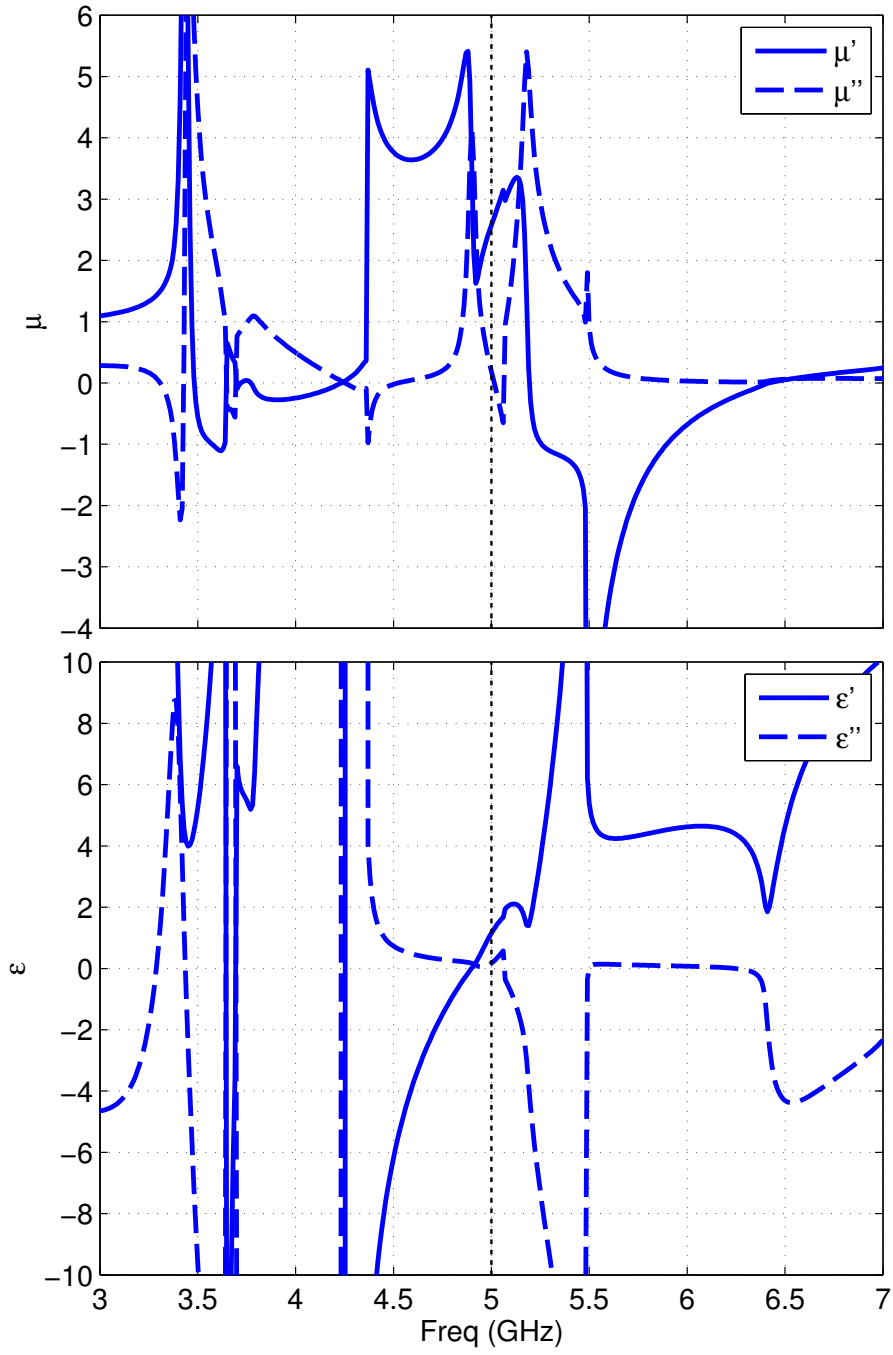


**Figure 5.9.** Retrieved  $\mu_{11}$  and  $\epsilon_{zz}$  of the optimized metamaterial unit cell for  $A_2$ .



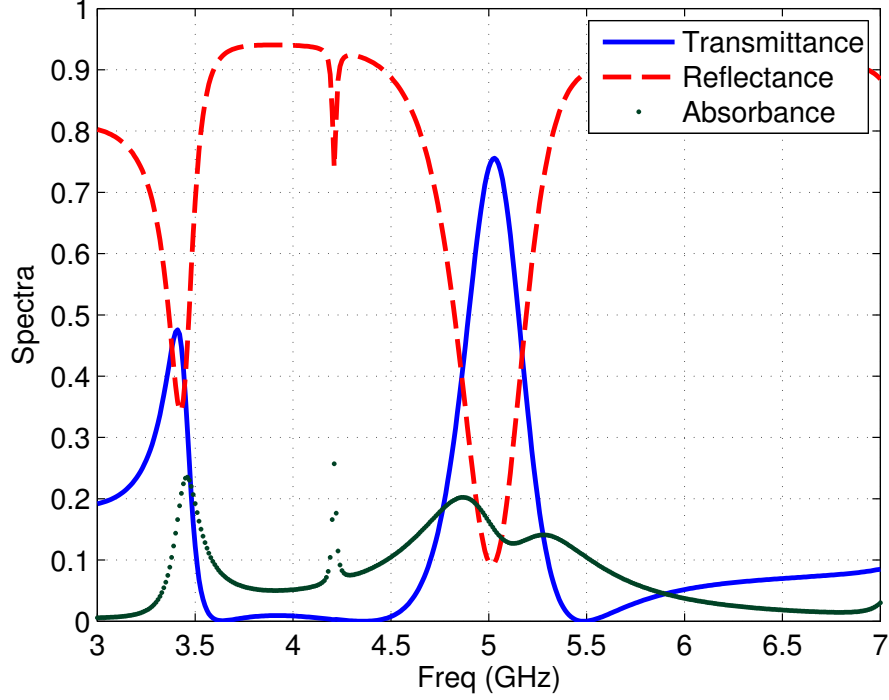


**Figure 5.10.** Transmittance, reflectance, and absorbance of the optimized metamaterial unit cell for  $A_2$  along  $v_2$ .

permittivity  $\epsilon_{zz}$  is equal to 1 isotropically, the same ELC structure with identical dimensions was chosen on both faces of the unit cell. Hence, one ELC and two SRR structures were optimized to give the desired set of values for  $\mu_{11}$ ,  $\mu_{22}$  and  $\epsilon_{zz}$  at the design frequency 5GHz.

The geometrical parameters of the unit cell were numerically optimized under plane wave illuminations in the  $v_1$  and  $v_2$  directions. Two optimizations were performed concurrently with the cost functions defined by

$$\text{cost} = |\mu - 2.618|^2 + |\epsilon - 1|^2, \quad \text{along } v_2 \quad (5.4)$$

$$\text{cost} = |\mu - 0.382|^2 + |\epsilon - 1|^2, \quad \text{along } v_1. \quad (5.5)$$

The same SRR parameter values for  $c$  and  $h$  were adopted from the NIM design of Section 5.1. From the remaining parameters,  $a$ ,  $g$ ,  $a_e$  and  $c_e$  were included in the initial GA-

**Table 5.2.** Geometrical design parameters for the unit cell (in mm).

Matcher ( $A_2$ )					
ELC		SRR- $v_1$		SRR- $v_2$	
$a_e$	0.4	$a$	0.9	$a$	0.2
$b_e$	0.42	$c$	5.2	$c$	5.2
$c_e$	2.9	$d$	6.0	$d$	6.0
$f_e$	0.8	$g$	0.4	$g$	0.14
$d_e$	6.0	$h$	5.8	$h$	5.8
$h_e$	11.82	$f$	0.5	$f$	0.3
$t_{sub}$	0.508	$t_{sub}$	0.508	$t_{sub}$	0.508

based optimization. Then, a QN-based optimization was performed on  $f$  and  $h_e$ . Due to standard PCB process tolerances, the lower bound for all trace widths and gaps between traces was set to 3 mils. The final geometrical parameter values of the optimized unit cell are listed in Table 5.2.

For the optimized unit cell, retrieved parameters  $\mu_{11}$  and  $\epsilon_{zz}$  are plotted with respect to frequency in Figure 5.9. Compared with the desired set of values  $\mu_{11} = 2.618$  and  $\epsilon_{zz} = 1$  at 5 GHz, the unit cell achieves  $\mu_{11} = 2.574 - j0.190$  and  $\epsilon_{zz} = 1.152 - j0.173$ . In particular, it is noted that  $\mu_{11}$  is a highly dispersive function of frequency.

The results in Figures 5.9 and 5.10 were obtained using an incident plane wave with the magnetic field polarized in the  $v_1$  direction. Analysis of the unit cell response for an incident field with the magnetic field polarized in the  $v_2$  direction gives  $\mu_{22}$  and  $\epsilon_{zz}$ . Retrieved parameters are plotted in Figures 5.11 and 5.12. At 5 GHz, the desired set of values are  $\mu_{22} = 0.382$  and  $\epsilon_{zz} = 1$ . The metamaterial exhibits  $\mu_{22} = 0.387 - j0.102$  and  $\epsilon_{zz} = 1.015 + j0.048$ . It is noted that the homogenized values of  $\epsilon_{zz}$  from the two plane wave transmission and reflection analyses are close to each other although they are not the same.

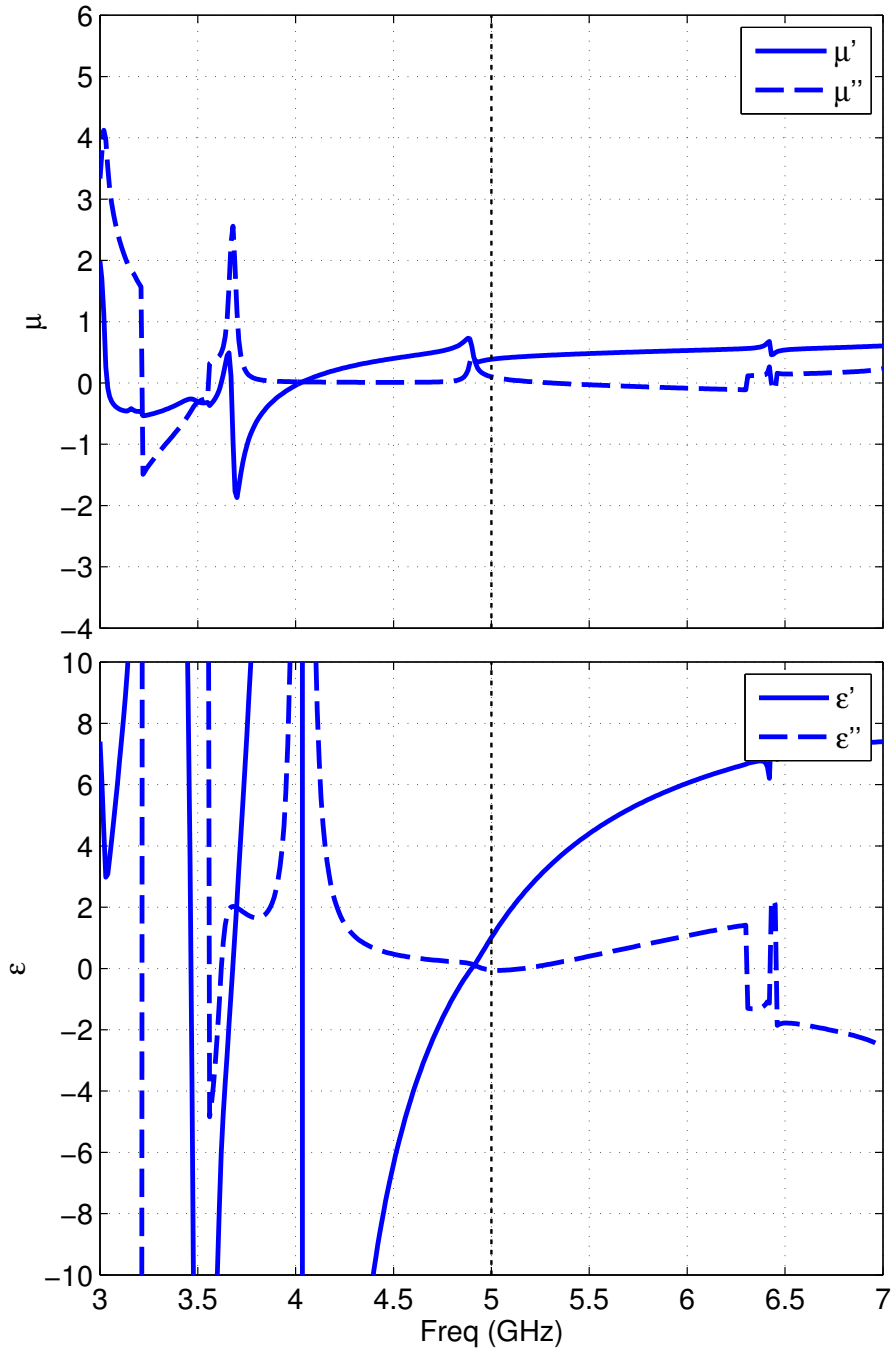


**Figure 5.11.** Retrieved  $\mu_{22}$  and  $\epsilon_{zz}$  of the optimized metamaterial unit cell for  $A_2$ .

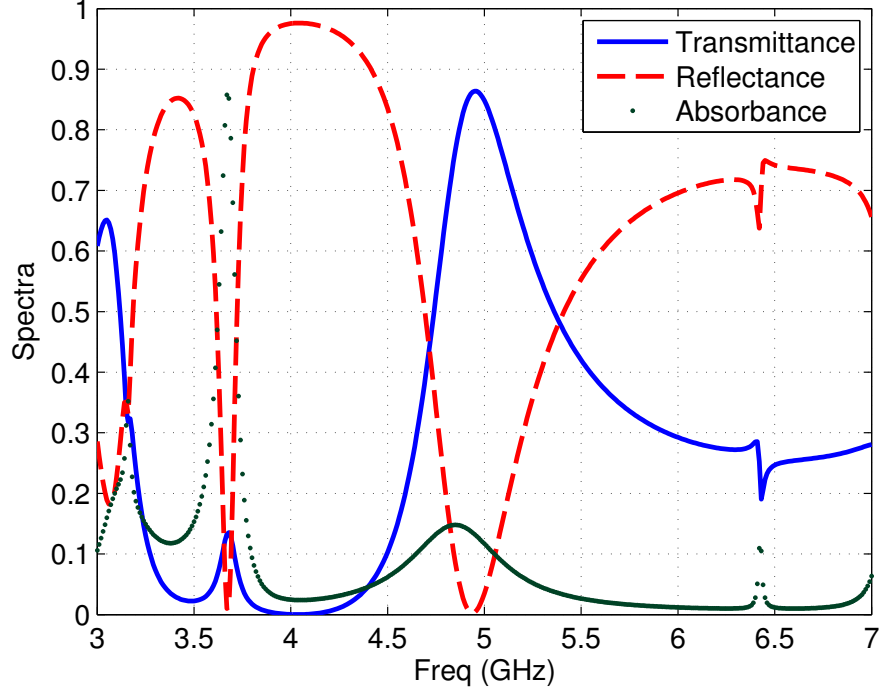


**Figure 5.12.** Transmittance, reflectance, and absorbance of the optimized metamaterial unit cell for  $A_2$  along  $v_1$ .

### 5.3 Measurement Results

The optimized metamaterial walls were fabricated using the standard PCB technologies, and unit cells were assembled for each metamaterial region as shown in Figure 5.13. The height of the fabricated 2-D configuration is four unit cells-thick ( $0.4\lambda_0$ ). Figure 5.14(a) shows the assembled metamaterial placed in a ground recess. The recess was realized using a bent aluminum strip. Copper tapes were used along the strip to ensure the proper contact between top and bottom plates of the waveguide simulator as shown in Figure 5.14(b). Edges of the truncated aluminum strip were treated with tapered copper taping. Measurement volume in  $y > 0$  was terminated in absorbers to keep waves from reaching the edges and corners of the plates. Figure 5.15(a) and 5.15(b) show the metamaterial setup for the original and the embedded line source configurations, respectively. A flat aluminum strip was used as the ground plane for the original configuration.

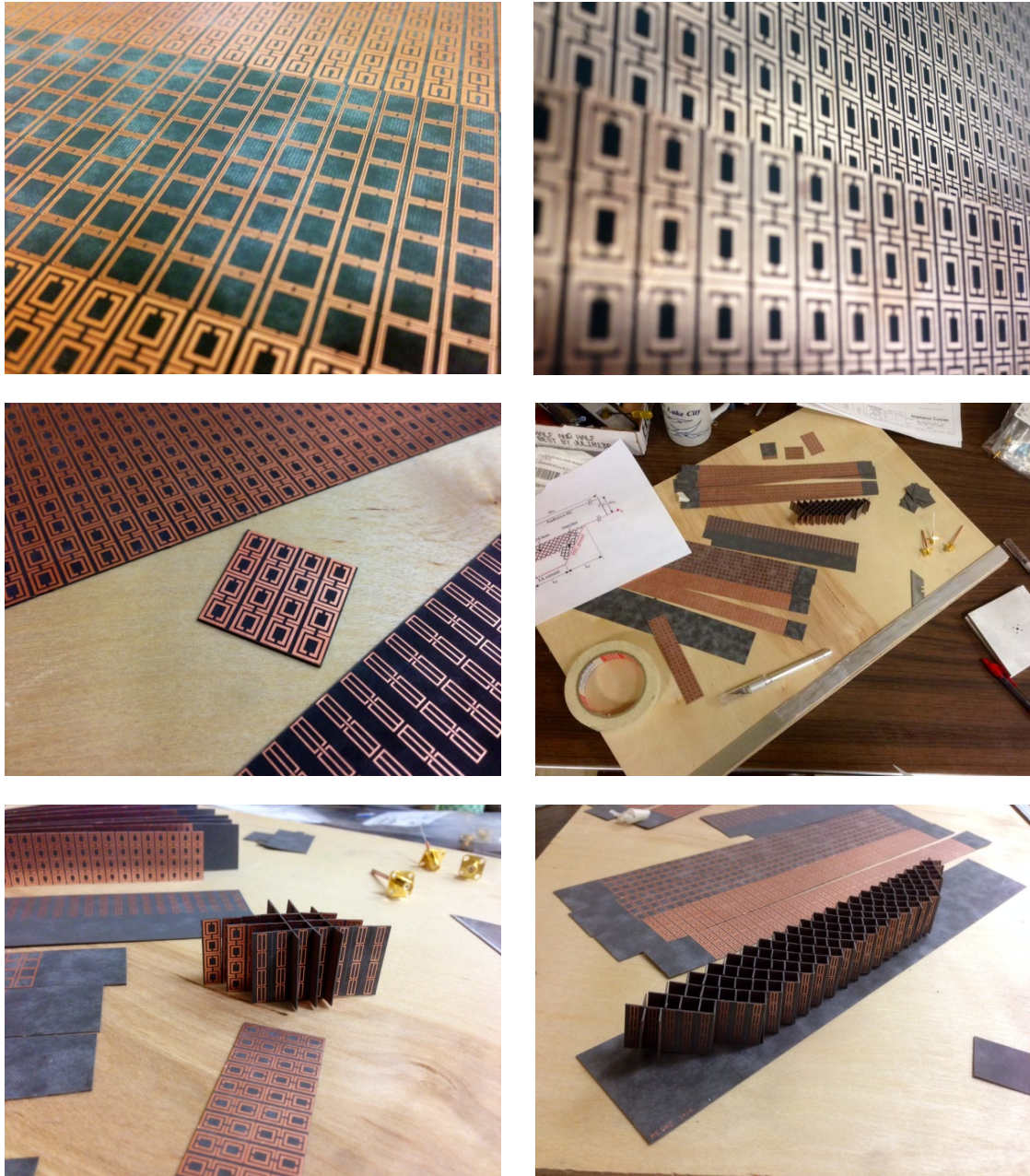


**Figure 5.13.** Assembly steps for the NIM lens and the matcher metamaterial.



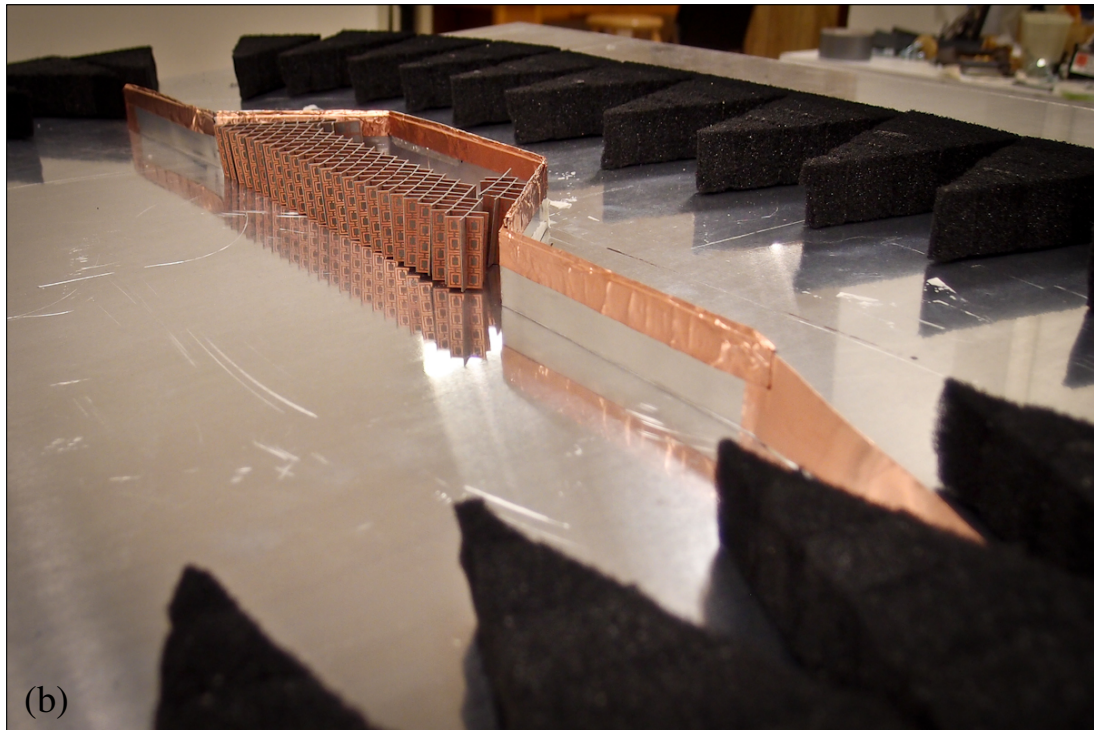
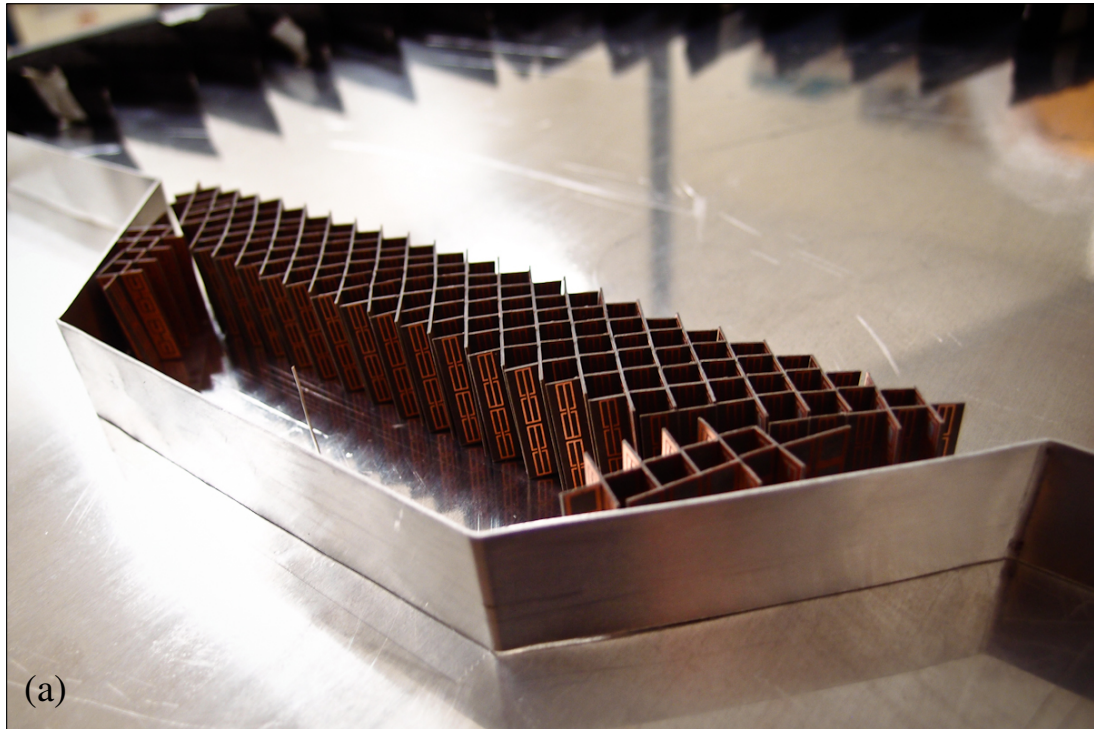


**Figure 5.14.** Assembled metamaterial inside the ground recess. (a) A bent aluminum strip was used as the ground recess. (b) The ground recess was treated with copper tape. The measurement volume was terminated in absorbers.

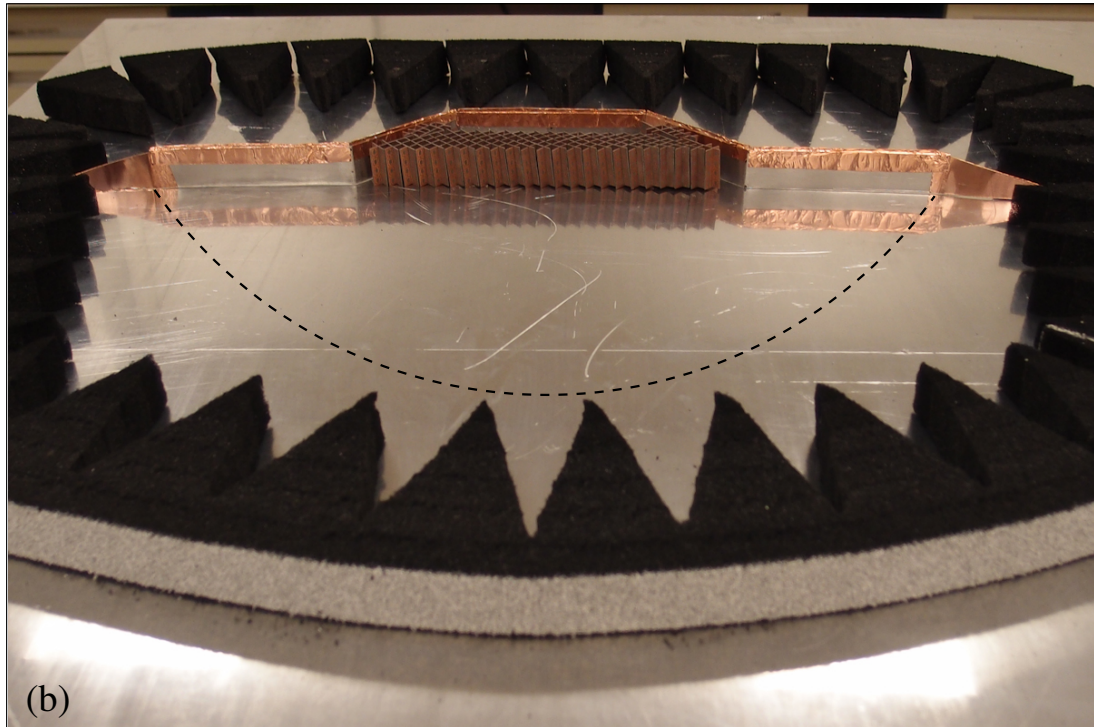
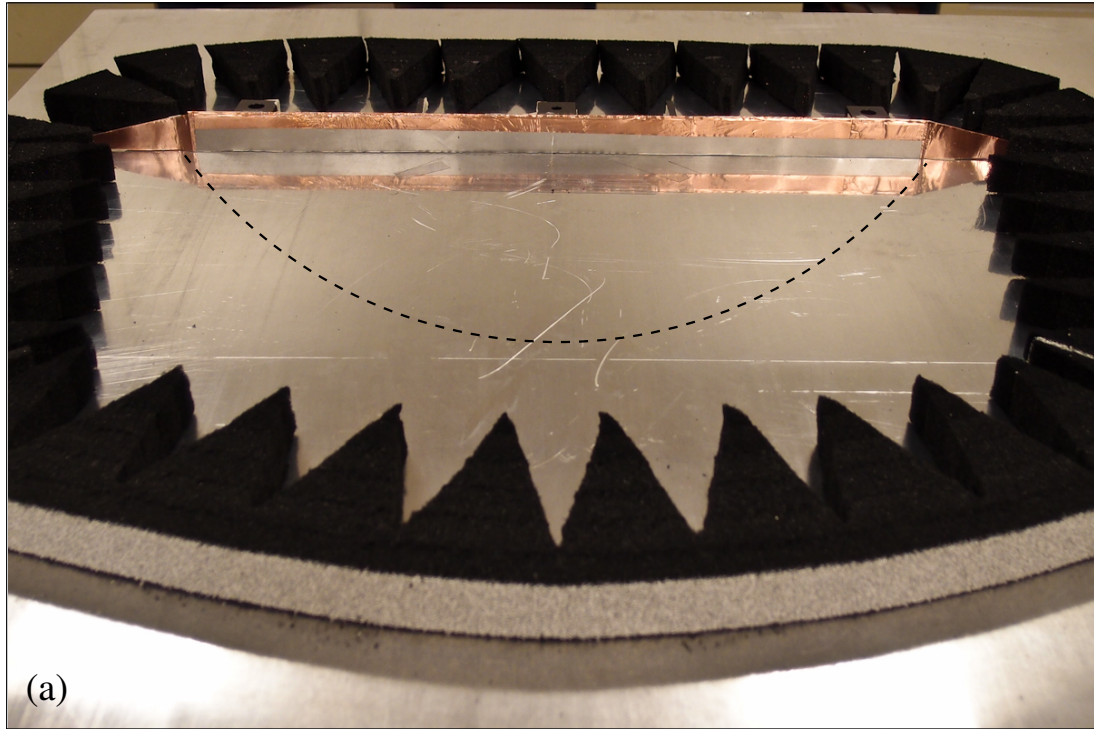


**Figure 5.15.** Metamaterial set up for field-scanning measurement. (a) Original configuration. (b) Embedded configuration.



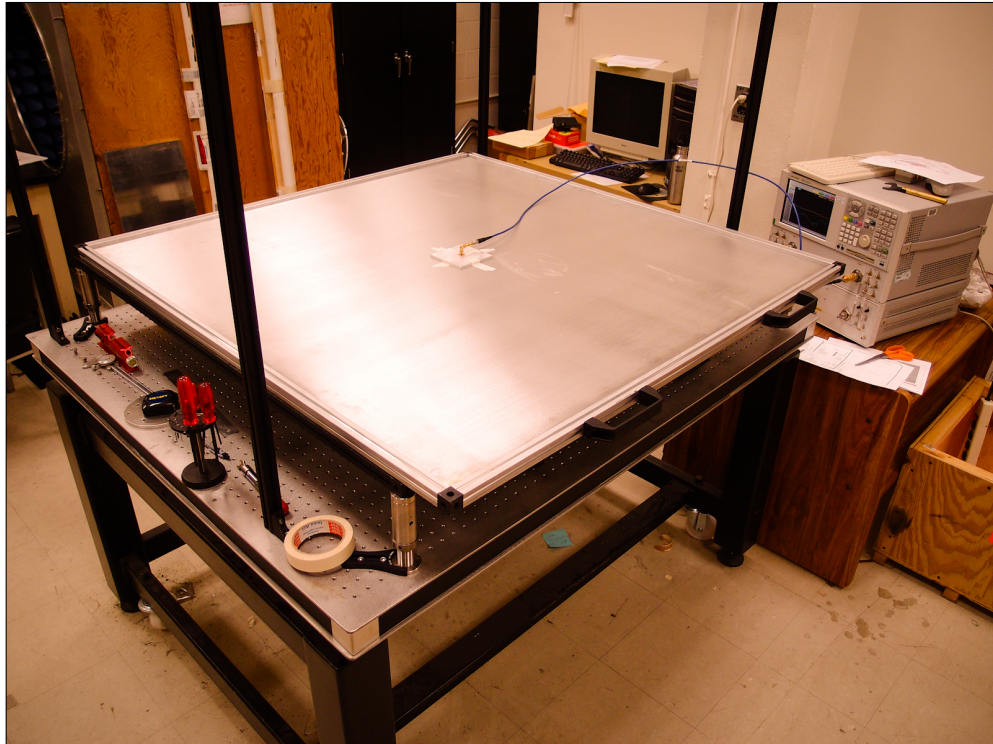
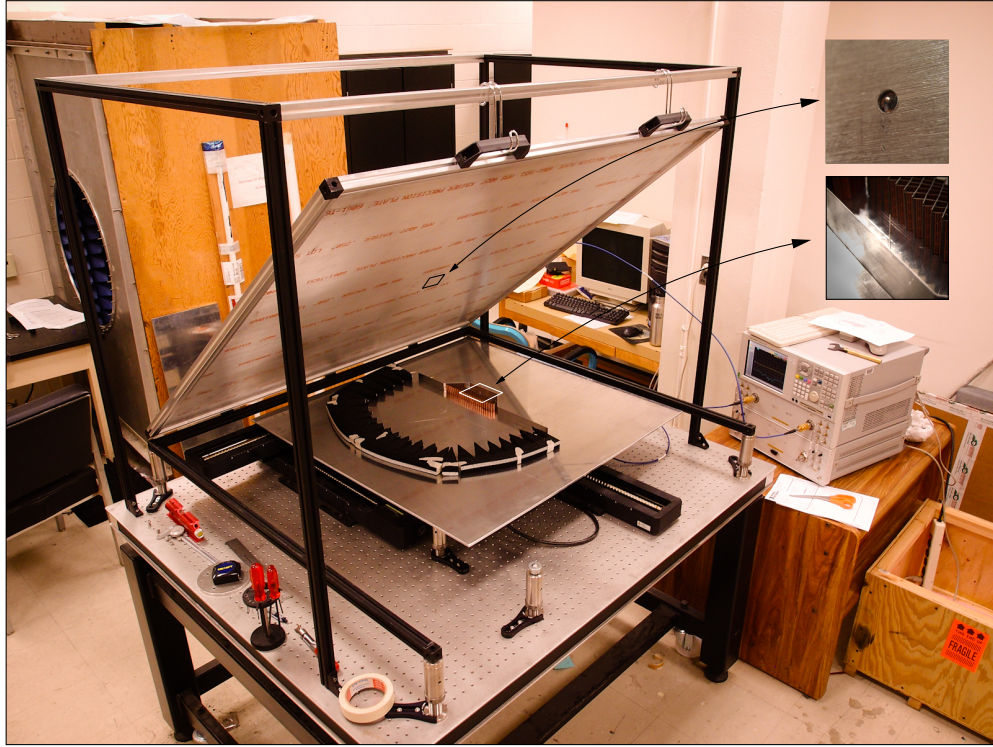


**Figure 5.16.** Parallel-plate waveguide simulator setup on the  $x - y$  positioner table. Insets show close-up photos of the cut coaxial cable used as an  $E$ -field sensor in the top plate, and the  $0.4\lambda_0$ -long excitation probe.



Figure 5.16 shows a parallel-plate waveguide simulator setup to measure the E-field distribution over an area of  $6\lambda_0 \times 4\lambda_0$  using an E-field sensor (a cut coaxial cable in the top plate). A  $0.4\lambda_0$ -long probe is used for excitation, and fed by a coaxial cable from below the bottom plate. The  $x - y$  positioner was controlled to move the bottom plate in 5 mm ( $\lambda_0/12$ ) steps. The transmission coefficient  $S_{21}$  between the excitation and sensor probes was recorded at each step.

Measured  $S_{21}$  distributions are shown in Figures 5.17–5.19. Figure 5.17 shows the phase distributions around the design frequency  $f_0$ . The best result with respect to the phase center restoration was measured at  $f = 4.92$  GHz. The phase distribution in Figure 5.17(a) shows that the waves generated by the embedded line source appear as if they originate above the ground plane. The relatively small deviation of the frequency of optimal performance from the design frequency  $f_0$  is attributed to the fabrication tolerances and deviations from the ideal structure in the assembly process.

For comparison, characteristics of the recessed probe radiation in an empty recess without the embedding metamaterials are shown in Figure 5.20. It is observed that both phase and magnitude distributions of the measured  $S_{21}$  are significantly distorted.

For quantitative evaluation of the virtual line-source radiation, measured near-field patterns are analyzed. Measured  $S_{21}$  distributions can be sampled along a semicircular arc of largest radius allowed in the measurement setup. These arcs are shown as dashed contours in Figure 5.15. We introduce the normalized near-field pattern from

$$F_{\text{near}}(\phi) = 2\pi \frac{U(\phi)}{\int_0^\pi U(\phi) d\phi}, \quad (5.6)$$

where  $U = |S_{21}|^2$ . Dividing  $U$  by the input mismatch factor  $1 - |S_{11}|^2$ , and assuming no loss for the original configuration, we perform calibration by associating the measured value of  $F_{\text{near}}$  with the known directivity of the original configuration. Figure 5.21 shows the measured  $S_{21}$  magnitudes along  $x = 0$ . Magnitude values at  $y = 2\lambda_0$  for the original

and the embedded configurations, and  $y = \lambda_0$  for the empty recess case were chosen for calibration.

The normalized near-field patterns for the embedded configuration are compared in Figure 5.22 around the design frequency. As expected from the phase distributions shown in Figure 5.17(a), the best operating frequency is observed to be  $f = 4.92$  GHz. Overall, the design frequency appears to be shifted to a slightly lower frequency range. Measured near-field patterns are shown in Figure 5.23 together with the simulated patterns plotted in Figure 5.24 of the original, embedded, and empty recess configurations at  $f = 4.92$  GHz. Except for the relatively reduced radiation efficiency for the embedded configuration, measured near-field patterns are in agreement with the simulations. The impact of region  $A_2$  is investigated in Figure 5.25. The impedance matching block  $A_2$  guides the field along the slanted recess wall and it is responsible for restoring the radiation pattern at large angles from broadside. The impact of  $A_2$  on the field distribution near broadside remains minimal, as expected.

In an attempt to extract the approximate far-field radiation patterns from Figure 5.23, a near-field to far-field transformation method is utilized. Interpreting the measured  $S_{21}$  as a scaled value of the  $z$ -directed electric field intensity  $\mathbf{E}$  over the measurement circle centered at the origin, the surface magnetic current density  $\mathbf{M}_s$  is given by

$$\mathbf{M}_s = \mathbf{E} \times \hat{\rho} = \hat{\phi} S_{21} \quad (5.7)$$

At far-zone distances, the electric field due to  $\mathbf{M}_s$  can be written as [12]

$$\mathbf{E}^M = \hat{z} j k \frac{e^{-jk\rho}}{\sqrt{j k 8 \pi \rho}} \int_0^\pi S_{21} e^{jk\hat{\rho} \cdot \rho'} \rho d\phi' \quad (5.8)$$

where  $k$  is the free space wavenumber. We approximate the gain patterns using the far-field expression in (5.8). Approximated gain patterns from the measurements of the original, embedded, and the empty recess configurations at  $f = 4.92$  GHz are shown in Figure 5.26

together with the simulated far-field gain patterns plotted in Figure 5.27. The effect of region  $A_2$  is clearly visible in Figure 5.28, where removal of  $A_2$  results in a reduction in the approximate gain, most notably over  $60^\circ - 80^\circ$  off broadside.

Finally, the exact far-field patterns are calculated utilizing the surface equivalence principle. We consider a PEC boundary condition over the measurement circle centered at the origin. The  $z$ -directed electric field intensity  $\mathbf{E}$  interpreted from the measured  $S_{21}$  can be placed on this PEC boundary as an impressed electric field distribution. Following this approach, far-field gain patterns are numerically calculated using COMSOL Multiphysics. Calculated far-field gain patterns from the measurements of the original, embedded, and the empty recess configurations at  $f = 4.92$  GHz are plotted in Figure 5.29. Using the far-field directivity and gain patterns, the radiation efficiency of the 2-D embedded line source configuration is estimated to be 38.2%. For comparison, simulated far-field gain patterns are plotted in Figure 5.30.

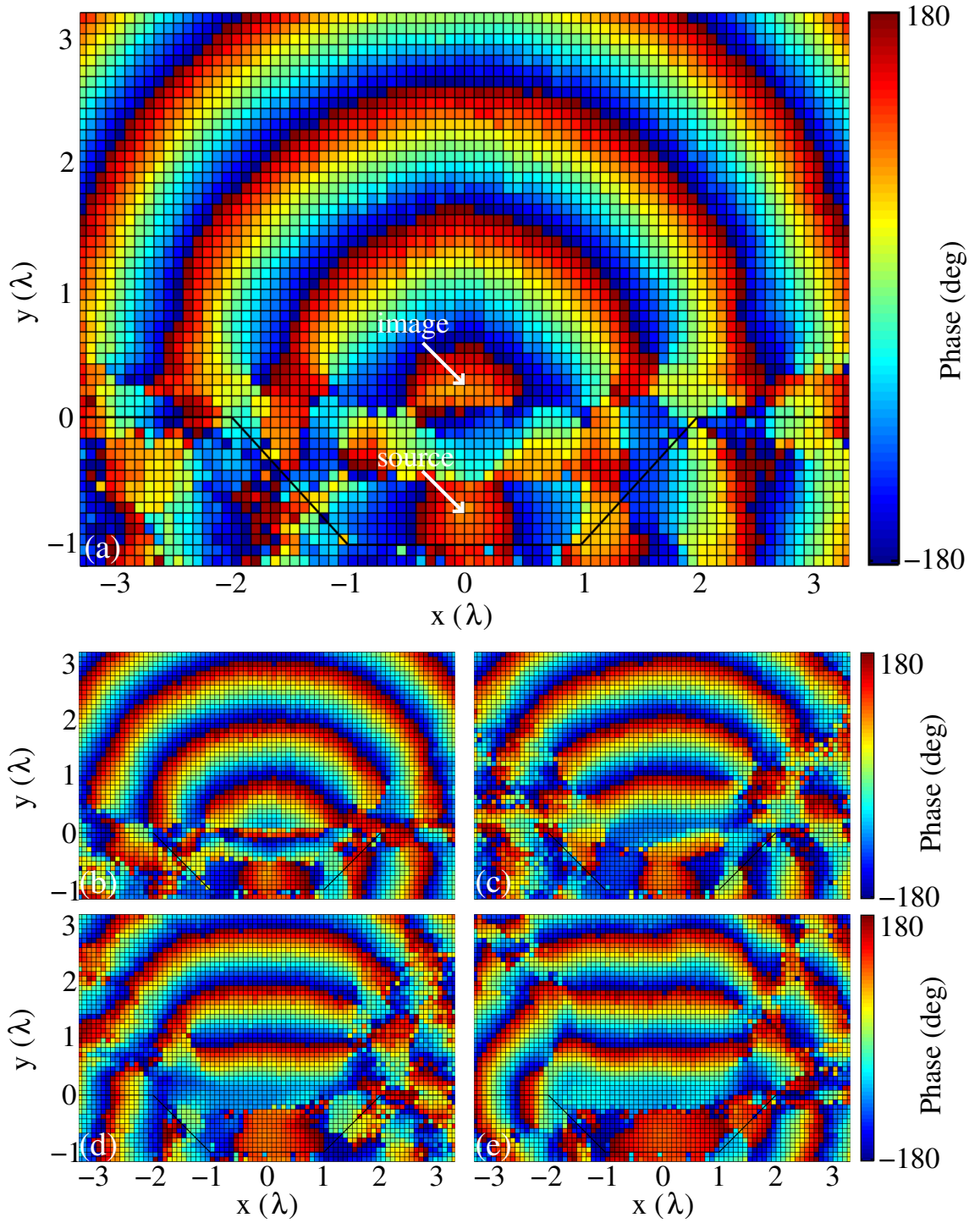


**Figure 5.17.** Measured electric field phase distributions around the design frequency  $f_0 = 5$  GHz. (a) At  $f = 4.92$  GHz. (b) At  $f = 4.85$  GHz. (c) At  $f = 5$  GHz. (d) At  $f = 5.03$  GHz. (e) At  $f = 5.06$  GHz.

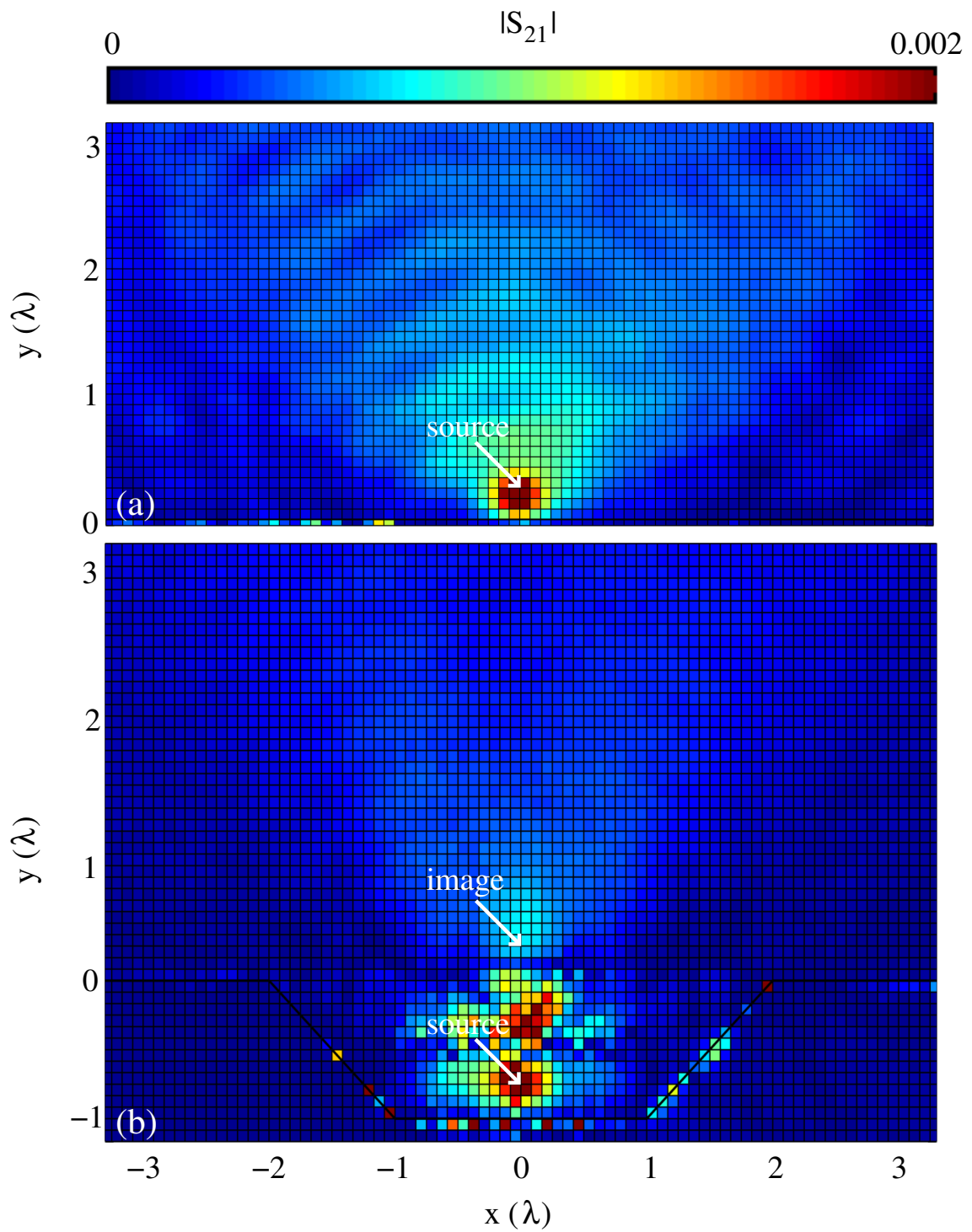


**Figure 5.18.** Measured electric field magnitude distributions at  $f = 4.92$  GHz. (a) Desired configuration. (b) Embedded configuration.

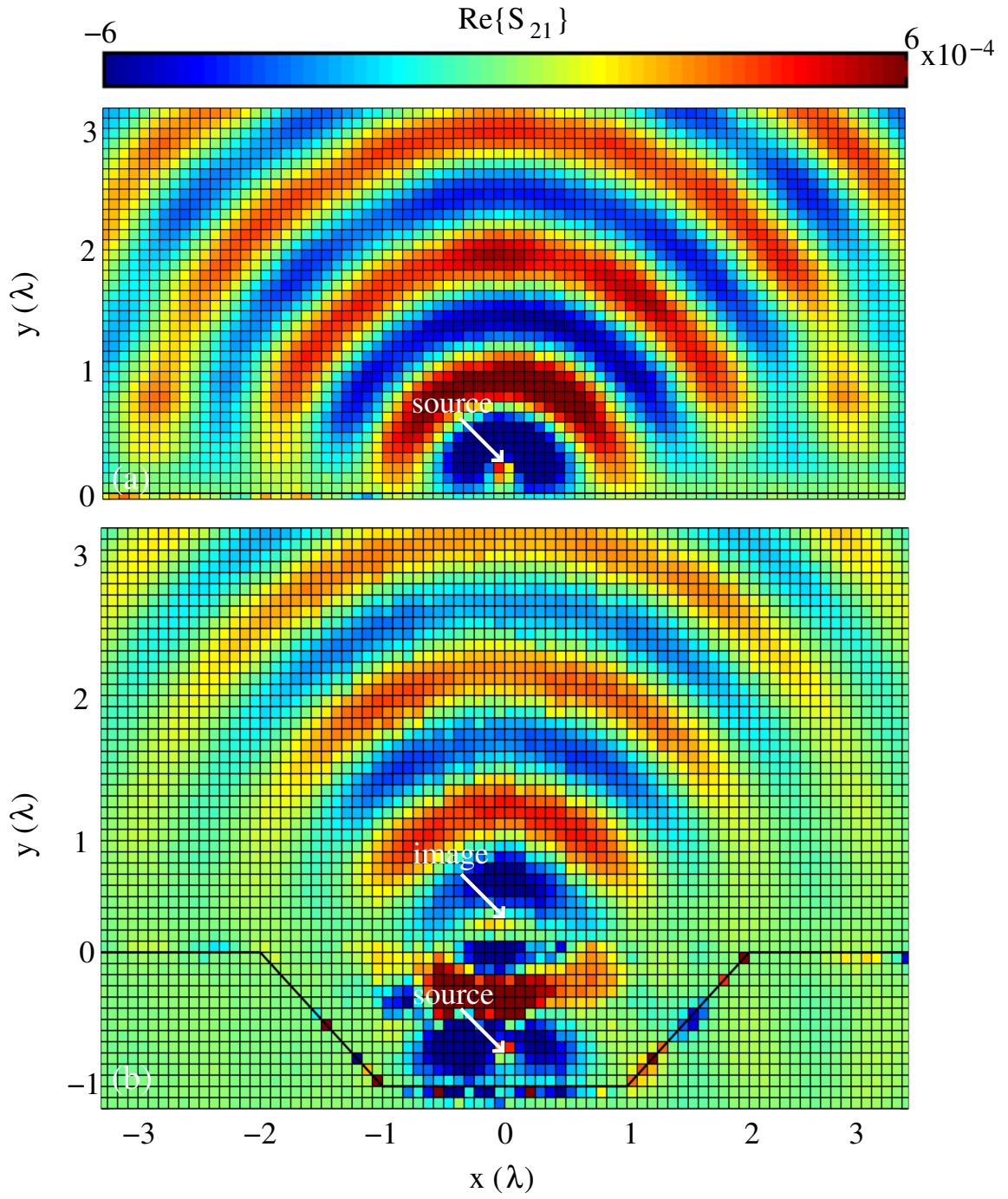


**Figure 5.19.** Measured electric field snapshots at  $f = 4.92$  GHz. (a) Desired configuration. (b) Embedded configuration.

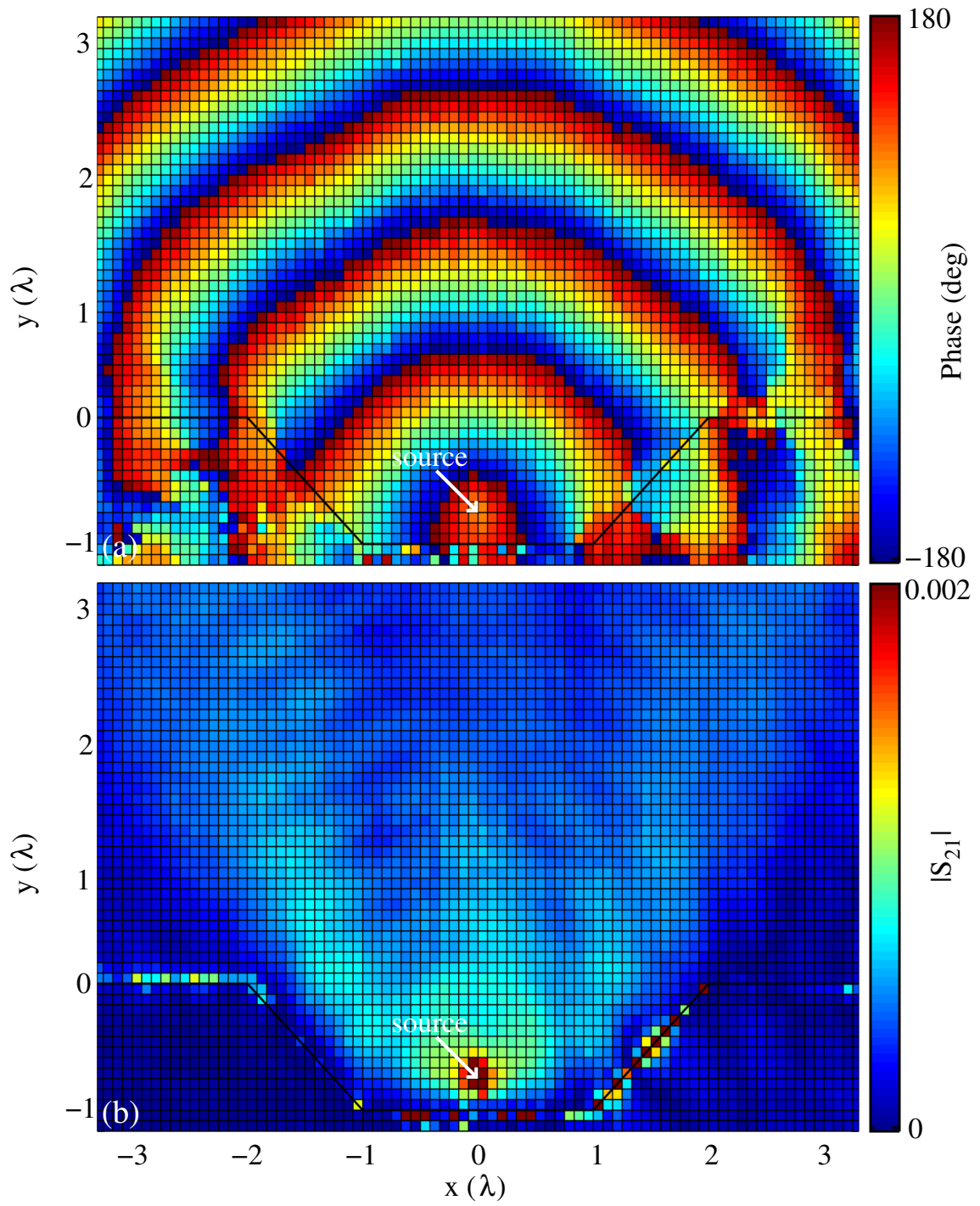


**Figure 5.20.** Measured electric field for an empty recess at  $f = 4.92$  GHz. (a) Phase distribution. (b) Magnitude distribution.

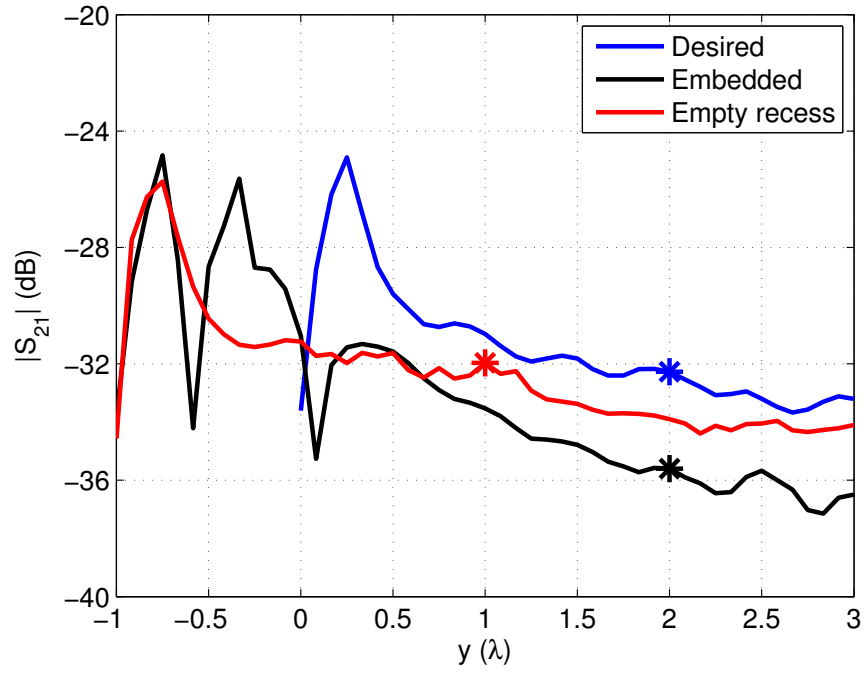


**Figure 5.21.** Measured  $S_{21}$  along  $x = 0$  at  $f = 4.92$  GHz.

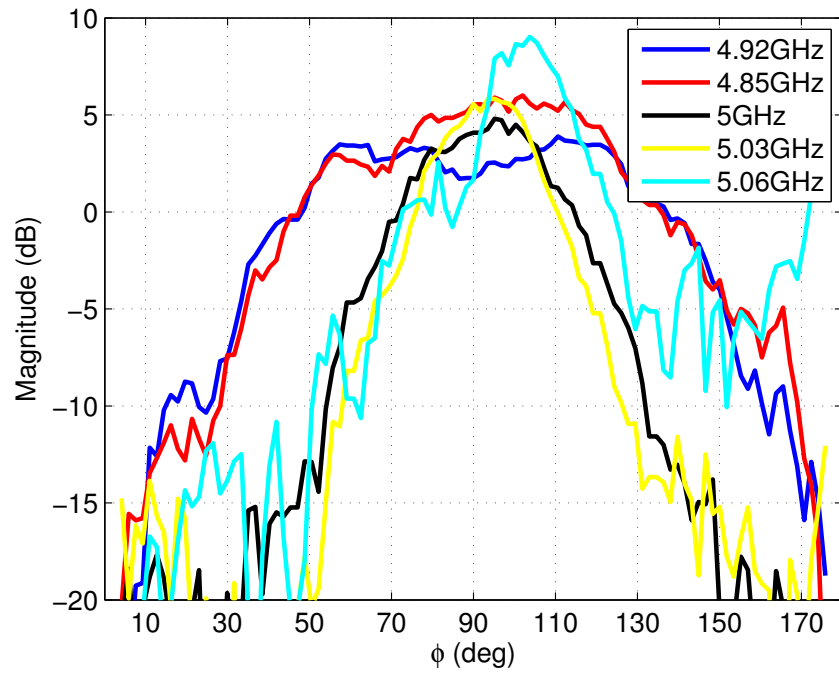


**Figure 5.22.** Measured near-field patterns for the embedded configuration.



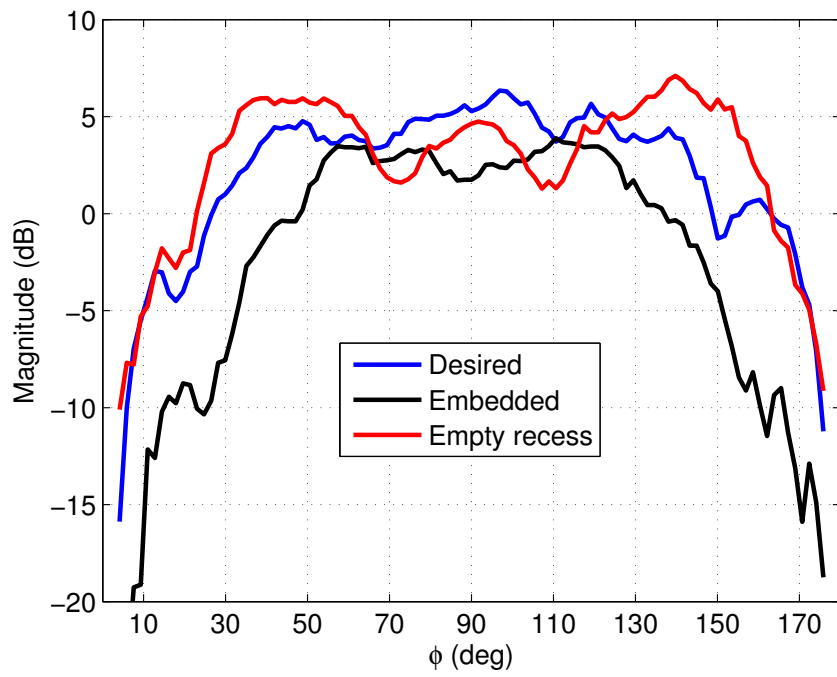


**Figure 5.23.** Measured near-field patterns at  $f = 4.92$  GHz.

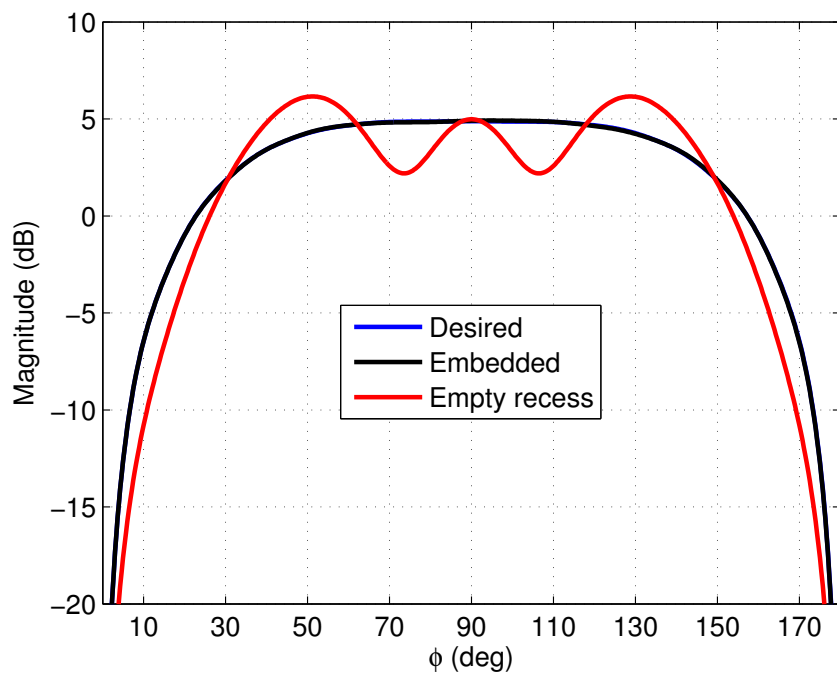


**Figure 5.24.** Simulated near-field patterns at  $f = 4.92$  GHz.

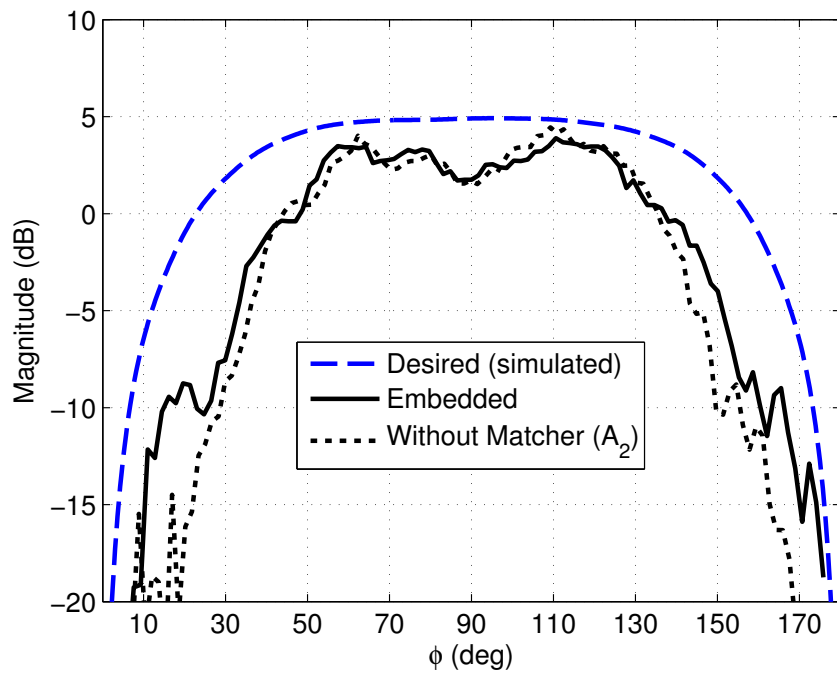


**Figure 5.25.** Effects of the matcher region  $A_2$  on the near-field pattern at  $f = 4.92$  GHz.

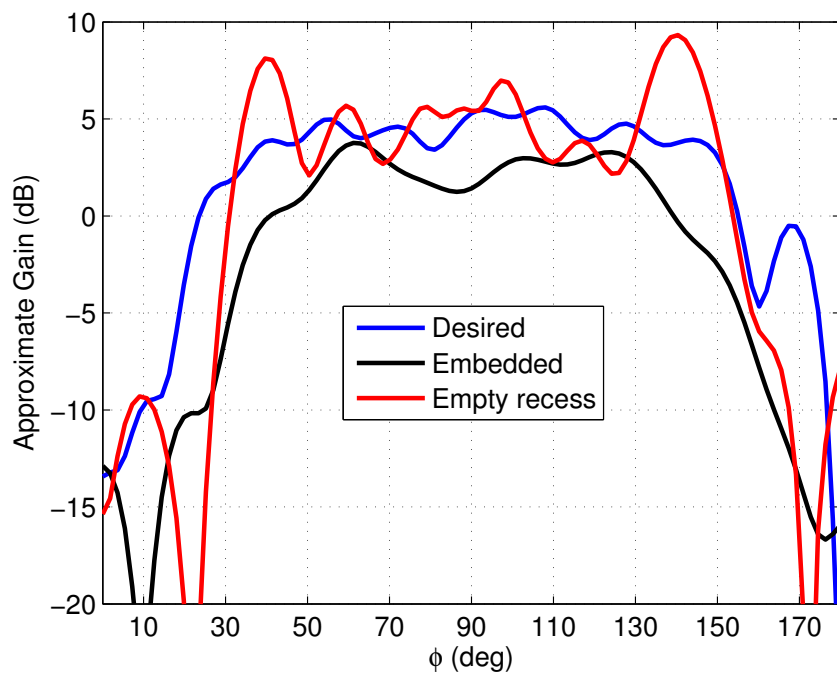


**Figure 5.26.** Approximate far-field gain patterns measured at  $f = 4.92$  GHz.

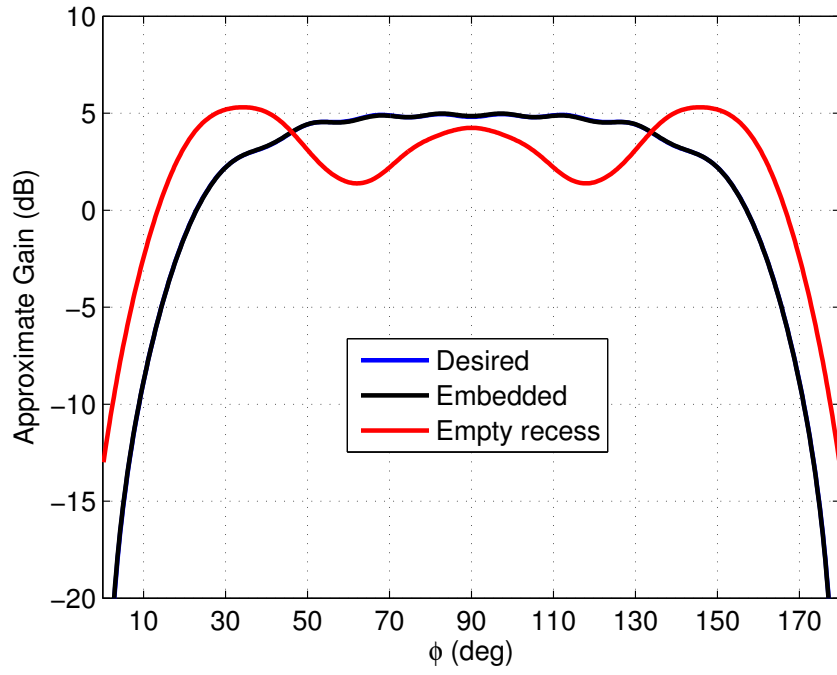


**Figure 5.27.** Simulated approximate far-field gain patterns at  $f = 4.92$  GHz.

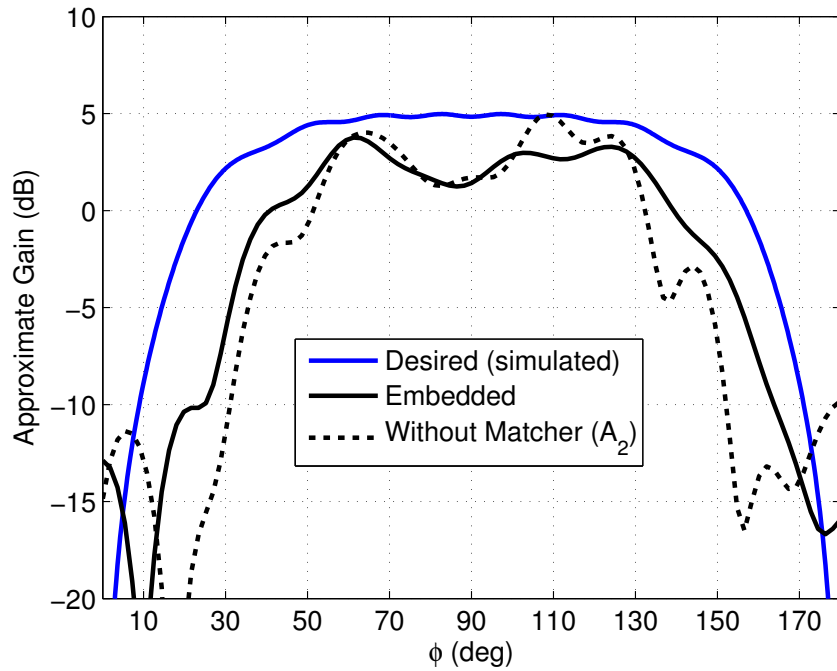


**Figure 5.28.** Effects of the matcher region  $A_2$  on the approximate far-field gain pattern at  $f = 4.92$  GHz.

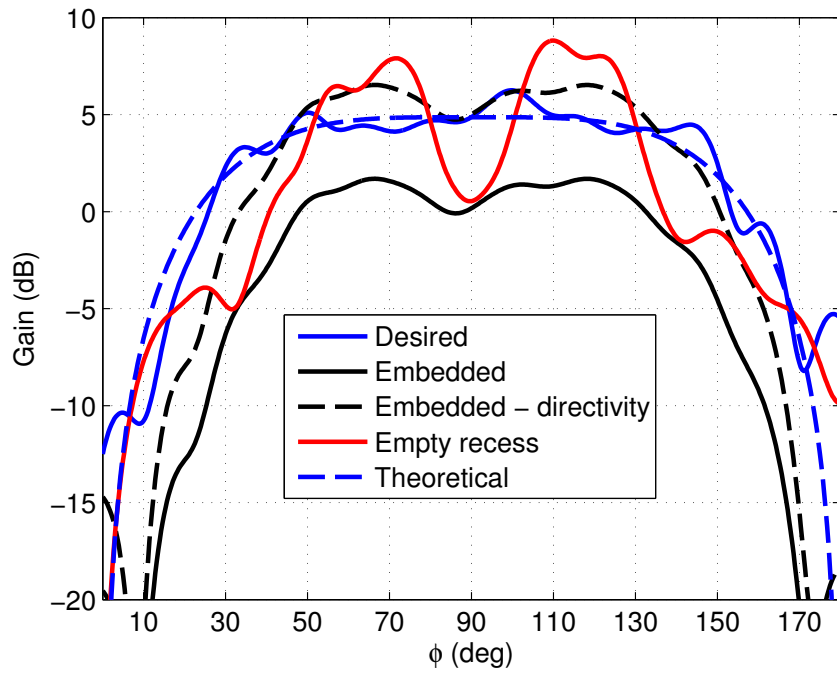


**Figure 5.29.** Numerically calculated far-field gain patterns for measurements at  $f = 4.92$  GHz.

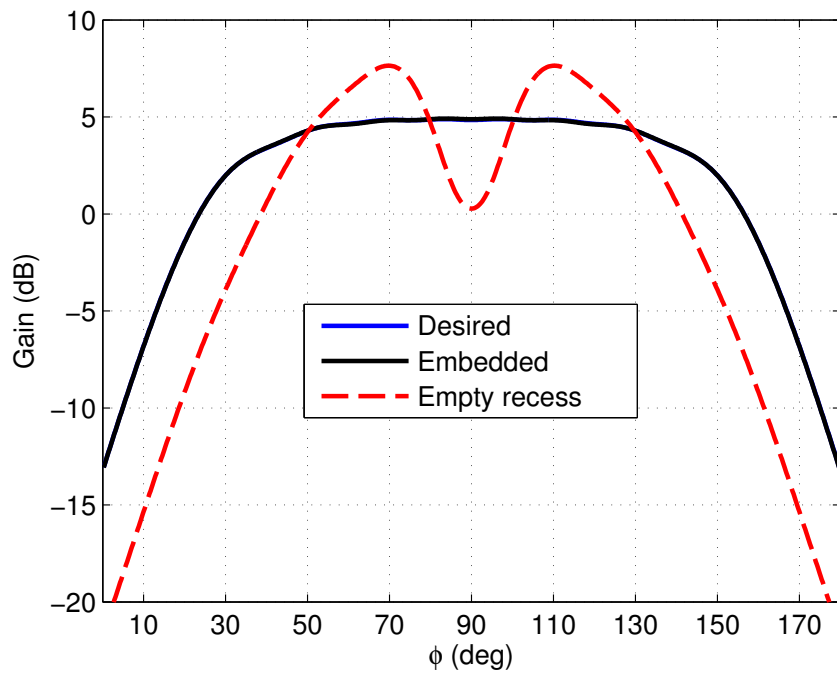


**Figure 5.30.** Simulated far-field gain patterns at  $f = 4.92$  GHz.

## CHAPTER 6

### 3-D METAMATERIAL-EMBEDDED MONOPOLE

A resonator-based metamaterial implementation of the 3-D effective medium for a virtual monopole antenna introduced in Chapter 2 will be presented in this chapter. Figure 2.1(b) illustrates the configuration based on the coordinate transformation. It is desired that a recessed embedded-monopole arrangement has the same far-zone radiation pattern as the original configuration, i.e., a monopole mounted on a flat ground plane. The required medium parameters were derived based on the coordinate transformation in Section 2.1.

At the chosen design frequency of  $f_0 = 5$  GHz, metamaterials are designed for fabrication using the standard PCB technologies. The standard parameter medium retrieval technique described in Section 3.1 is used in the extraction of the material parameters at the design frequency. For low-loss properties at high frequencies, Rogers Corporation's RT/Duroid 5880 laminates of thickness  $t_{sub} = 10$  mil with a 0.5-oz. copper cladding were chosen for the substrate. Except for the thickness that is half as thin, the substrate material is the same as that employed in the 2-D case of Chapter 5.

#### 6.1 Unit Cells for the Negative-Index Lens $A_3$

The region  $A_3$  represents a 3-D NIM superlens as shown in Figure 2.1. It has homogeneous, isotropic relative permeability and permittivity values simultaneously equal to -1. The central portion of the volume contains the  $z$ -axis ( $\rho = 0$ ). A metamaterial with a unit cell design based on the cylindrical coordinate system would have a singularity in the volumetric fill, which is undesirable. Hence, the NIM lens volume is divided into two volumes—the central circular cylinder and the outer toroid of triangular cross section. The

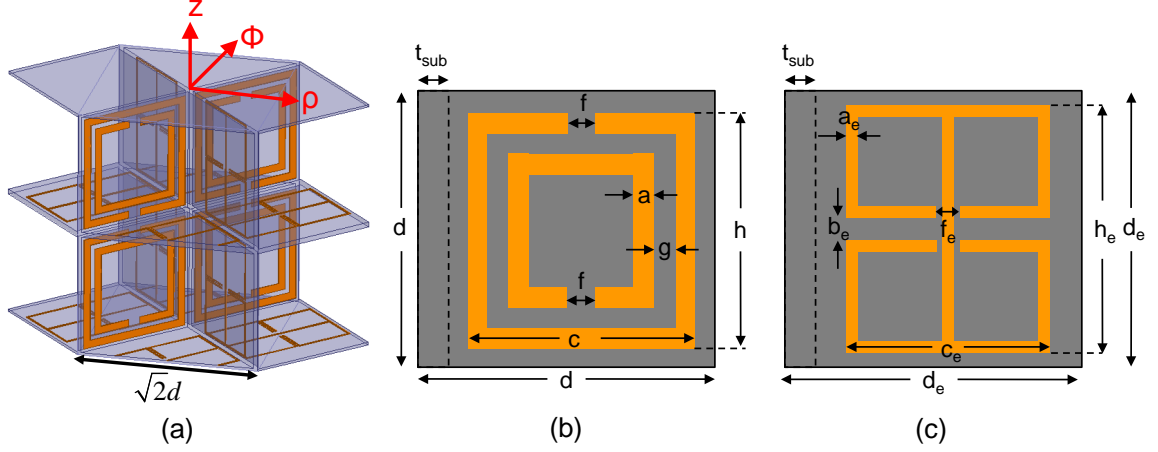


**Figure 6.1.** Unit cell of the outer NIM. (a) 3-D view. (b) The SRR face. (c) The ELC face. The side of the unit cell is equal to  $d\sqrt{2}$ .

unit cell for the central volume is designed on the Cartesian basis; a cell based on cylindrical basis is used for the outer volume.

The geometrical parameters of the unit cells were numerically optimized to obtain the index of refraction  $n = -1$  and the normalized impedance  $z = 1$ .

### 6.1.1 Outer volume

Figure 6.1 illustrates the unit cell chosen for the NIM lens volume in  $\rho > a$ . It consists of walls orthogonal to each other with each containing either an SRR or an ELC resonator (but not both). The polarization of the 3-D configuration is TM to  $z$  in the cylindrical  $(\rho, \phi, z)$  coordinate system, i.e., the magnetic field is  $\phi$ -directed and the electric field is orthogonal to  $\hat{\phi}$ . The SRRs control the effective permeability in the  $\phi$ -direction. The ELCs positioned in the two orthogonal planes control the effective permittivity in the  $\rho - z$  plane.

Similar to the NIM cell design for the 2-D application in Section 5.1, the unit cell was defined such that the substrate walls are positioned along the diagonal of the cubic elementary building block. This is to ensure that the unit cell structure becomes symmetric (except for a mirroring) in the direction of plane wave propagation for medium parameter retrieval. Following the same approach as in Section 5.1, minimizing the cost function

**Table 6.1.** Geometrical design parameters for the outer NIM unit cell (in mm).

	ELC		SRR
$a_e$	0.08	$a$	0.35
$b_e$	0.08	$c$	5.45
$c_e$	3.5	$d$	6.0
$f_e$	0.56	$g$	0.25
$d_e$	6.0	$h$	5.45
$h_e$	5.62	$f$	0.62

given in (5.1) was set to be the goal for the optimizations over the same set of geometrical parameters.

At 5 GHz, the optimized values are found to be  $n = -1.077 - j0.163$  and  $z = 0.836 - j0.008$ . The retrieved medium parameters associated with the optimized geometrical parameters are shown in Figure 6.2 with respect to frequency. The geometrical parameters for the optimized cell are given in Table 6.1.

Negative index of refraction is observed in 4.84–5.21 GHz. Compared with the 2-D NIM response of Section 5.1, we note that the bandwidth is narrower. This is primarily due to the ELC, which is roughly half as tall as the ELC used for the 2-D NIM. Unlike the 2-D configuration which allowed the ELC design to cover two unit cells, making one ELC per unit cell is a necessity for the 3-D application.

### 6.1.2 Central volume

For the NIM lens volume in  $\rho < a$ , the unit cell structure shown in Figure 6.3 is adopted. It consists of walls orthogonal to each other, each containing either an SRR or an ELC resonator. Unlike the NIM unit cell in the outer region, both an ELC and an SRR exist on two out of three walls of the elementary cubic block. The ELCs on the substrate walls in three orthogonal directions control the effective permittivity, and the SRRs adjust the effective permeability of the homogenized medium. Since the magnetic field does not

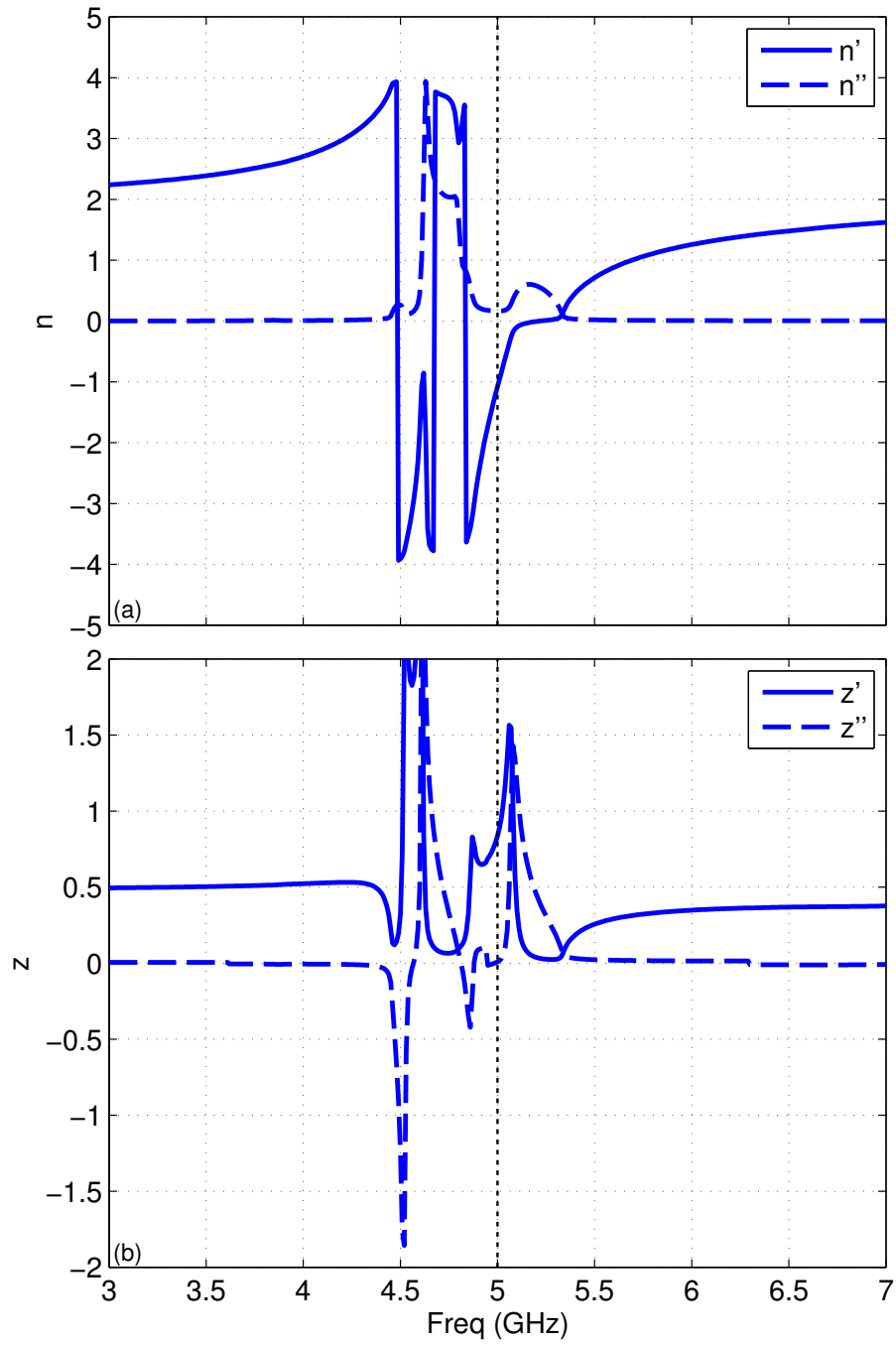


**Figure 6.2.** The retrieved medium parameters of the optimized outer NIM unit cell. (a) Index of refraction  $n = n' - jn''$ . (b) Impedance  $z = z' - jz''$ .



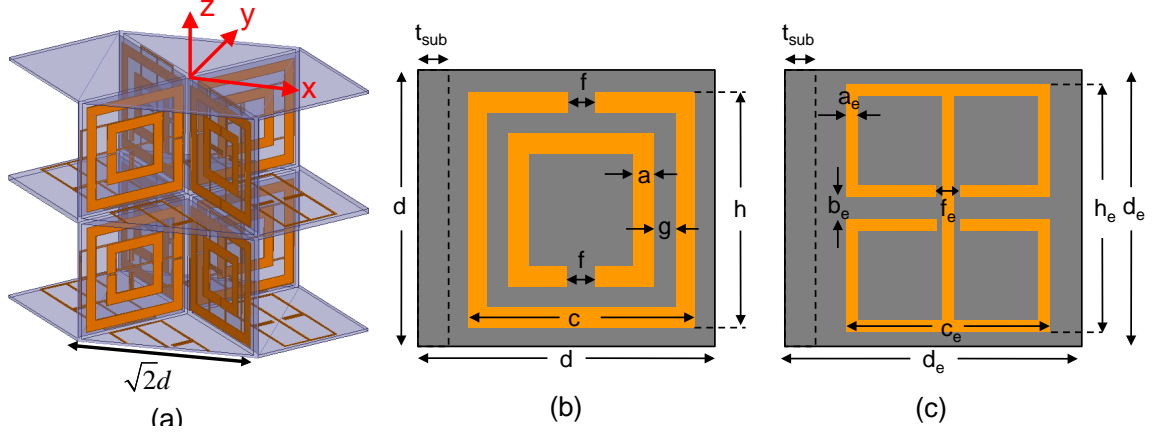


**Figure 6.3.** Unit cell of the central NIM. (a) 3-D view. (b) The SRR face. (c) The ELC face. The side of the unit cell is equal to  $d\sqrt{2}$ .

**Table 6.2.** Geometrical design parameters for the central NIM unit cell (in mm).

	ELC		SRR
$a_e$	0.08	$a$	0.5
$b_e$	0.08	$c$	5.2
$c_e$	2.82	$d$	6.0
$f_e$	0.58	$g$	0.6
$d_e$	6.0	$h$	5.2
$h_e$	5.59	$f$	0.08

have a  $z$ -component due to symmetry, there is no need to place an SRR in the unit cell wall that is parallel to the  $xy$ -plane.

Geometrical parameters of the unit cell design were optimized using a GA algorithm in HFSS. The cost function to be minimized by the optimization was also set to (5.1) as in the cell optimization for the outer NIM volume. The geometrical parameters for the optimized cell are given in Table 6.2. At 5 GHz, the optimized values medium parameters were found to be  $n = -1.156 - j0.930$  and  $z = 0.324 - j0.377$ . The retrieved medium parameters associated with the optimized geometrical parameters are shown in Figure 6.4 with respect to frequency.

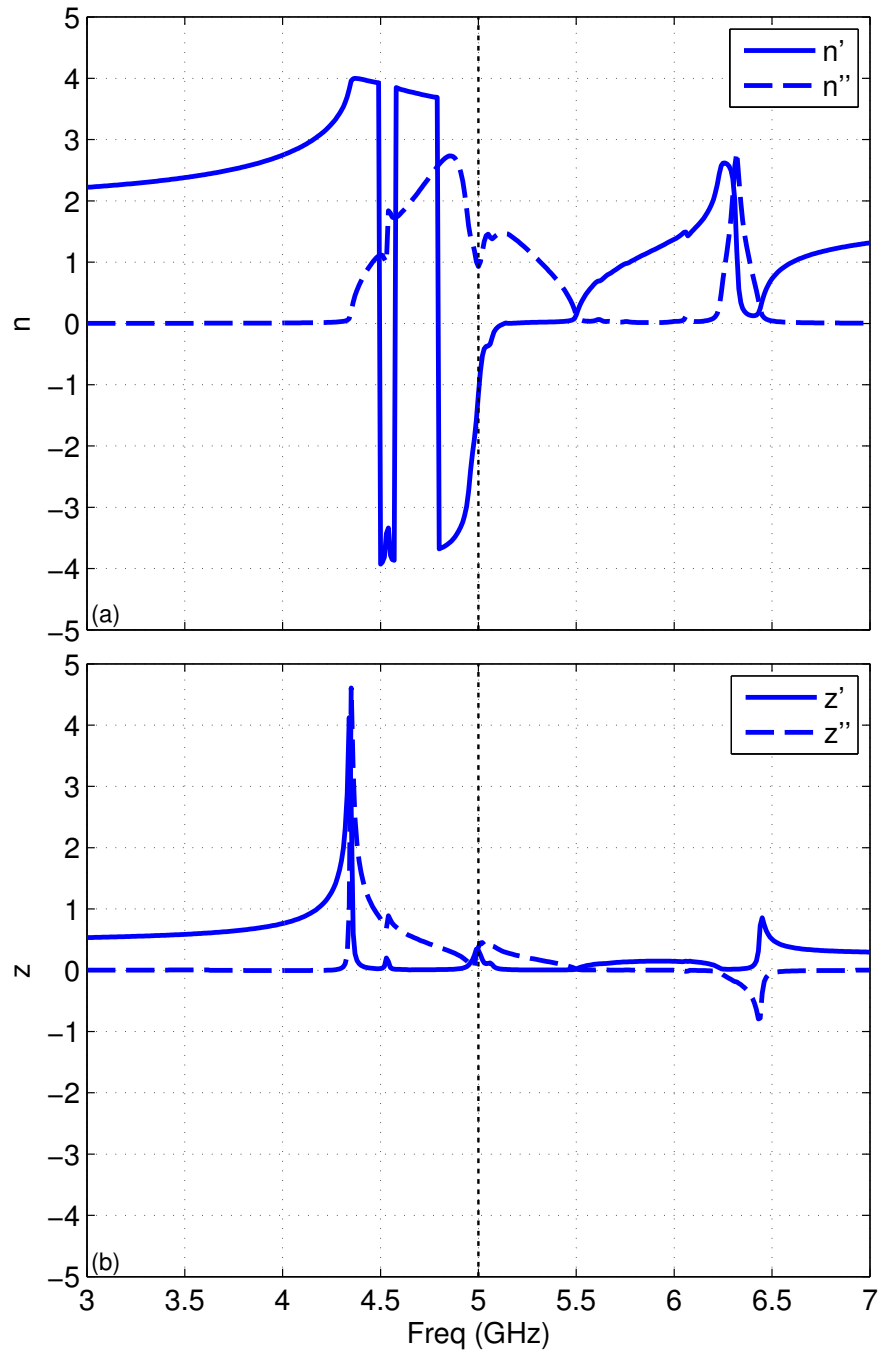


**Figure 6.4.** The retrieved medium parameters of the optimized central NIM unit cell. (a) Index of refraction  $n = n' - jn''$ . (b) Impedance  $z = z' - jz''$ .

Compared with the outer NIM, the cell exhibits a higher loss with a poor match over the negative index of refraction band of 4.8–5.13 GHz. The optimal value of cost was 1.488. In contrast, cost was minimized to 0.060 for the outer NIM. The inferior performance of this NIM cell is attributed to having more number of resonators and stronger coupling due to having two resonators on the two sides of one wall.

## 6.2 Unit Cells for the Matcher $A_2$

Anisotropic material parameters are required for  $A_2$ . Written in the cylindrical  $(\rho, \phi, z)$  coordinate system, the permittivity tensor  $\epsilon$  in the  $\rho - z$  plane has non-zero off diagonal terms in

$$\epsilon = \begin{bmatrix} \epsilon_{\rho\rho} & \epsilon_{\rho z} \\ \epsilon_{z\rho} & \epsilon_{zz} \end{bmatrix} = \begin{bmatrix} 1 & 1 \\ 1 & 2 \end{bmatrix}. \quad (6.1)$$

The permeability  $\mu_{\phi\phi}$  is equal to 1. In this section, two unit cell designs for the matcher metamaterial in  $A_2$  will be presented.

### 6.2.1 Rotated cubic unit cell

A diagonalization of  $\epsilon$  similar to the one in Section 5.2 may also be used to design the 3-D matcher unit cell having

$$\epsilon = \begin{bmatrix} \epsilon_{\rho\rho} & \epsilon_{\rho z} \\ \epsilon_{z\rho} & \epsilon_{zz} \end{bmatrix} = \begin{bmatrix} 1 & 1 \\ 1 & 2 \end{bmatrix} = \mathbf{V} \begin{bmatrix} \epsilon_{11} & 0 \\ 0 & \epsilon_{22} \end{bmatrix} \mathbf{V}^T \quad (6.2)$$

and  $\mu_{\phi\phi} = 1$ , where the eigenvectors  $v_1$  and  $v_2$  are given by (5.3). The scalars  $\epsilon_{11} = 2.618$  and  $\epsilon_{22} = 0.382$  are the associated eigenvalues—implying that the permittivity tensor will be a diagonal matrix when written in the  $(v_1, v_2, \phi)$  coordinate system. This is equal to the  $(\rho, \phi, z)$  system rotated around the  $\phi$ -axis by  $58.3^\circ$ .

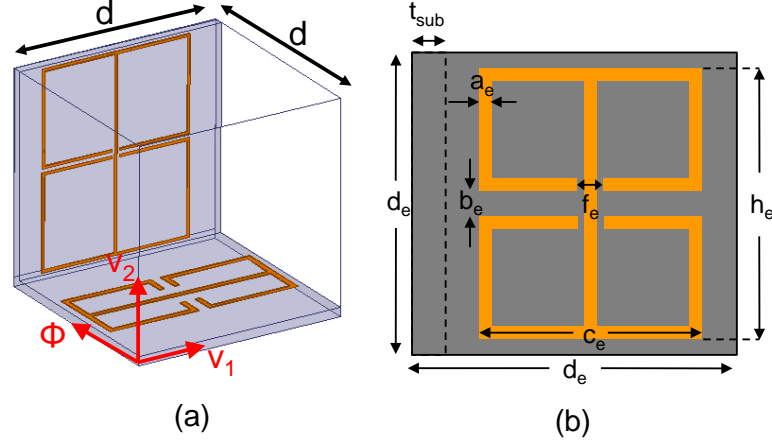


**Figure 6.5.** The cubic unit cell for  $A_2$ . (a) A 3-D view. (b) The ELC faces.

The unit cell is shown in Figure 6.5. It consists of two orthogonal walls along the  $v_1$  and  $v_2$  directions, containing ELC resonators of different dimensions on the two walls. Each ELC resonator is responsible for adjusting the permittivity along the resonator axis direction. The geometrical parameter values of the optimized design are listed in Table 6.3.

Using plane waves illuminating the unit cell propagating in the  $v_1$  and  $v_2$  directions, separate GA optimizations were performed to optimize the dimensions of the ELC excited by the plane wave. Once both ELC dimensions were determined, it was confirmed that the final cell design is optimal for both  $\epsilon_{11}$  and  $\epsilon_{22}$ . For the optimized unit cell, the effective medium parameters  $\epsilon_{11}$  and  $\mu_{\phi\phi}$  are plotted with respect to frequency in Figure 6.6(a) and (b), respectively, retrieved from scattering analysis of a plane wave propagating in the  $v_2$  direction. At 5 GHz, it was found that  $\epsilon_{11} = 2.629 - j0.039$  and  $\mu_{\phi\phi} = 0.949 + j0.012$ . From scattering analysis of a plane wave propagating in the  $v_1$  direction, the retrieved parameters  $\epsilon_{22}$  and  $\mu_{\phi\phi}$  are plotted in Figure 6.7(c) and (d), respectively. At 5 GHz, the metamaterial exhibits  $\epsilon_{22} = 0.394 - j0.046$  and  $\mu_{\phi\phi} = 1.224 + j0.025$ .

### 6.2.2 Parallelogram cross-section unit cell

Figure 6.8(a) and (b) shows the rotated cubic unit cell that are arranged to fill the region  $A_2$  and highlights the resulting unfilled space with this filling scheme, respectively. The

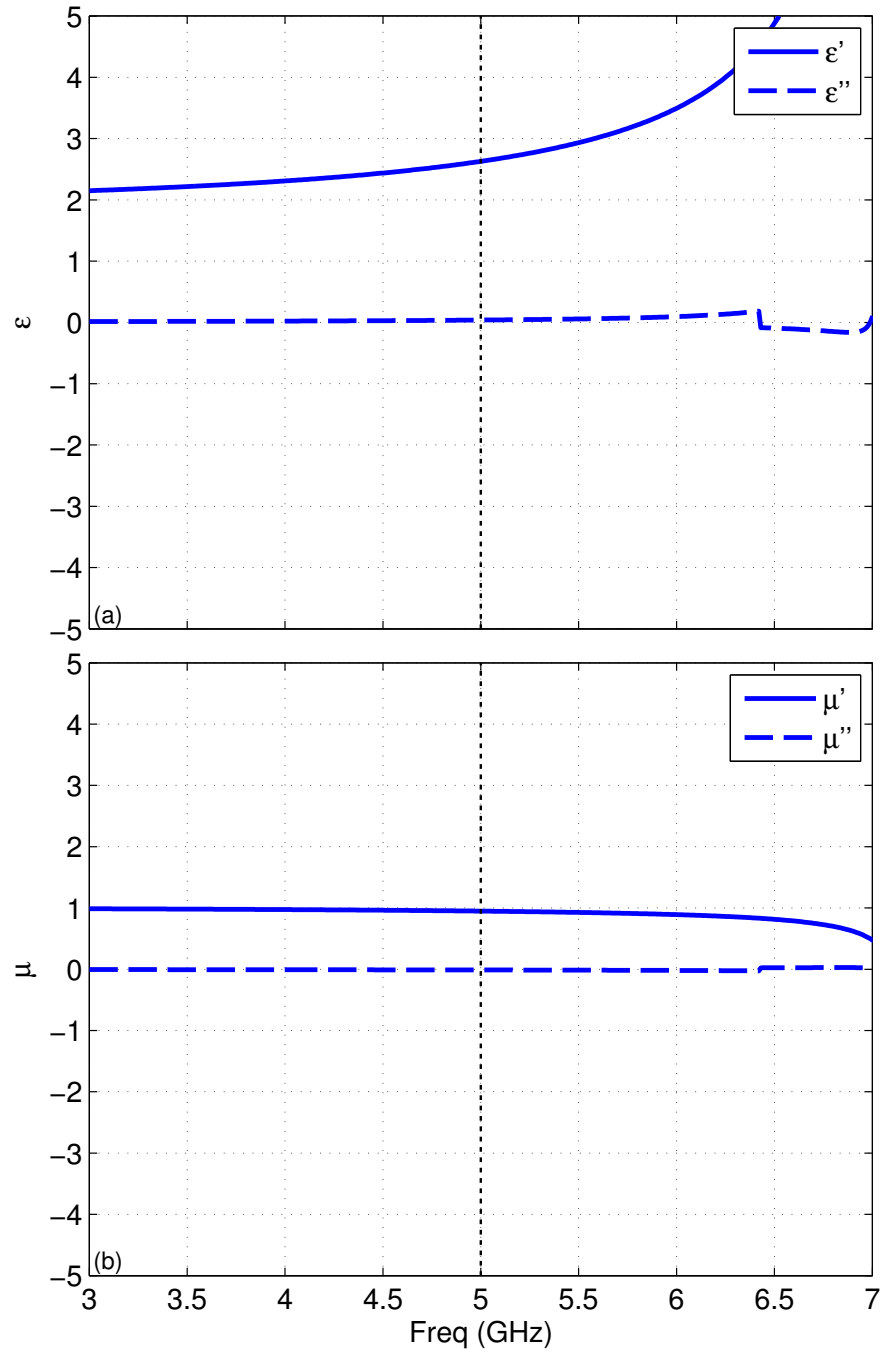


**Figure 6.6.** The retrieved medium parameters of the optimized cubic unit cell for  $A_2$ . (a)  $\epsilon_{11}$ . (b)  $\mu_{\phi\phi}$ .

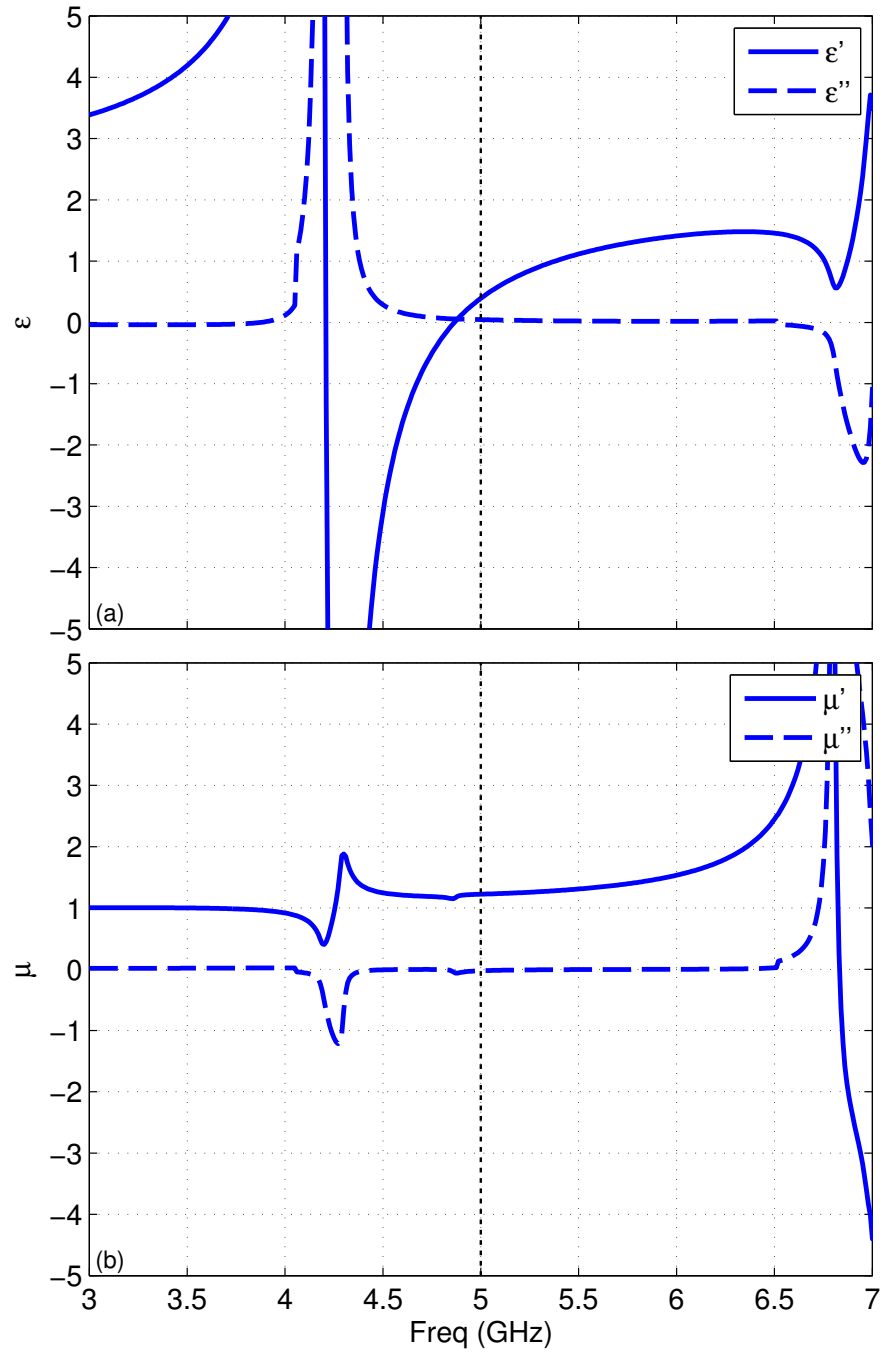


**Figure 6.7.** The retrieved medium parameters of the optimized cubic unit cell for  $A_2$ . (a)  $\epsilon_{22}$ . (b)  $\mu_{\phi\phi}$ .

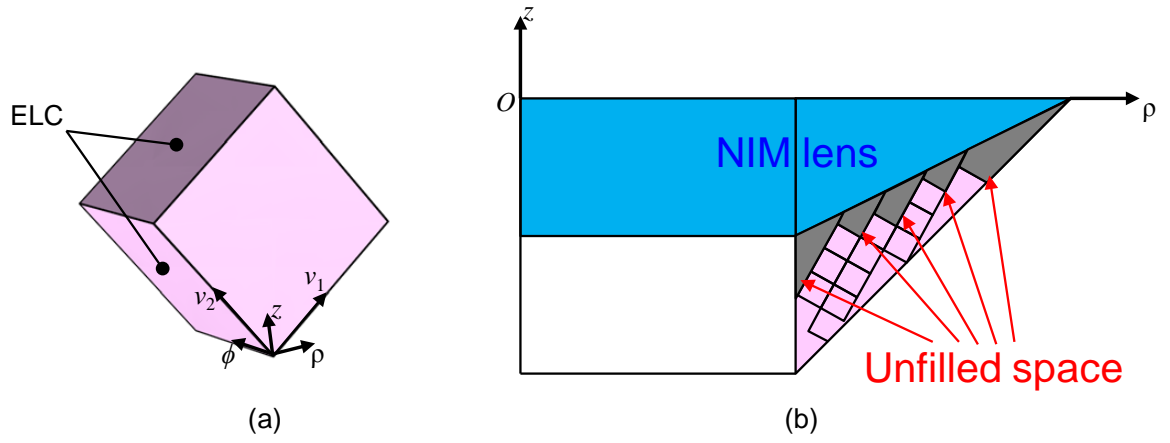


**Figure 6.8.** Metamaterial for  $A_2$ . (a) Rotated cubic unit cell. (b) Volumetric fill for a matcher constructed with the rotated cubic unit cell.

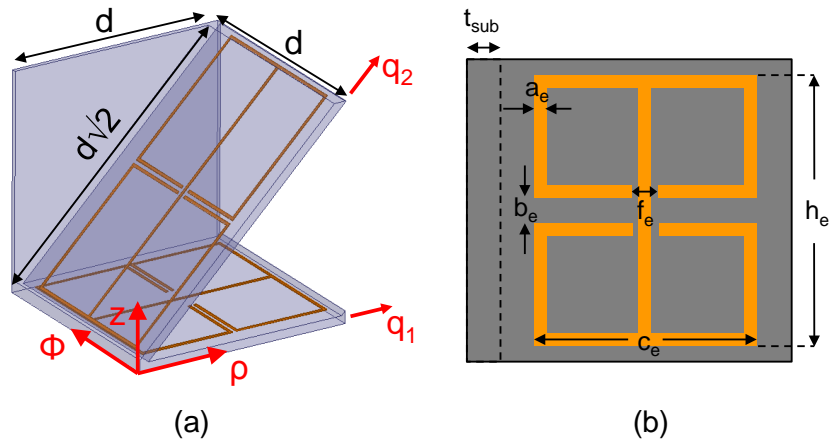


**Figure 6.9.** The parallelogram cross-section unit cell for  $A_2$ . (a) A 3-D view. (b) The ELC faces.

**Table 6.3.** Geometrical design parameters for the rotated cubic matcher unit cell (in mm).

ELC 1		ELC 2	
$a_e$	0.15	$a_e$	0.08
$b_e$	0.3	$b_e$	0.1
$c_e$	2.32	$c_e$	4.4
$f_e$	1	$f_e$	0.52
$h_e$	5.6	$h_e$	5.6

volumetric fill is very poor due to the cubic unit cell structure not aligning well with the boundary surface of  $A_2$ . Instead of using a cubic unit cell, a unit cell with non-orthogonal face normals geometry can be designed for a more effective fill of the volume  $A_2$ . Therefore, we consider a unit cell with a parallelogram cross-section in the  $\rho - z$  plane as shown in Figure 6.9. A design approach for the non-orthogonal TL grid in Section 3.2 can be utilized to design such a unit cell.

The relative medium parameters for  $A_2$  are equal to

$$\epsilon = \mathbf{I} + \chi = \begin{bmatrix} 1 & 1 \\ 1 & 2 \end{bmatrix}, \quad (6.3)$$

expressed in  $(\rho, z)$ , where  $\mathbf{I}$  is the identity dyad, and

$$\chi = \begin{bmatrix} \chi_{\rho\rho} & \chi_{\rho z} \\ \chi_{z\rho} & \chi_{zz} \end{bmatrix} \quad (6.4)$$

is the electric susceptibility tensor. The relative medium permeability  $\mu_{\phi\phi}$  is equal to 1. Let  $\hat{q}_1$  and  $\hat{q}_2$  in Figure 6.9(a) make angles  $\phi_1$  and  $\phi_2$  from the  $+\rho$  axis such that

$$\hat{q}_1 = \hat{\rho} \cos \alpha_1 + \hat{z} \sin \alpha_1, \quad (6.5)$$

$$\hat{q}_2 = \hat{\rho} \cos \alpha_2 + \hat{z} \sin \alpha_2. \quad (6.6)$$



Expressed in the  $(q_1, q_2)$  system, the effective electric susceptibility represented by the unit cell is a diagonal tensor:

$$\chi' = \begin{bmatrix} \chi_{11} & 0 \\ 0 & \chi_{22} \end{bmatrix}. \quad (6.7)$$

Now we consider a coordinate rotation from  $(q_1, q_2)$  to  $(\rho, z)$ . The electric susceptibility tensor parameters in the  $(\rho, z)$  are then expressed by [28]

$$\chi = \frac{\mathbf{A}\chi'\mathbf{A}^T}{|\mathbf{A}|}. \quad (6.8)$$

One finds that

$$\tan \alpha_1 = -\frac{\chi_{zz} \cos \alpha_2 - \chi_{\rho z} \sin \alpha_2}{\chi_{\rho\rho} \sin \alpha_2 - \chi_{\rho z} \cos \alpha_2} \quad (6.9)$$

in reciprocal media.

To realize the particular set of medium parameters for  $A_2$  in (6.3), we obtain  $\alpha_2 = 45^\circ$  for  $\alpha_1 = 0$  as a possible realization. The unit cell with the wall directions defined by angles  $\alpha_1$  and  $\alpha_2$  provides a more efficient fill of the volume  $A_2$  in comparison with the rotated cubic cell of Subsection 6.2.1. The cell consists of two walls  $45^\circ$  apart in the  $\rho - z$  plane. Each wall contains an ELC resonator in different dimensions as illustrated in Figure 6.9(a). The unit cell and the arrangement of the cells for filling  $A_2$  are illustrated in Figures 6.10(a)–6.10(b). The two ELCs in the cell can be optimized to synthesize the effective permittivity tensor in the  $\rho - z$  plane.

The homogenized parameter retrieval procedure for an anisotropic medium described in Section 3.3 is employed. For each of the three different directions of plane wave illumination in the  $\rho z$ -plane, the unit cell is arranged in a perpendicular direction to form a metamaterial slab and analyzed for scattering parameters. This uniquely determines the

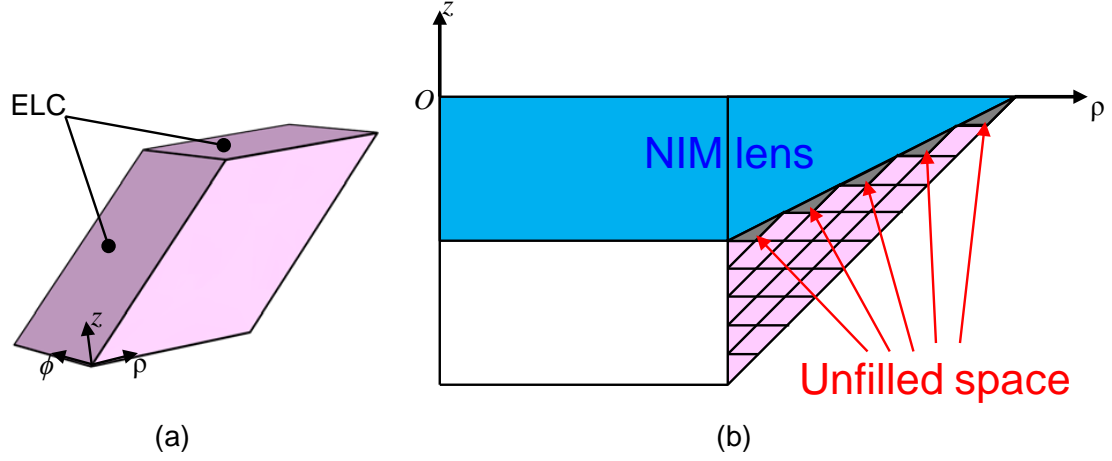


**Figure 6.10.** Metamaterial for  $A_2$ . (a) Parallelogram cross-section unit cell. (b) Volumetric fill for a matcher constructed with the parallelogram cross-section unit cell.

**Table 6.4.** Geometrical design parameters for the parallelogram cross section matcher unit cell (in mm).

	ELC 1		ELC 2
$a_e$	0.08	$a_e$	0.08
$b_e$	0.1	$b_e$	0.1
$c_e$	5	$c_e$	4.51
$f_e$	1.05	$f_e$	0.3
$h_e$	5.4	$h_e$	7.9

effective medium parameters. The three different incidence directions were chosen to be  $\theta = 0, 90^\circ, -45^\circ$  measured from the  $+\rho$ -axis direction. Figure 6.11 shows the retrieved permittivity and permeability plots with respect to frequency. At the design frequency, the effective anisotropic permittivity tensor for this cell is found to be

$$\epsilon = \begin{bmatrix} \epsilon_{\rho\rho} & \epsilon_{\rho z} \\ \epsilon_{z\rho} & \epsilon_{zz} \end{bmatrix} = \begin{bmatrix} 1.033 - j0.051 & 0.798 + j0.023 \\ 0.798 + j0.023 & 1.488 + j0.038 \end{bmatrix}. \quad (6.10)$$

The average effective permeability value of the unit cell obtained from the analysis is  $\mu_{\phi\phi} = 0.940 - j0.061$ . For the optimized unit cell, the retrieved parameters  $\epsilon_{\rho\rho}$ ,  $\epsilon_{z\rho}$ ,  $\epsilon_{zz}$  and  $\mu_{\phi\phi}$

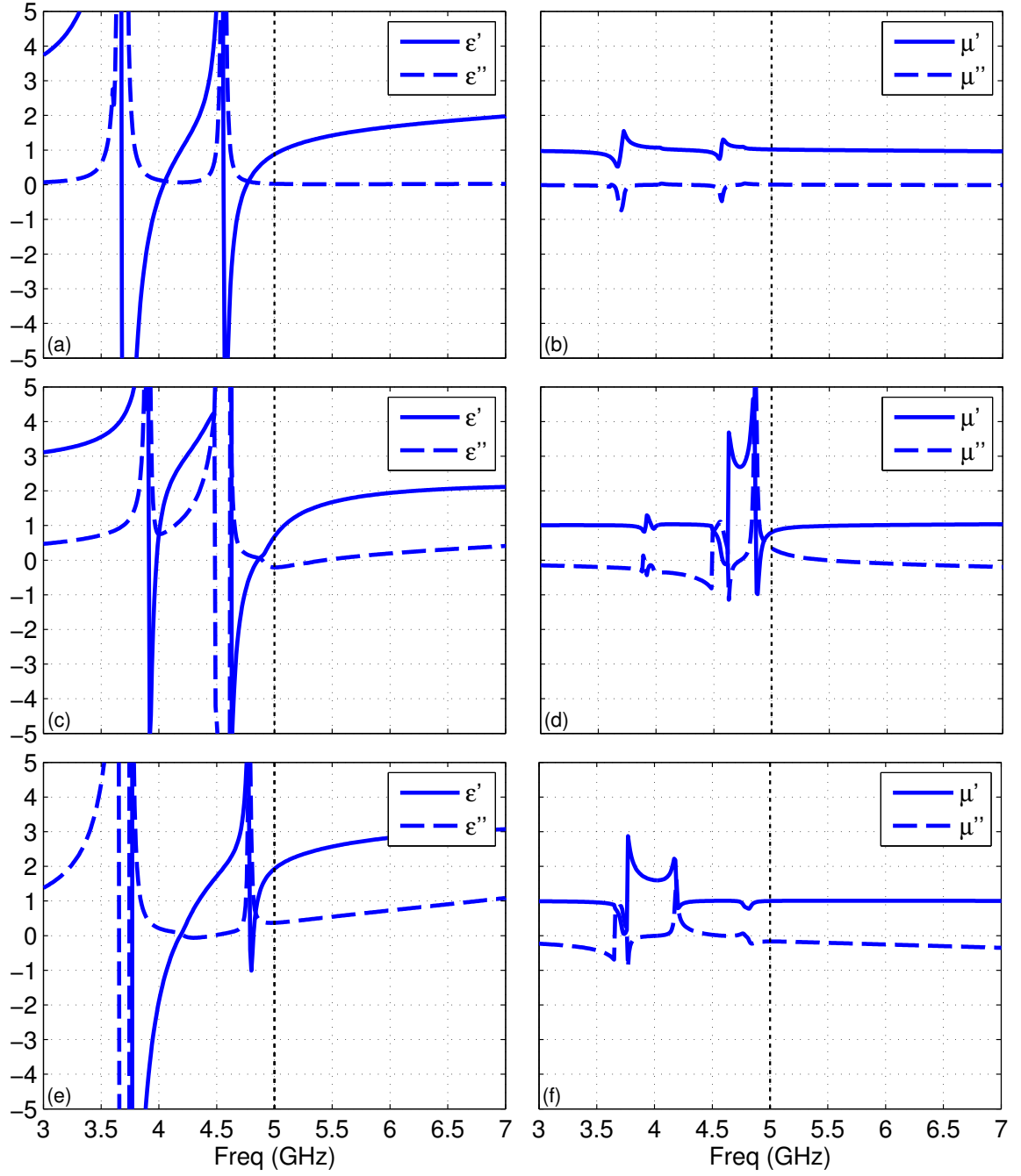


**Figure 6.11.** The retrieved medium parameters of the optimized parallelogram cross-section matcher unit cell for  $A_2$ . (a)-(b), (c)-(d), (e)-(f) show the effective relative  $\epsilon - \mu$  in  $\theta = 0, 90, -45^\circ$  plane wave incidence directions, respectively.

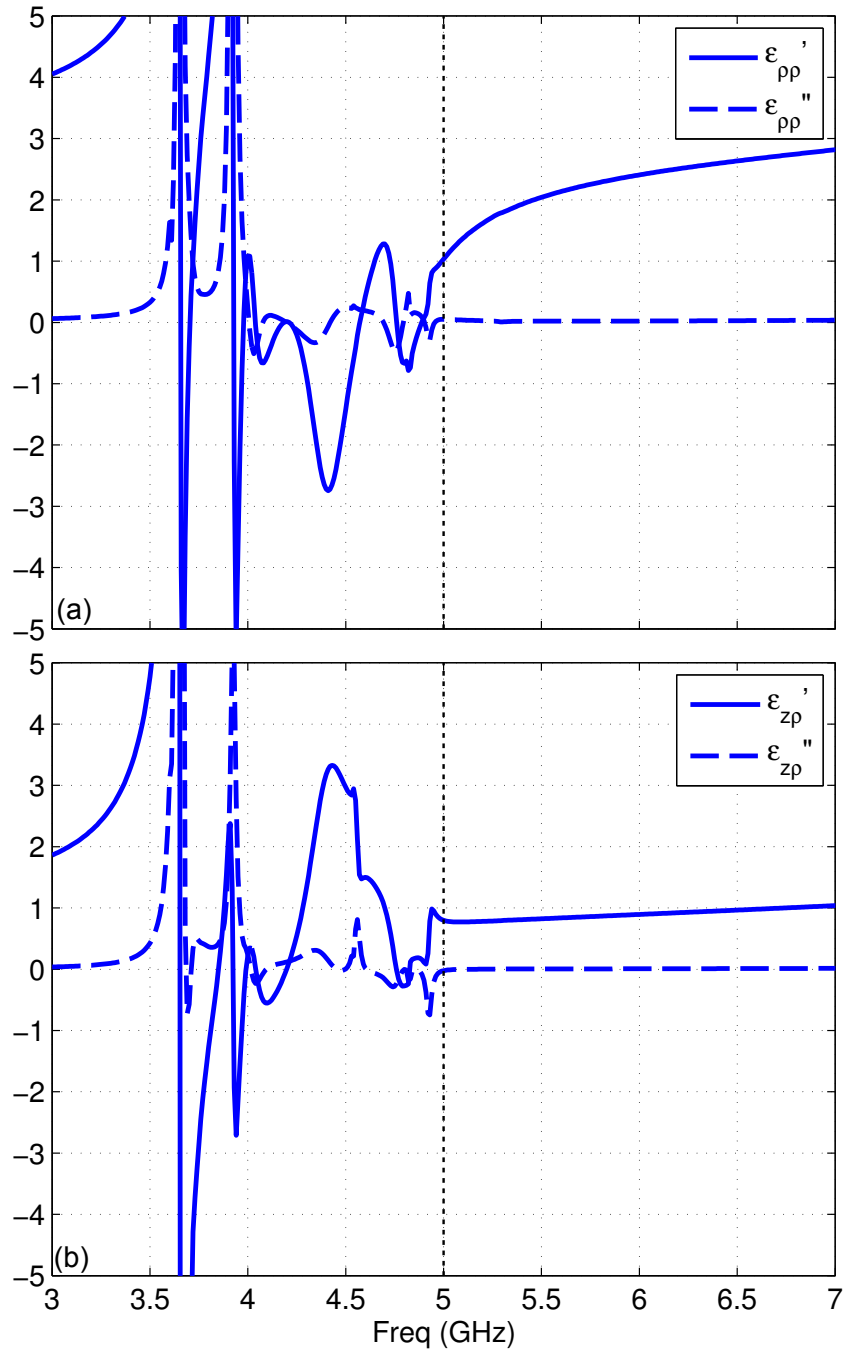


**Figure 6.12.** The retrieved medium parameters of the optimized parallelogram cross-section matcher unit cell for  $A_2$ . (a)  $\epsilon_{\rho\rho}$ . (b)  $\epsilon_{\rho z}$ .

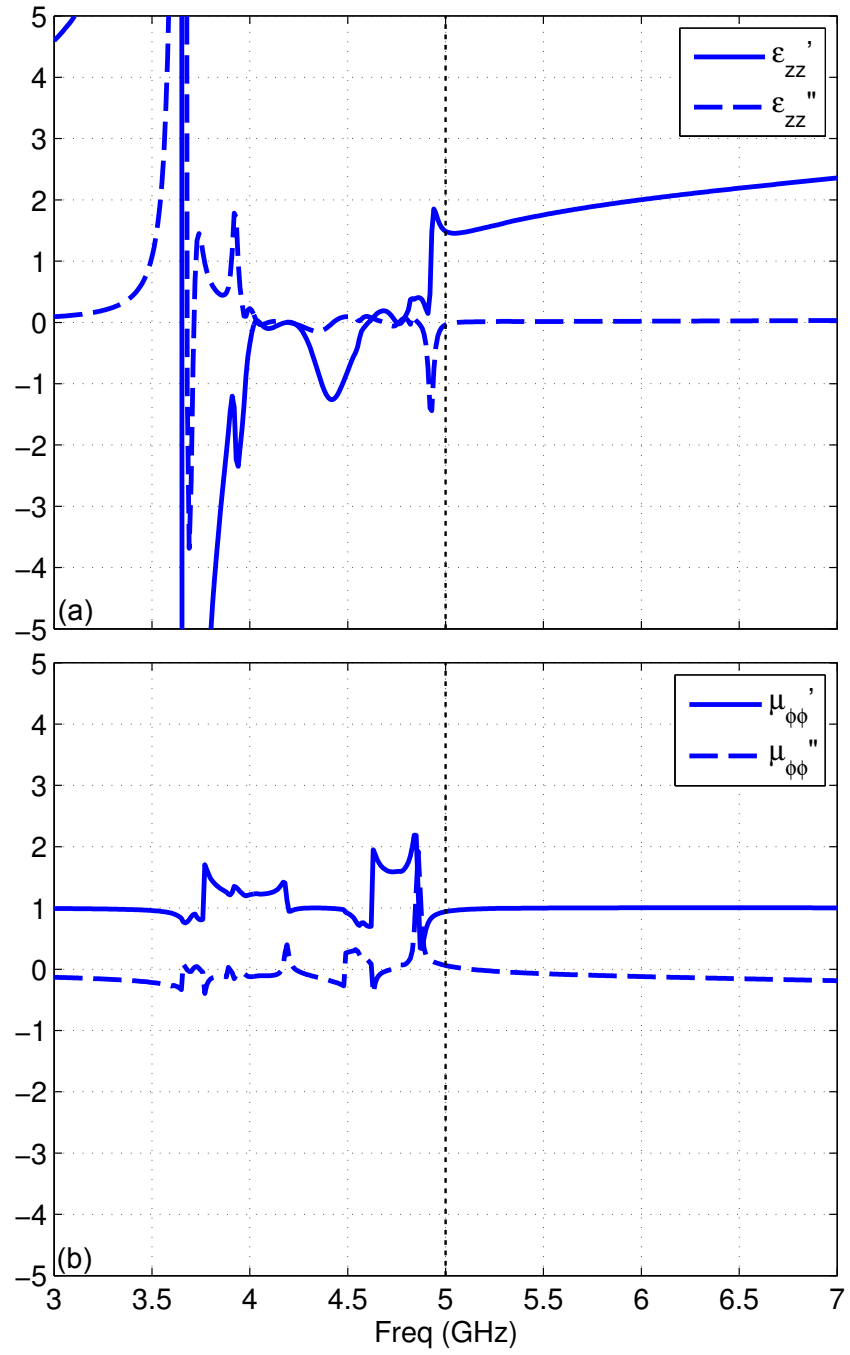


**Figure 6.13.** The retrieved medium parameters of the optimized parallelogram cross-section matcher unit cell for  $A_2$ . (a)  $\epsilon_{zz}$ . (b)  $\mu_{\phi\phi}$ .

are plotted in Figures 6.12 and 6.13. The optimized geometrical parameters are given in Table 6.4.

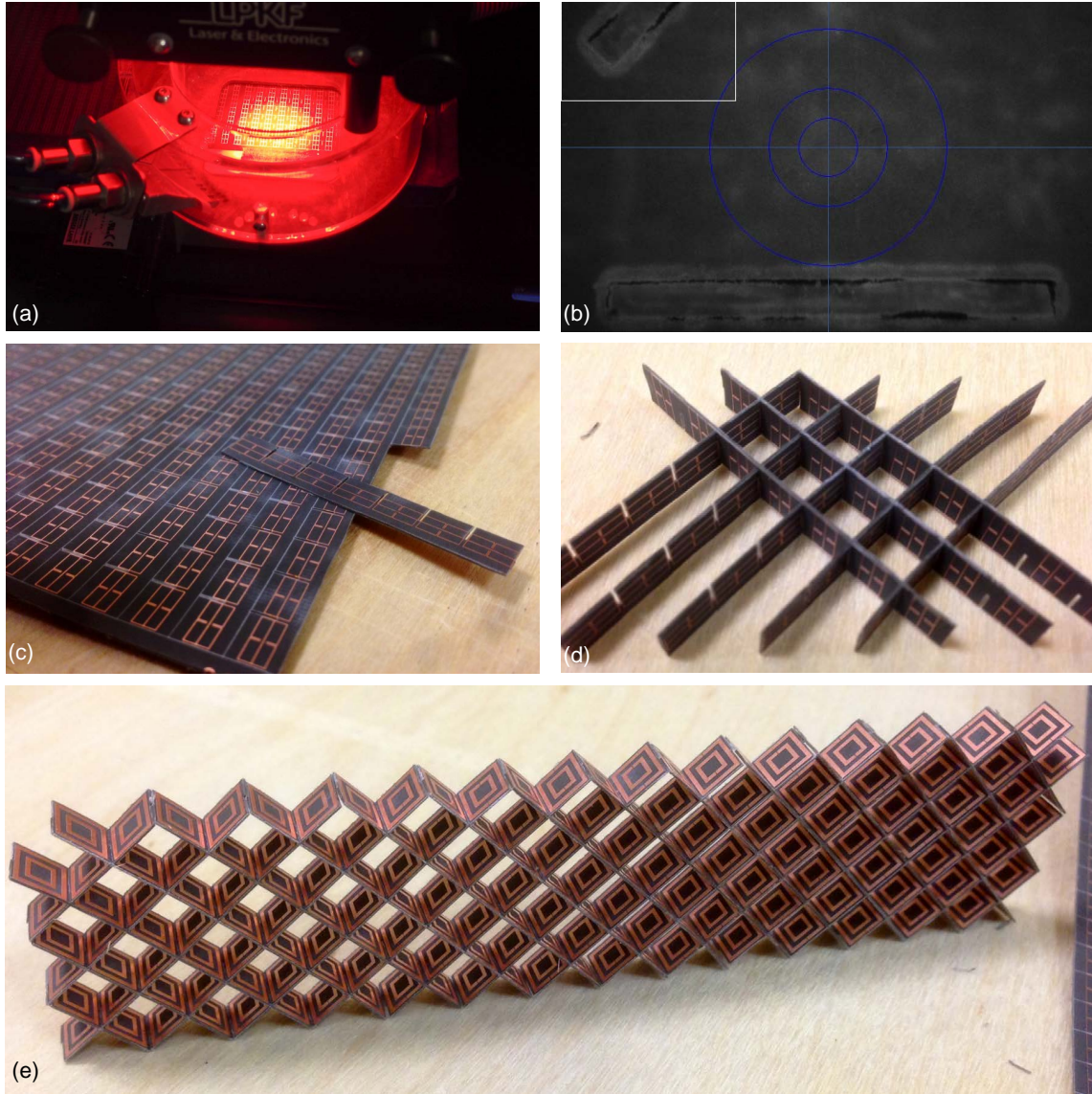
## **6.3 Fabrication, Assembly and Measurement Results**

The metamaterial unit cell walls designed in Sections 6.2 and 6.1 can be fabricated using the standard PCB technologies. Specifically, unit cell walls for the central NIM, outer NIM, and the anisotropic matcher based on the parallelogram cross-section cell design were fabricated. Then, they were assembled to make metamaterial volumes. In this section, the metamaterial assembly steps are first shown and measurement results are presented.

### **6.3.1 Fabrication and Assembly of the Metamaterials**

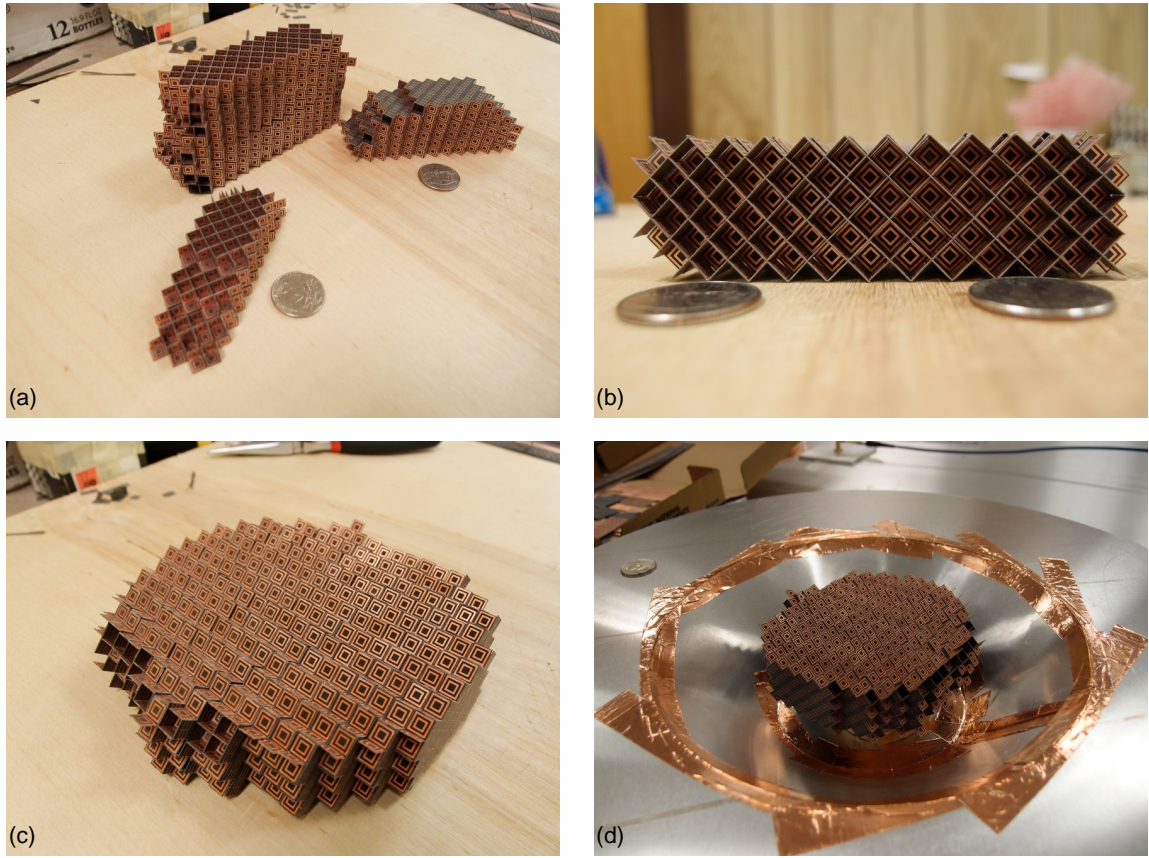
The entire NIM lens volume was split into the inner and outer parts. The central NIM lens region was assembled in an egg-crate structure. The outer NIM volume and the impedance-matching block with the parallelogram cross-section unit cell were assembled in a concentric ring configuration.

Figure 6.14 shows the assembly process for the central NIM, which will fill a cylindrical volume inside the recess, as designed in the Subsection 6.1.2. The fabricated metamaterial walls are in the form of print-etched dielectric panels. First, each panel needs to be cut into strips having the width of a unit cell wall. In order to facilitate assembly of the strips into an array of cubic cells, it was decided that small tabs and slots be created to make an interlocking structure. A precision-cutting operation needed for this process was enabled using a PCB laser etching machine—Protolaser U3 by LPKF Laser and Electronics AG—available in the UMass ECE department. This process is illustrated in Figures 6.14(a)–6.14(b). As shown in Figures 6.14(c)–6.14(d), these strips are assembled in an interlocking structure to form a layer of the metamaterial [Figure 6.14(d)]. Figure 6.14(e) shows the partially assembled central NIM. Figures 6.15(a)– 6.15(b) show a few metamaterial building blocks comprising stacked layers. Finally, the assembled metamaterial for the entire central NIM



**Figure 6.14.** Assembly of the metamaterial for the central NIM volume. (a) Creating slots in the cell walls. (b) A close-up view of the slots. (c) Cut-out cell wall strips. (d) Assembling the walls. (e) One layer of the central NIM.





**Figure 6.15.** Assembled metamaterial for the central NIM volume. (a) Assembled parts of the central NIM. (b) Side view. (c) Assembled central NIM metamaterial. (d) Assembled central NIM the recess.

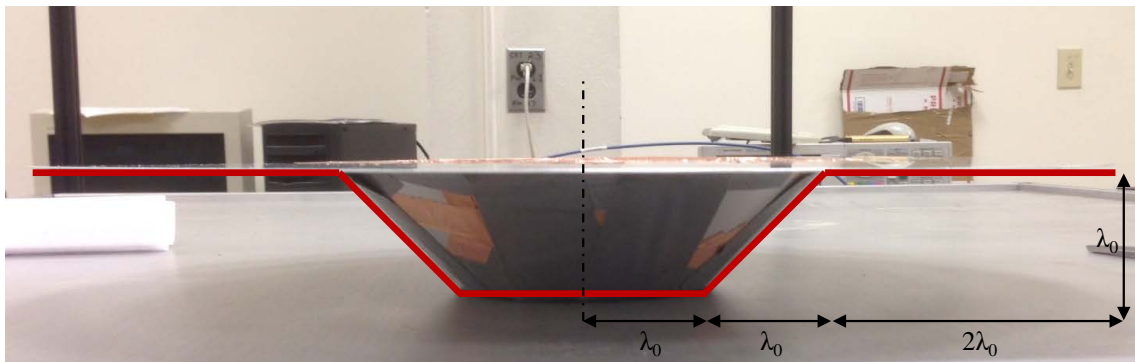


**Figure 6.16.** Fabricated ground recess.  $\lambda_0 = 6$  cm at the design frequency.



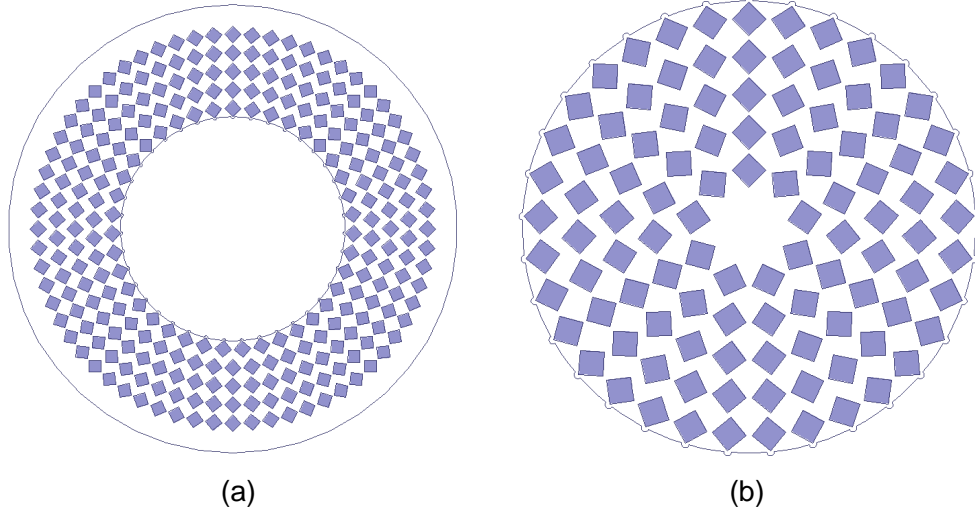


**Figure 6.17.** Top view of the unit cell assembly schematics for NIM lenses. (a) Outer NIM. (b) Central NIM fill using the outer NIM unit cell.

volume is shown in Figure 6.15(c). Figure 6.15(d) shows the central NIM placed inside the recess. The ground recess is fabricated in three pieces using aluminum plates, and assembled as shown in Figure 6.16. The outermost radius of the circular ground plane is  $4\lambda_0$ .

The outer NIM and the matcher metamaterials are held together in position using layers of perforated standard copier papers. Arrays of square holes were created in the papers using the laser cutter to form a holder and spacer for the metamaterial. A schematic for the paper holder of the outer NIM cells is shown in Figure 6.17(a). Assembled columns of unit cells were then inserted in these slots for each individual region as shown in Figure 6.18(a) and (c). Figure 6.19 shows the final assembly for measurements. A  $\lambda_0/4$ -long coax-fed monopole is placed at the bottom of the recess at  $(\rho, z) = (0, -\lambda_0)$  for excitation.

### 6.3.2 Measurement Results

Antenna gain patterns were measured in the near-field range in the Antennas and Propagation Laboratory of the UMass ECE Department. A method of spherical near-field scan and near-to-far field projection was used. Figure 6.20 shows the near-field scanner by

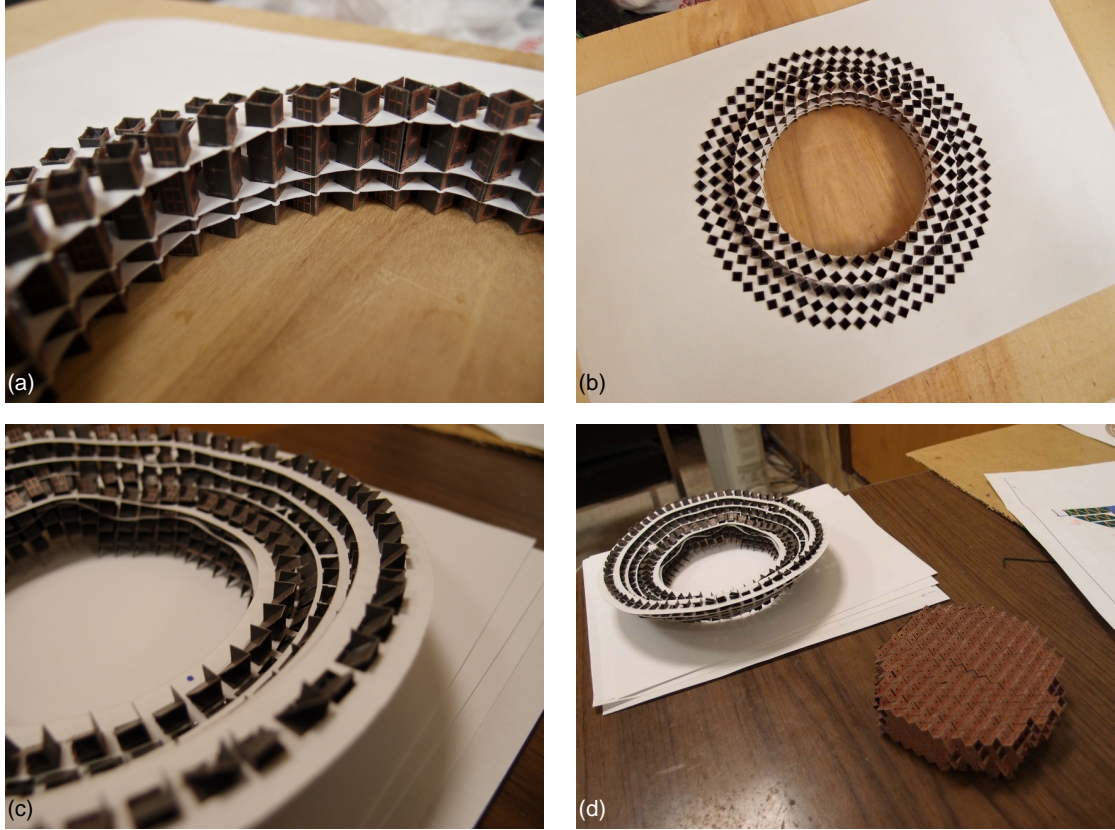


**Figure 6.18.** Assembled metamaterials for each volume. (a) Close-up view of the NIM for the outer volume. (b) Top view of the outer NIM. (c) Close-up view of the matcher metamaterial with the parallelogram cross-section unit cells. (d) Assembled matcher and the central NIM.

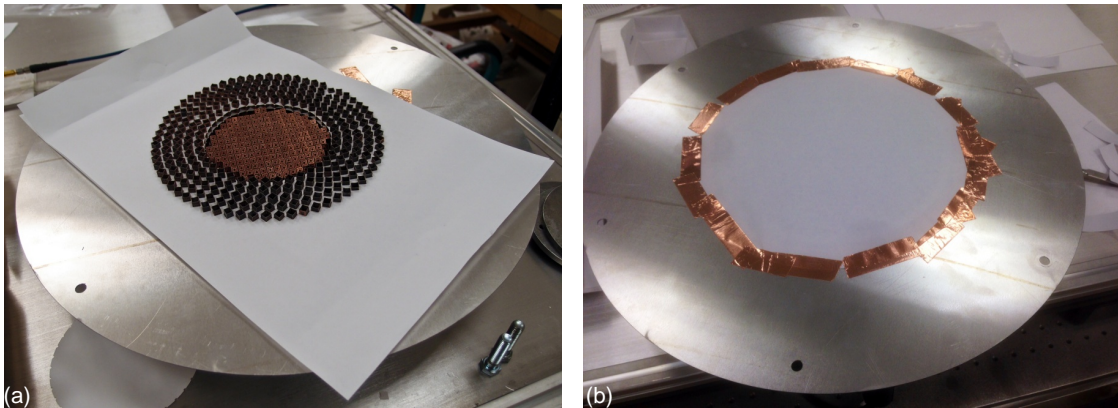


**Figure 6.19.** Metamaterial-embedded monopole antenna inside the ground recess. (a) Recess filled with the assembled metamaterials. (b) Final assembly is paper-covered for measurements.

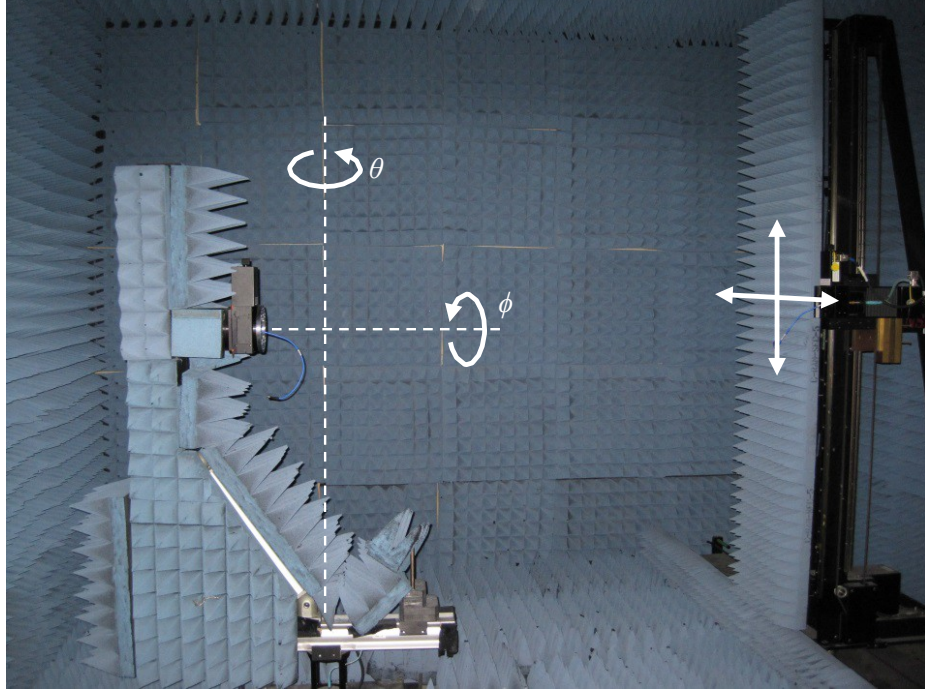


**Figure 6.20.** Near-field range for spherical surface scan.

Nearfield Systems, Inc. inside an anechoic chamber. The spherical measurement takes a phi-over-theta scan, where the AUT (antenna under test) is mounted on the phi positioner, which in turn is mounted on an L-bracket that sits on the theta positioner. A near-field-to-far-field transformation is performed to obtain the AUT gain.

To form a baseline, the original configuration, i.e., a wire monopole antenna on a flat ground plane, is measured. A  $\lambda_0/4$ -long coax-fed thin-wire monopole antenna is placed at the center of a flat circular ground plane. The radius of the ground plane is  $4\lambda_0$ , matching the ground plane size of the metamaterial-embedded physical configuration. At  $f_0 = 5$  GHz, the measured gain pattern is shown in Figure 6.21 together with simulated results obtained using COMSOL Multiphysics. The peak gain is measured to be 3.9 dB at  $\theta = 69.92^\circ$ . In comparison, the simulated gain pattern has a peak value of 5.3 dB at  $\theta = 67.83^\circ$ . The monopole was then placed in an empty recess, and the measured and simulated gain patterns are plotted in Figure 6.22. A significantly distorted pattern charac-

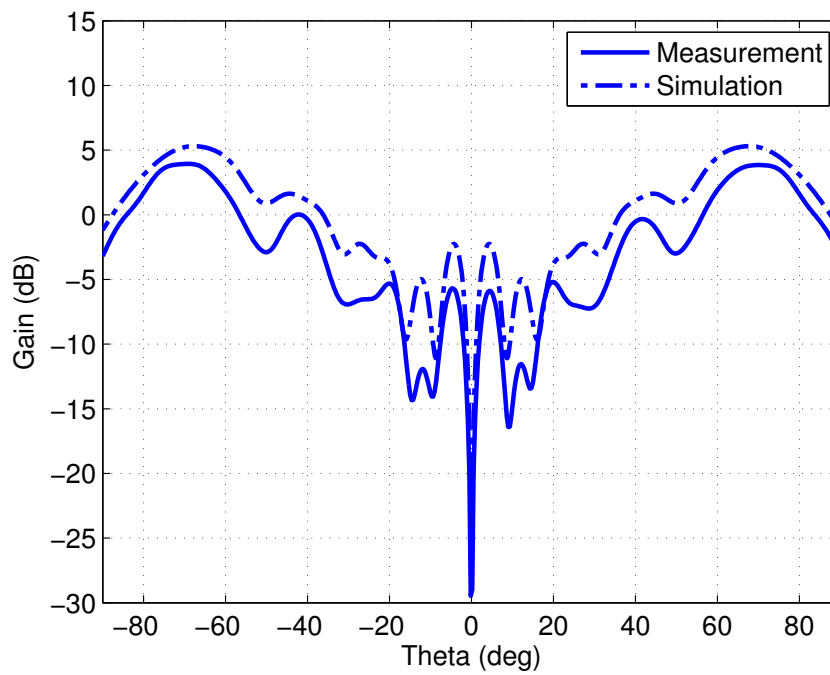


**Figure 6.21.** Gain patterns for the original configuration.

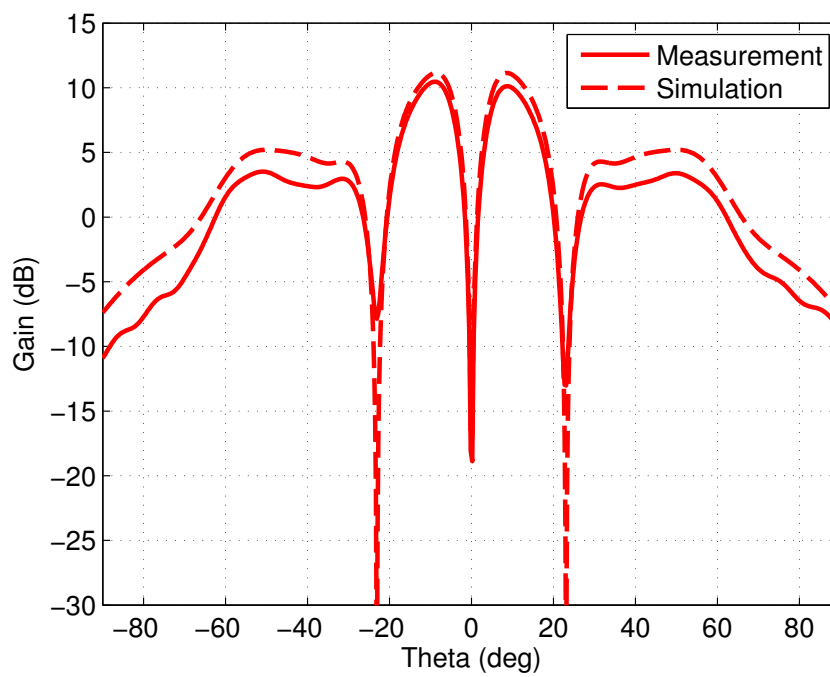


**Figure 6.22.** Gain patterns for a monopole radiating in an empty recess.

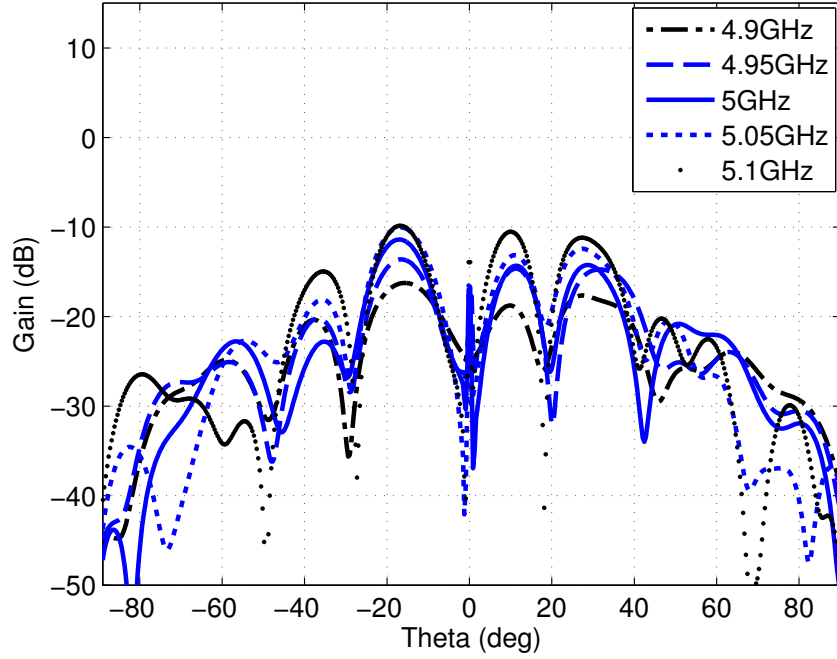


**Figure 6.23.** Measured gain patterns for the material-embedded monopole around  $f_0 = 5$  GHz.

teristics are observed for radiation from inside the empty recess, with the gain maximum appearing at a low-angle from broadside around  $\theta = 10^\circ$ .

The embedding metamaterials assembled in Section 6.3 are placed inside the recess. The measured gain patterns are plotted in Figure 6.23 around the design frequency  $f_0$ . Unexpectedly, it is observed that the patterns possess a low-angle peak similar to the empty recess measurement. At  $f = 5$  GHz, gain peaks are observed at  $\theta = 10.53^\circ$  and  $-16.73^\circ$ . We also notice that the overall gain level is significantly lower (by 20-25 dB) than the reference measurements.

In order to track the source of error in the design or fabrication of the metamaterials, the performance of the central NIM metamaterial lens is investigated. For this purpose, we consider a ground pit, i.e., a ground recess with a cylindrical shell side wall having the radius  $a = \lambda_0$  as illustrated in Figure 6.24. A  $\lambda_0/4$ -long coax-fed monopole is radiating from the bottom of the pit capped with the central NIM metamaterial of Figure 6.15(c). Use



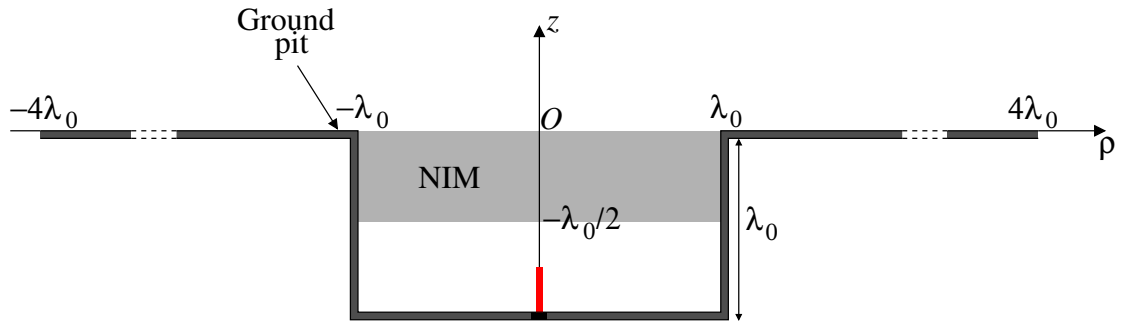


**Figure 6.24.** Ground pit for the central NIM lens experiment.

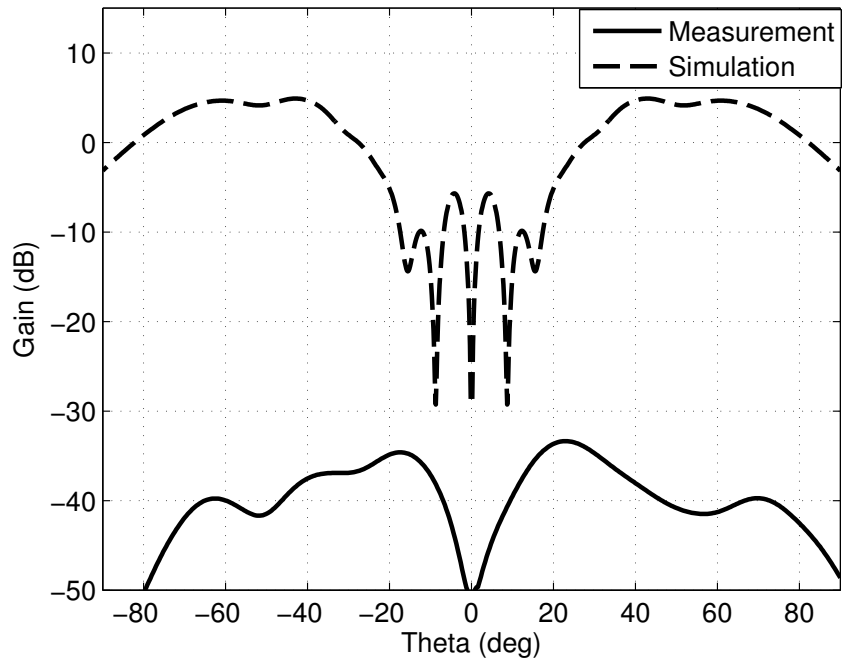


**Figure 6.25.** Gain patterns for a monopole radiating inside the central-NIM-filled pit.

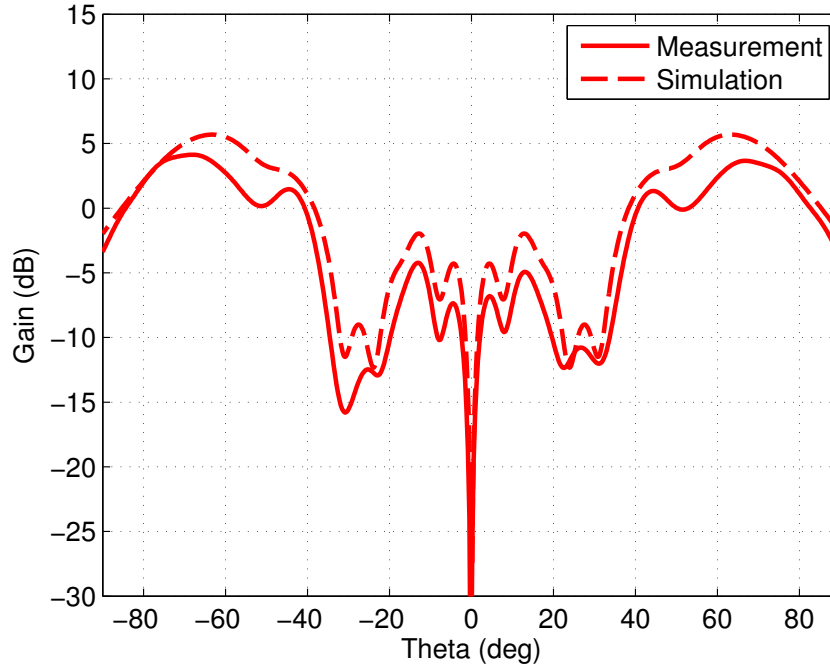


**Figure 6.26.** Gain patterns for a monopole radiating in an empty pit.

of this configuration isolates the problem with the center NIM metamaterial. The measured gain is plotted in Figure 6.25 together with the simulated gain pattern for an ideal NIM-filled pit at the design frequency. For comparison purposes, Figure 6.26 shows the gain patterns for the monopole radiation inside an empty pit by removing the metamaterial cap. It was concluded that the material loss factor for the central NIM is severely high—ending up reducing the radiation efficiency roughly by 40 dB. This is attributed to the sub-optimal effective parameter values shown in Subsection 6.1.2.

In order to isolate and evaluate the performance of the outer NIM metamaterial in Subsection 6.1.1 as a lens, a similar experiment was conducted for the outer NIM lens. Although designed to fill the outer volume of  $A_3$ , the NIM cells of Subsection 6.1.1 were assembled to form a cylindrical center portion of  $A_3$ . The arrangement of NIM metamaterial cell columns is illustrated in Figure 6.17(b). In the ground pit radiation of Figure 6.25, the NIM volume was filled with this new block of outer NIM cells. Due to the unit cell design on the cylindrical basis, volumetric fill is not as efficient as with the central NIM

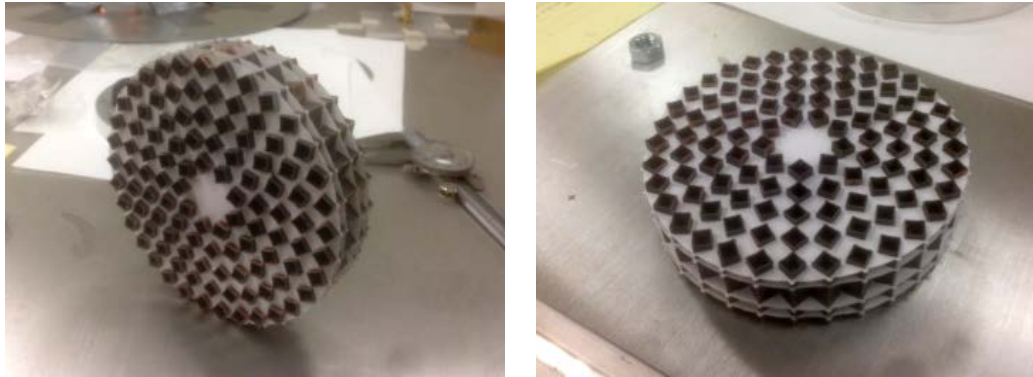


**Figure 6.27.** NIM lens assembled using the outer NIM unit cells for the ground pit measurement.

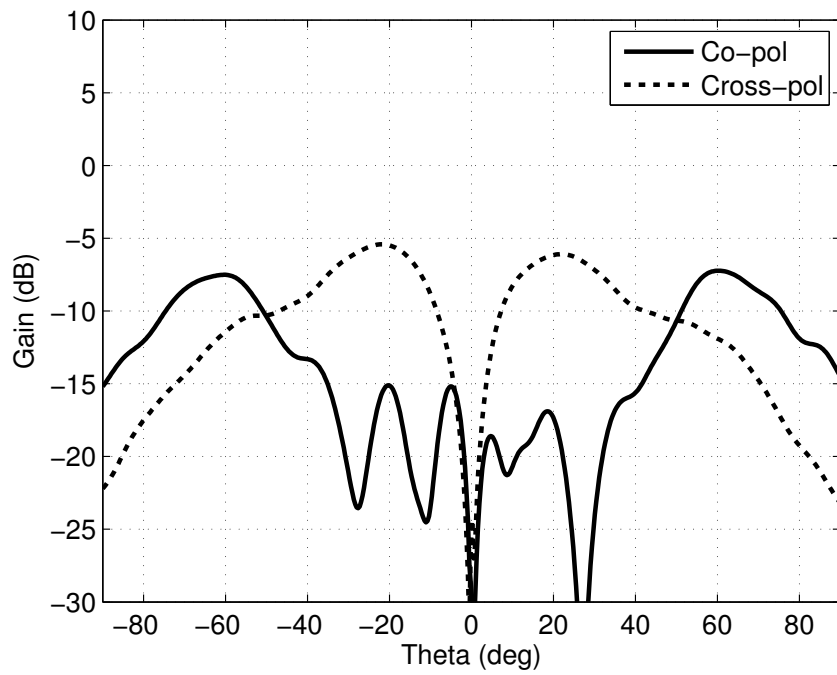


**Figure 6.28.** Measured gain pattern for the pit filled with outer NIM unit cells.



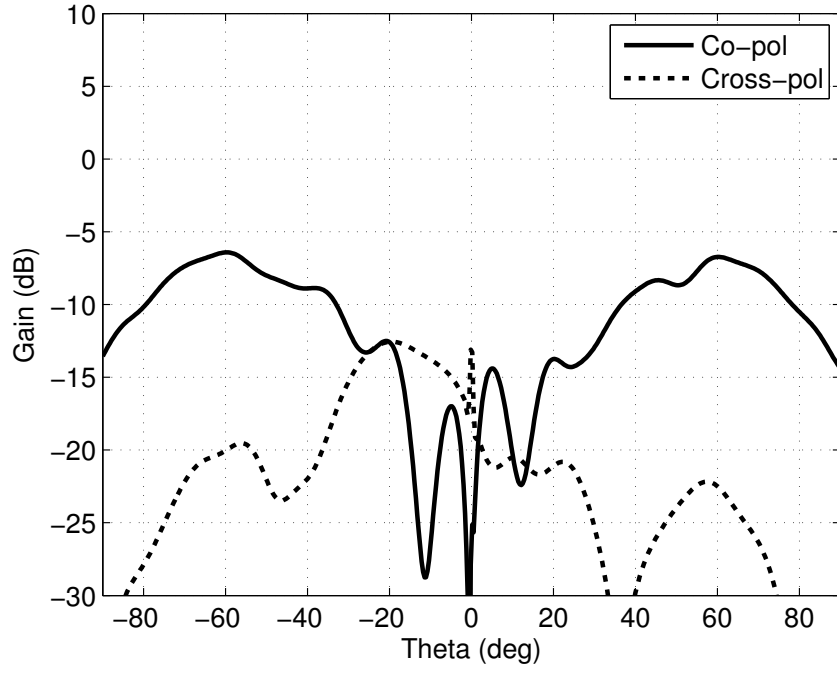


**Figure 6.29.** Measured gain pattern for the pit filled with outer NIM unit cells in a mirror symmetric arrangement.

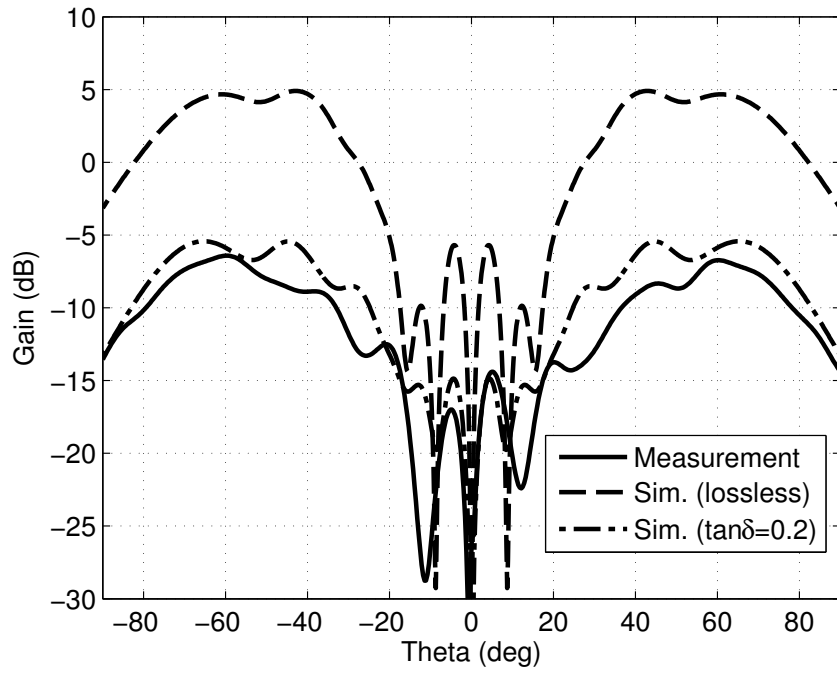


**Figure 6.30.** Gain patterns for the pit filled with outer NIM unit cells in a mirror symmetric arrangement.

design as discussed in Section 6.1. The assembled metamaterial is shown in Figure 6.27. Measurements were performed with this NIM filling the pit. Among the gain patterns measured around the design frequency, patterns at 4.935 GHz are plotted in Figure 6.28. Compared with the central NIM lens measurement results in Figure 6.25, it is observed that the co-polarized gain pattern is significantly improved. We also note the high cross-polarization levels. A potential explanation for this significant cross-polarized radiation is the rotation of the unit cell design of the outer NIM lens, as illustrated in Figure 6.1. To test this hypothesis, the unit cells were newly arranged such that the unit cells in each neighboring quadrant are mirrored with each other. For a constant- $\phi$  cut along the mirror symmetry, the measured gain pattern is plotted in Figure 6.29. Without changing the co-polarized gain pattern noticeably, the cross-polarized gain level was significantly reduced. The measured gain pattern is compared with the simulated pattern in Figure 6.30. With a loss tangent of  $\tan \delta = 0.2$  introduced to the NIM volume in simulation, it is found that the measured gain pattern agrees with the simulations.

Based on measurement results to this point, three conclusions can be drawn. First, the NIM metamaterial for the central volume of  $A_3$  shown in Figure 6.3 is too lossy to be effective in applications. Second, the NIM metamaterial cell for the outer volume of  $A_3$  shown in Figure 6.1 has a significantly reduced loss in comparison, but the  $45^\circ$ -rotation around the  $z$ -axis shown in Figure 6.1(a) introduces a high level of cross-polarized radiation. The directions of the unit cell rotation can be alternated in arranging the cells in forming the  $A_3$  block to reduce the cross-pol level in mirror planes. Third, the NIM lens constructed out of the outer-volume metamaterial cell performs the function of a lens, but with an approximate loss tangent value of 0.2.

To take advantage of the reduced loss of the NIM cell for the outer volume, the entire metamaterial volume  $A_3$  was constructed out of the cell of Subsection 6.1.1. This arrangement is illustrated in Figure 6.31(a). Figure 6.32 shows the assembled NIM positioned inside the recess, setup for measurement without the matcher volume  $A_2$ . The measured

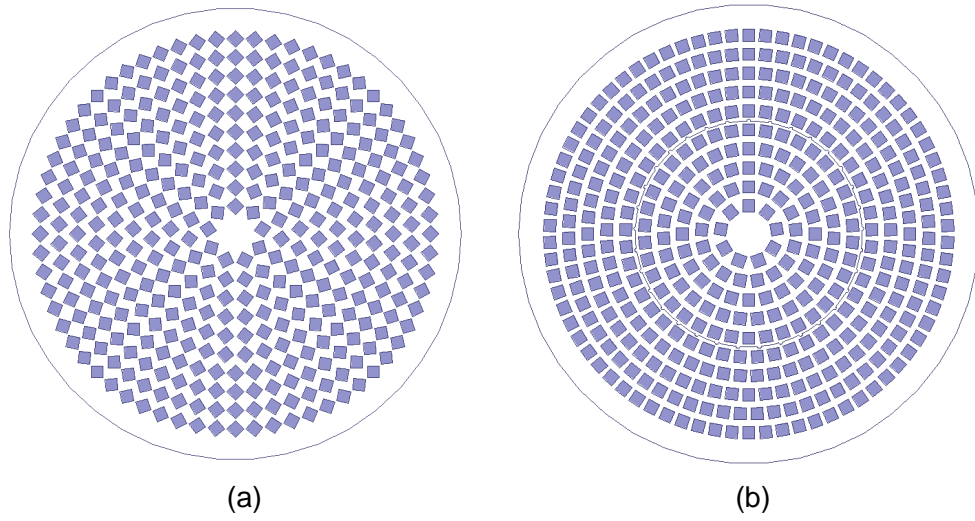


**Figure 6.31.** Top view of the unit cell assembly schematics for the NIM lens. (a) NIM volume fill using outer NIM unit cells. (b) NIM volume fill using the unrotated outer NIM unit cells.

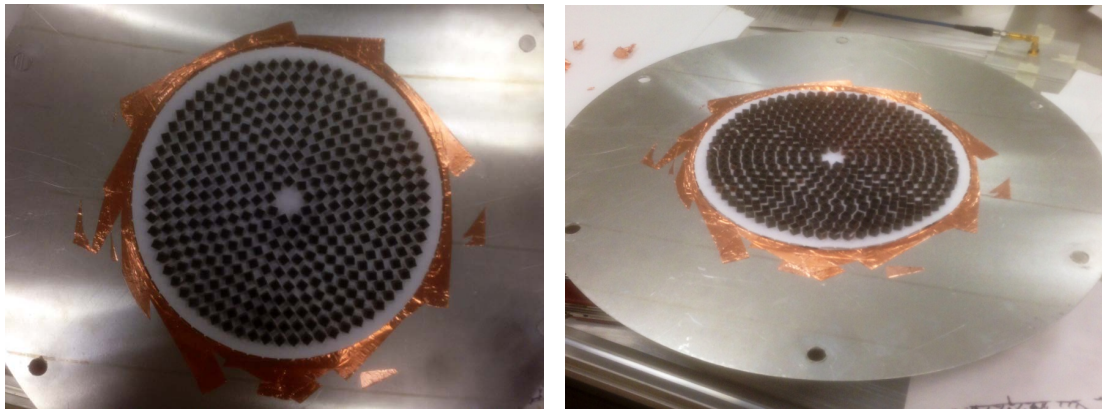


**Figure 6.32.** NIM lens using the outer NIM unit cells positioned inside the ground recess.

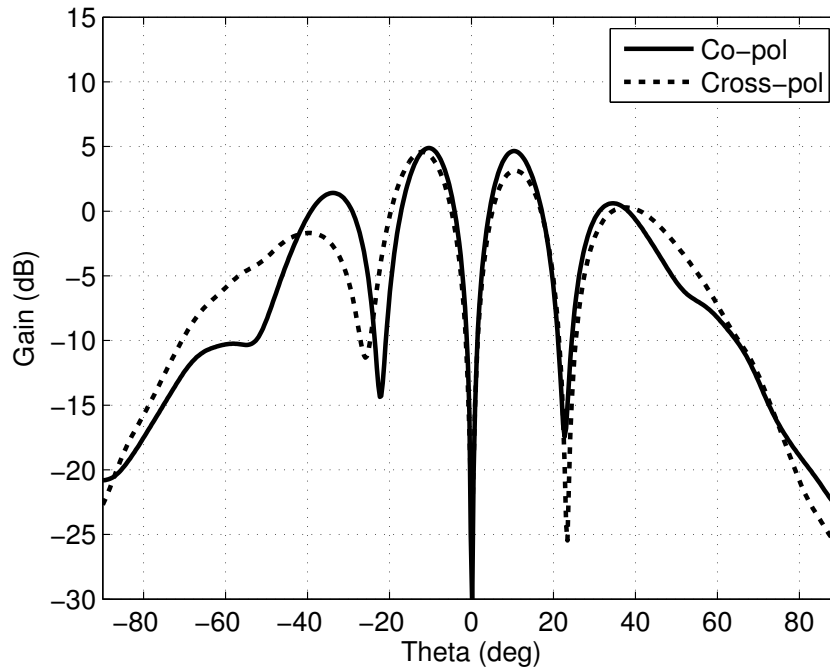


**Figure 6.33.** Measured gain pattern for the NIM-filled recess using the outer NIM unit cells.

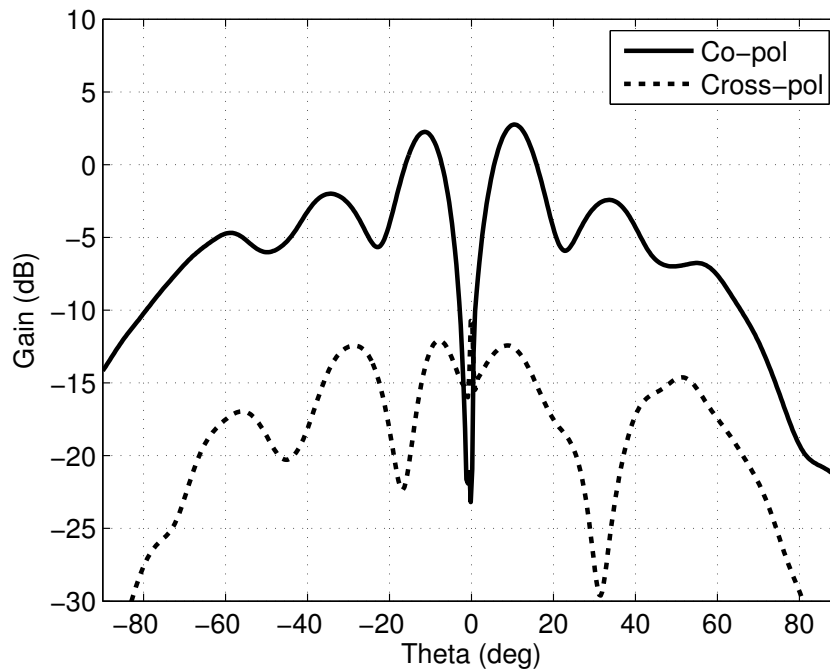


**Figure 6.34.** Measured gain pattern for the NIM-filled recess using the outer volume NIM unit cells in a mirror symmetric arrangement.

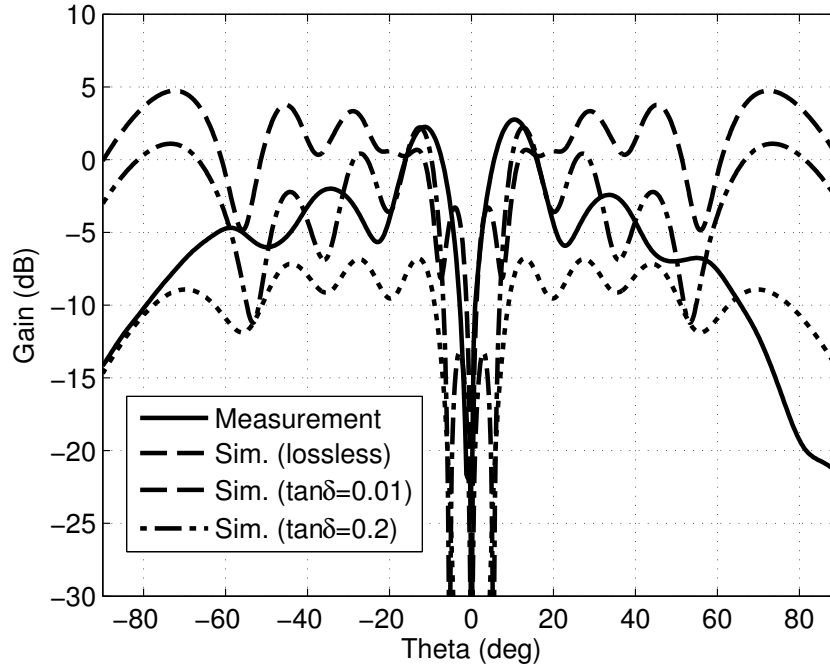


**Figure 6.35.** Gain patterns for the NIM-filled recess using the outer volume NIM unit cells.

gain pattern is plotted in Figure 6.33 at 4.935 GHz. Not surprisingly, cross-polarized radiation as strong as the co-polarized radiation was observed. Also, a large peak appears near the broadside direction and the desired strong radiation near the ground plane is not observed. Next, the NIM cells were arranged to provide mirror symmetry as in the ground pit measurement in order to minimize cross-polarized radiation. The gain patterns plotted in Figure 6.34 were obtained for a constant- $\phi$  cut along a mirror symmetry plane. Similar to the ground pit measurement shown in Figure 6.29, lower overall cross-polarized gains are observed. In Figure 6.35, the measured co-polarized gain pattern is compared with the simulations for an ideal, lossless NIM-filled recess together with lossy NIMs having a loss factor of  $\tan \delta = 0.01$  and  $0.2$ . It was observed that the simulated gain pattern could not be reproduced.

For the simulated gain patterns of ideal and lossy NIM lenses in Figure 6.35, it is observed that the gain levels, while having some variations, remain relatively constant over a wide range of angle  $\theta$ . The measured pattern shows some sign of constant gain levels

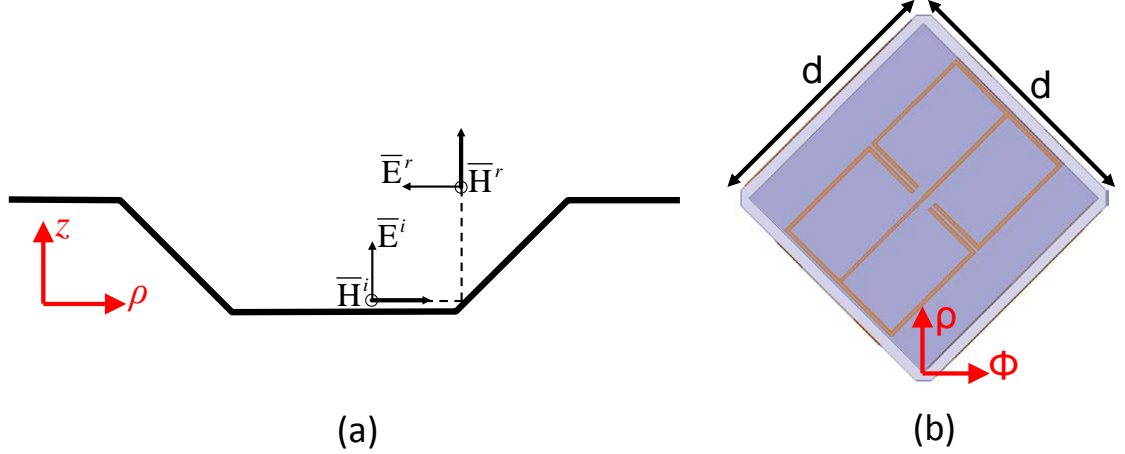


**Figure 6.36.** (a) Reflection inside the recess. (b) A top view of the outer NIM unit cell.

up to  $\theta = 60^\circ$ , but the peak around  $\theta = 10^\circ$  is always present and strongest. However, it is noted that this near-broadside radiation peak was never observed for an embedded monopole inside a ground pit (see Figure 6.29) using the same NIM metamaterial block. It is plausible that the near-broadside peak is associated the geometrical feature of the recess compared with the vertical wall of the pit, i.e., the slanted side wall.

To explain the appearance of a strong radiation peak near broadside for measured patterns, we consider reflection mechanism of waves inside the recess. Assuming that the field of a monopole incident on the slanted recess wall can be visualized as a plane wave with the  $E$ -field in the  $\rho z$ -plane and the associated  $\phi$ -directed  $H$ -field, Figure 6.36(a) illustrates the change of propagation direction due to reflection. The electric field is  $\rho$ -directed for the reflected plane wave. For a NIM-filled recess, this reflected wave are incident on the NIM from the underside of the lens, on the outer volume of  $A_3$ . Therefore, the effective medium parameters of the NIM cell under this combination of polarization ( $E_\rho$ ) and propagation direction ( $+z$ ) is of importance. Figure 6.36(b) shows the top view of the NIM cell together with the coordinate axes. Using the standard parameter retrieval technique of Section 3.1, we found that the cell exhibits a positive index of refraction of  $n = 0.914 - j0.010$  and relative impedance  $z = 0.348 + j0.025$ . The associated effective medium parameters are

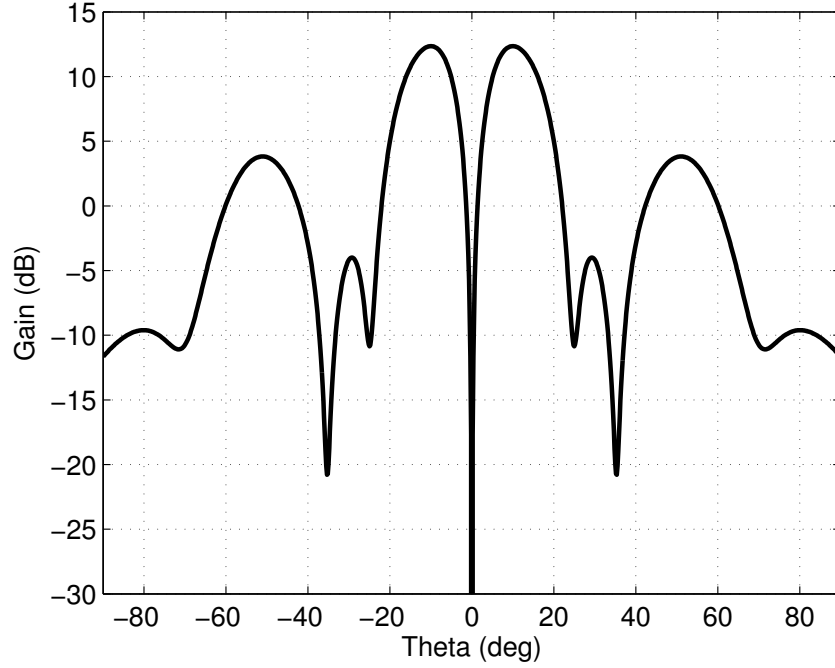


**Figure 6.37.** Simulated gain pattern with the NIM lens replaced with an isotropic medium having the effective medium parameters given by (6.11).

$$\epsilon_{\rho\rho} = 2.610 - j0.214, \quad (6.11)$$

$$\mu_{\phi\phi} = 0.318 + j0.019$$

at the design frequency, which implies that the metamaterial will not function as a NIM for the wave reflected from the recess. This is attributed to the 45°-rotated cell design which was introduced following the successful application in the 2-D case in order to improve the stability of the medium parameters under different angle of incidence as well as to make the homogenization reliable by making the cell structure symmetric in the direction of propagation. As can be observed from Figure 6.36(b), the electric field of a  $\rho$ -polarized polarized plane wave will see an ELC resonator that is longer than for a wave with the  $E$ -field aligned with the ELC axis. As a result, an electric resonance will occur at a lower frequency than the intended 5 GHz, resulting in a set of positive-index medium parameters. Hence, the NIM metamaterial presents a different set of medium parameters for different polarizations and propagation directions, exhibiting both anisotropy (for  $E$ -field) and spatial dispersion

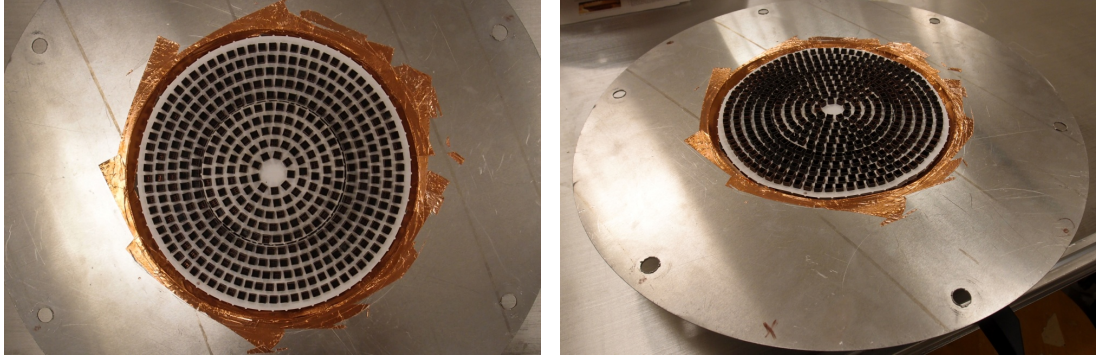


**Figure 6.38.** NIM lens positioned inside the ground recess using the outer NIM unit cells unrotated.

(for  $H$ -field) [27]. We note that this phenomenon does not occur in the case of the rotated NIM cell design of Section 5.1 because only the  $z$ -directed electric field is supported by the 2-D configuration.

For the purpose of characterizing the effect of the spatial dispersion, the NIM volume of  $A_3$  can be filled using an isotropic material with the effective medium parameters of (6.11), by setting  $\epsilon = \epsilon_{\rho\rho}$  and  $\mu = \mu_{\phi\phi}$ . The simulated gain pattern is plotted in Figure 6.37. We observe that the near-broadside peaks that were observed for a monopole inside an empty recess become prominent. Comparing with the measured gain pattern of Figure 6.34, we conclude that the low-angle gain characteristics for the designed NIM-filled recess are primarily due to the effective positive-index medium parameters (6.11) of the unit cell that are experienced by the wave reflected off the slanted recess wall.

Finally, we arrange the unit cells of Subsection 6.1.1 to construct another NIM lens  $A_3$ . For this assembly, the unit cells were arranged using a paper grid without the  $45^\circ$  rotation around the  $z$ -axis as illustrated in Figure 6.31(b). Figure 6.38 shows the assembled NIM inside the recess. The measured gain pattern is plotted in Figure 6.39 at  $f = 4.86$  GHz. Without the cell rotation, the polarization match between the electric field and the axes of the two ELCs in a cell is perfect. As a result, low cross-polarized radiation is expected and confirmed. Figure 6.40 shows the measured co-polarized pattern together with the



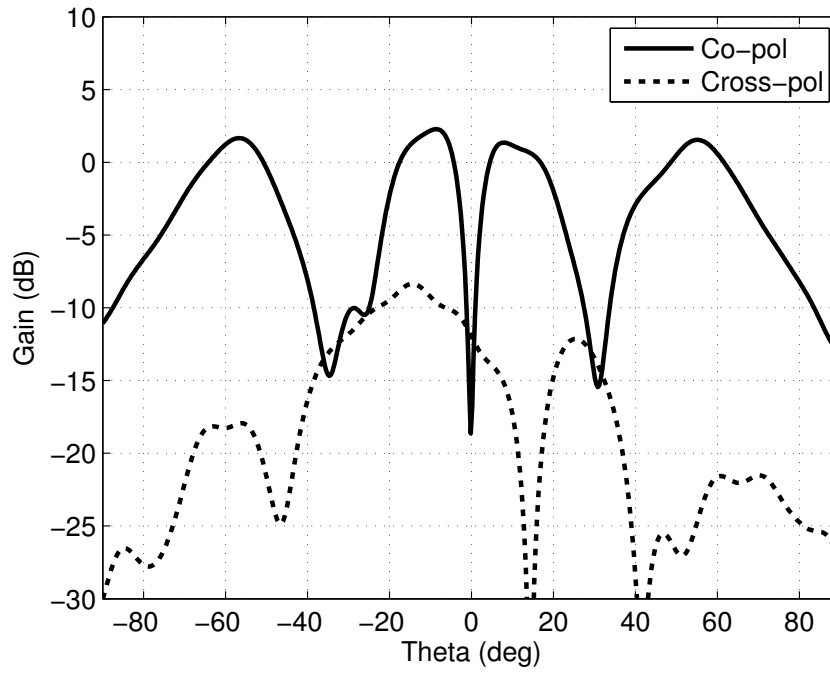


**Figure 6.39.** Measured gain for the NIM-filled recess using the outer NIM unit cells unrotated.

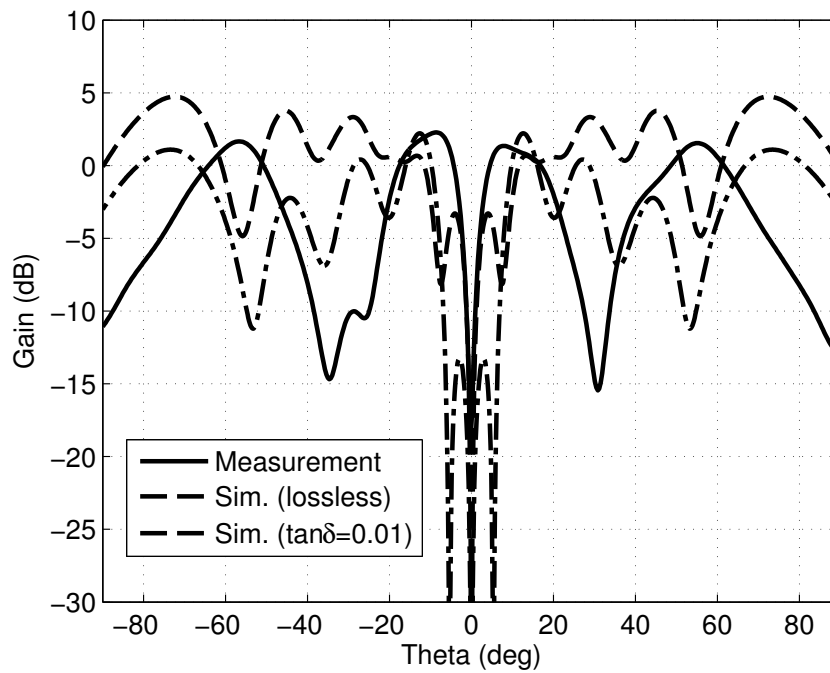


**Figure 6.40.** Gain patterns for the NIM-filled recess using the outer NIM unit cells unrotated.

simulated gain patterns. Comparing with the measured gain pattern of Figure 6.34 for the NIM assembly using rotated NIM cells, a significantly different pattern characteristic is observed. Since the unit cell was optimized to exhibit NIM characteristics in a  $45^\circ$  rotated configuration, the  $A_3$  volume realized using the cell arrangement in Figure 6.31(b) is not expected to operate as a NIM lens.

## **CHAPTER 7**

### **SUMMARY AND CONCLUSIONS**

Metamaterials have been designed in the microwave frequency regime for virtual source formation in various configurations. Based on coordinate transformation in a folded geometry configuration, virtual antennas above a ground plane is synthesized using a physical structure that incorporates a new ground recess, but is completely flush with the ground plane without any physical structure above the plane of the ground.

2-D TL-metamaterials based on the coordinate transformation approach was designed and fabricated. Using a metamaterial-embedded probe, formation of a virtual source was experimentally confirmed. The probe positioned inside a ground recess is embedded in the TL metamaterials such that it creates the same waves as physical probe over a flat ground plane does. The TL metamaterials were fabricated by loading a host 2-D TL microstrip network with lumped reactive elements. Numerical results from simulations and measurement results confirmed an accurate reproduction of the radiation characteristics by the embedded design at the design frequency.

As an extension, a line source embedded in resonant inclusion-based metamaterials for virtual line source formation was investigated in 2-D TE polarization. The standard PCB technologies were used to fabricate the material. Unit cells were assembled to form the embedding media and measurements were performed to test virtual antenna formation. It was confirmed that the metamaterial embedding media translates radiation from the physical line source located inside a recess to a virtual location above the ground plane. For measurement validation, a parallel-plate waveguide simulator apparatus was used to probe the electric field both inside and outside the metamaterial embedding media.

For a 3-D monopole in vertical linear polarization, embedding metamaterials were designed and fabricated. Two variants of the impedance-matching block have been designed in two different unit cell geometries—a rotated cubic cell and a right parallelogram prism cell. Fabricated unit cell walls for the central NIM, outer NIM, and the anisotropic matcher based on the parallelogram cross-section cell were assembled and the metamaterial volumes were arranged in a ground recess. Measurement of gain patterns of an embedded monopole antenna revealed that loss of the central NIM metamaterial was too high to operate as a NIM lens. Use of the unit cells for the outer NIM volume for the NIM lens in a ground pit configuration confirmed relatively moderate loss for the outer NIM metamaterial by measurement. These cells were then used to fill entire NIM volume inside the ground recess. However, it was observed that the rotated cell design introduced a high level of cross-polarized radiation. In addition, it is believed that the metamaterial exhibits a positive index of refraction for the waves reflected from the recess wall, ending up forming a strong radiation lobe near the broadside direction.

Even though low-loss substrates with copper cladding were used in implementing the embedding metamaterials, enhanced conductor and dielectric losses at resonance and the resulting reduction in radiation efficiency of antennas remain as the main obstacles in practical applications. As a future work, it is recommended to investigate similar virtual antenna formation using the recently-emerging metasurfaces [13, 55, 56]. Typically, a metasurface is a single-layer array of subwavelength resonators that can cause a phase discontinuity across the layer. A spatially-varying phase discontinuity can realize anomalous reflection and refraction, including negative refraction, among a variety of features that have been associated with metamaterials. In this regard, metasurfaces show a promise in dramatically reducing the losses typically associated with bulk metamaterials. Hence, it may be possible that virtual antennas could be formed using metasurfaces instead of metamaterials, potentially at an enhanced radiation efficiency in comparison.

## BIBLIOGRAPHY

- [1] Brewitt-Taylor, C. R., and Johns, P. B. On the construction and numerical solution of transmission-line and lumped network models of Maxwell's equations. *Int. J. Numer. Meth. Eng.* 15 (1980), 13–30.
- [2] Caloz, C., and Itoh, T. *Electromagnetic Metamaterials: Transmission Line Theory and Microwave Applications*. Wiley-IEEE Press, Hoboken, NJ, 2006.
- [3] Chen, H., Chan, C. T., and Sheng, P. Transformation optics and metamaterials. *Nature Mater.* 9 (May 2010), 387–396.
- [4] Chen, X., Grzegorz, T. M., Wu, B.-I., J. Pacheco, Jr., and Kong, J. A. Robust method to retrieve the constitutive effective parameters of metamaterials. *Phys. Rev. E* 70 (July 2004).
- [5] Christopoulos, C. *The Transmission-Line Modeling Method TLM*. IEEE Press, Piscataway, NJ, 1995.
- [6] Cummer, S. A., Kundtz, N., and Popa, B.-I. Electromagnetic surface and line sources under coordinate transformations. *Phys. Rev. A* 80, 3 (Sept. 2009), 033 820/1–7.
- [7] Eleftheriades, G. V., and Balmain, K. G. *Negative Refraction Metamaterials: Fundamental Principles and Applications*. Wiley-IEEE Press, Hoboken, NJ, 2005.
- [8] Engheta, N., and Ziolkowski, R. W., Eds. *Metamaterials: Physics and Engineering Explorations*. Wiley-IEEE Press, Hoboken, NJ, 2006.
- [9] Gok, G., and Grbic, A. Tensor transmission-line metamaterials. *IEEE Trans. Antennas Propag.* 58, 5 (May 2010), 1559–1566.
- [10] Grbic, A., and Eleftheriades, G. V. Periodic analysis of a 2-D negative refractive index transmission line structure. *IEEE Trans. Antennas Propag.* 51, 10 (Oct. 2003), 2604–2611.
- [11] Grbic, A., and Eleftheriades, G. V. Overcoming the diffraction limit with a planar left-handed transmission-line lens. *Phys. Rev. Lett.* 92 (2004), 117403/1–4.
- [12] Harrington, R. F. *Time-Harmonic Electromagnetic Fields*. IEEE Press, Piscataway, NJ, 2001.

- [13] Holloway, C. L., Kuester, E. F., Gordon, J. A., O'Hara, J., Booth, J., and Smith, D. R. An overview of the theory and applications of metasurfaces: the two-dimensional equivalents of metamaterials. *IEEE Antennas Propag. Mag.* 54, 2 (Apr. 2012), 10–35.
- [14] Kundtz, N., and Smith, D. R. Extreme-angle broadband metamaterial lens. *Nature Mater.* 9 (Feb. 2010), 129–132.
- [15] Kundtz, N. B., Smith, D. R., and Pendry, J. B. Electromagnetic design with transformation optics. *Proc. IEEE* 99, 10 (Oct. 2011), 1622.
- [16] Kwon, D.-H. Transformation electromagnetic design of embedded monopole in a ground recess for conformal applications. *IEEE Antennas Wireless Propag. Lett.* 9 (2010), 432–435.
- [17] Kwon, D.-H., and Emiroglu, C. D. Low-profile embedded design of endfire scanning arrays with coordinate transformations. *J. Appl. Phys.* 107 (2010), 034 508/1–8.
- [18] Kwon, D.-H., and Emiroglu, C. D. Non-orthogonal grids in two-dimensional transmission-line metamaterials. *IEEE Trans. Antennas Propag.* 60, 9 (Sept. 2012), 4210–4218.
- [19] Kwon, D.-H., and Emiroglu, C. D. Two-dimensional metamaterial designs for line-source radiation from a virtual location. In *Proc. 6th Eur. Conf. Antennas Propag. (EuCAP 2012)* (Prague, Czech Republic, Mar. 2012), pp. 1706–1710.
- [20] Lai, Y., Chen, H., Zhang, Z.-Q., , and Chan, C. T. Complementary media invisibility cloak that cloaks objects at a distance outside the cloaking shell. *Phys. Rev. Lett.* 102 (Mar. 2009), 093901/1–4.
- [21] Lai, Y., Ng, J., Chen, H., D. Han, J. Xiao, Zhang, Z.-Q., and Chan, C. T. Illusion optics: the optical transformation of an object into another object. *Phys. Rev. Lett.* 102 (June 2009), 253902/1–4.
- [22] Leonhardt, U. Optical conformal mapping. *Science* 312 (2006), 1777–1780.
- [23] Leonhardt, U., and Philbin, T. G. General relativity in electrical engineering. *New J. Phys.* 8 (2006), 247/1–18.
- [24] Li, C., Meng, X., Liu, X., Li, F., Fang, G., Chen, H., and Chan, C. T. Experimental realization of a circuit-based broadband illusion-optics analogue. *Phys. Rev. Lett.* 105 (Dec. 2010), 233906/1–4.
- [25] Li, J., and Pendry, J. B. Hiding under the carpet: a new strategy for cloaking. *Phys. Rev. Lett.* 101 (Nov. 2008), 203901/1–4.
- [26] Liu, X., Li, C., Yao, K., Meng, X., and Li, F. Invisibility cloaks modeled by anisotropic metamaterials based on inductor-capacitor networks. *IEEE Antennas Wireless Propag. Lett.* 8 (2009), 1154–1157.

- [27] Markus, R., Martn, F., and Sorolla, M., Eds. *Metamaterials with Negative Parameters: Theory, Design and Microwave Applications*. Wiley, Hoboken, NJ, 2008.
- [28] Milton, G. W., Briane, M., and Willis, J. R. On cloaking for elasticity and physical equations with a transformation invariant form. *New J. Phys.* 8 (2006), 248/1–20.
- [29] Pendry, J. B. Negative refraction makes a perfect lens. *Phys. Rev. Lett.* 85 (2000), 3966–3969.
- [30] Pendry, J. B., Holden, A. J., Robbins, D. J., and Stewart, W. J. Low frequency plasmons in thin-wire structures. *J. Phys.: Condens. Matter* 10, 22 (1998), 4785–4809.
- [31] Pendry, J. B., Holden, A. J., Robbins, D. J., and Stewart, W. J. Magnetism from conductors and enhanced nonlinear phenomena. *IEEE Trans. Microw. Theory Tech.* 47, 11 (Nov. 1999), 2075–2084.
- [32] Pendry, J. B., Holden, A. J., Stewart, W. J., and Youngs, I. Extremely low frequency plasmons in metallic mesostructures. *Phys. Rev. Lett.* 76, 25 (1996), 4773–4776.
- [33] Pendry, J. B., Schurig, D., and Smith, D. R. Controlling electromagnetic fields. *Science* 312 (2006), 1780–1782.
- [34] Popa, B.-I., Allen, J., and Cummer, S. A. Conformal array design with transformation electromagnetics. *Appl. Phys. Lett.* 94 (2009), 244 102/1–3.
- [35] Pozar, D., Ed. *Microwave Engineering*. Wiley, Hoboken, NJ, 2005.
- [36] Rahm, M., Cummer, S. A., Schurig, D., Pendry, J. B., and Smith, D. R. Optical design of reflectionless complex media by finite embedded coordinate transformations. *Phys. Rev. Lett.* 100 (2008), 063903/1–4.
- [37] Rahm, M., Schurig, D., Roberts, D. A., Cummer, S. A., Smith, D. R., and Pendry, J. B. Design of electromagnetic cloaks and concentrators using form-invariant coordinate transformations of Maxwell’s equations. *Photon. Nanostruct.: Fundam. Applic.* 6 (2008), 87–95.
- [38] Ruppin, R. Surface polaritons of a left-handed material slab. *J. Phys. Condens. Matter* 13, 9 (Mar. 2001), 1811–1818.
- [39] Schurig, D., Mock, J. J., Justice, B. J., Cummer, S. A., Pendry, J. B., Starr, A. F., and Smith, D. R. Metamaterial electromagnetic cloak at microwave frequencies. *Science* 314 (2006), 977–980.
- [40] Schurig, D., Mock, J. J., and Smith, D. R. Electric-field-coupled resonators for negative permittivity metamaterials. *Appl. Phys. Lett.* 88, 041109 (2006).
- [41] Schurig, D., Pendry, J. B., and Smith, D. R. Calculation of material properties and ray tracing in transformation media. *Opt. Express* 14 (2006), 9794–9804.

- [42] Selvanayagam, M., and Eleftheriades, G. V. Transmission-line metamaterials on a skewed lattice for transformation electromagnetics. *IEEE Trans. Microw. Theory Tech.* 59, 12 (Dec. 2011), 3272–3282.
- [43] Shelby, R. A., Smith, D. R., and Schultz, S. Experimental verification of a negative index of refraction. *Science* 292 (Apr. 2001).
- [44] Smith, D. R., Gollub, J., Mock, J. J., Padilla, W. J., and Schurig, D. Calculation and measurement of bianisotropy in a split ring resonator metamaterial. *J. Appl. Phys.* 100 (2006), 024 507/1–9.
- [45] Smith, D. R., Padilla, Willie J., Vier, D. C., Nemat-Nasser, S. C., and Schultz, S. Composite medium with simultaneously negative permeability and permittivity. *Phys. Rev. Lett.* 84, 18 (2000), 4184–4187.
- [46] Smith, D. R., and Pendry, J. B. Homogenization of metamaterials by field averaging. *J. Opt. Soc. Am. B* 23 (Mar. 2004).
- [47] Smith, D. R., Schultz, S., Markos, P., , and Soukoulis, C. M. Determination of effective permittivity and permeability of metamaterials from reflection and transmission coefficients. *Phys. Rev. B* 65 (Apr. 2002).
- [48] Smith, D. R., Schurig, D., Rosenbluth, M., Schultz, S., Ramakrishna, S. A., and Pendry, J. B. Limitations on subdiffraction imaging with a negative refractive index slab. *Appl. Phys. Lett.* 82 (2003), 1506–1508.
- [49] Smith, D. R., Vier, D. C., Koschny, Th., and Soukoulis, C. M. Electromagnetic parameter retrieval from inhomogeneous metamaterials. *Phys. Rev. E* 71 (2005), 036617/1–11.
- [50] Starr, A. F., Rye, P. M., Smith, D. R., and Nemat-Nasser, S. Fabrication and characterization of a negative-refractive-index composite metamaterial. *Phys. Rev. B* 70 (Sept. 2004), 113102.
- [51] Vier, D. C., Schultz, S., Greigor, R. B., Parazzoli, C. G., Nielsen, J. A., and Tanielian, M. H. Three-dimensional double-negative metamaterials resonating at 13.5 GHz. *Microwaves, Antennas Propagation, IET* 3, 5 (2009), 723–727.
- [52] Ward, A. J., and Pendry, J. B. Refraction and geometry in Maxwell’s equations. *J. Mod. Opt.* 43, 4 (1996), 773–793.
- [53] Werner, D. H., and Kwon, D.-H., Eds. *Transformation Electromagnetics and Metamaterials: Fundamental Principles and Applications*. Springer, London, 2014.
- [54] Wu, B. I. Transformation electromagnetics for antenna applications. In *Transformation Electromagnetics and Metamaterials: Fundamental Principles and Applications*, Douglas H. Werner and Do-Hoon Kwon, Eds. Springer, London, 2014, ch. 9.



- [55] Yu, N., and Capasso, F. Flat optics with designer metasurfaces. *Nat. Mater.* 13 (Feb. 2014), 139–150.
- [56] Yu, N., Genevet, P., Kats, M. A., Aieta, F., Tetienne, J.-P., Capasso, F., , and Gaburro, Z. Light propagation with phase discontinuities: generalized laws of reflection and refraction. *Science* 334 (Oct. 2011), 333–337.
- [57] Zedler, M., and Eleftheriades, G. V. 2D transformation optics using anisotropic transmission-line metamaterials. In *Proc. 2010 IEEE Int. Microw. Symp.* (Anaheim, CA, May 2010), pp. 33–36.